Flexible preclinical models of high-grade serous ovarian carcinoma to elucidate mechanisms of treatment sensitivity and resistance

by

Stella V. Paffenholz

A Dissertation

Presented to the Faculty of the Louis V. Gerstner, Jr.

Graduate School of Biomedical Sciences,

Memorial Sloan-Kettering Cancer Center

in Partial Fulfillment of the Requirements for the Degree of

Doctor of Philosophy

New York, NY

September 2022

_____ _____

Scott W. Lowe, PhD
Dissertation mentor

Date

DEDICATION

I would like to dedicate this thesis to my grandfather, Wilhelm Koch, who always supported me on my scientific quests and adventures. He helped me conceptualize and write my first scientific term paper in high school over a decade ago. I wish he could have read this thesis today and asked curious questions.

ABSTRACT

High-grade serous ovarian carcinoma (HGSOC) is a cancer with dismal prognosis due to the limited effectiveness of existing chemo- and immunotherapies. To elucidate mechanisms mediating sensitivity or resistance to these therapies, we developed a fast and flexible autochthonous mouse model based on somatic introduction of HGSOC-associated genetic alterations into the ovary of immunocompetent mice using tissue electroporation. Tumors arising in these mice recapitulate the metastatic patterns, histological, molecular, and treatment response features of the human disease. By leveraging these models, we show that the ability to undergo senescence underlies the clinically observed increase in sensitivity of homologous recombination (HR) deficient HGSOC tumors to platinum-based chemotherapy. In this context, cGas/STING-mediated activation of a restricted senescence-associated secretory phenotype (SASP) was sufficient to induce immune infiltration and sensitize HR-deficient tumors to immune checkpoint blockade. This study identifies senescence propensity as a predictor of therapy response and defines a limited SASP profile that appears sufficient to confer added vulnerability to concurrent immunotherapy. In ongoing experiments, we apply our model to investigate cholesterol metabolism as a potential therapeutic vulnerability in HGSOC tumors with PI3K hyperactivation and analyze the response of HGSOC to cellular immunotherapies. In sum, this work provides a blueprint for the implementation of electroporation-based mouse models to reveal mechanisms of oncogenesis and therapy response in HGSOG.

ACKNOWLEDGEMENTS

I would like to thank my thesis advisor Dr. Scott W. Lowe for his mentorship and tremendous support during my PhD. Scott allowed me to independently explore different angles of this and other projects, while at the same time providing critical scientific advice and big picture thinking. Over the years, Scott has taught me how to become a rigorous scientist, how to focus on the most exciting and important questions and experiments, how to set ambitious goals and achieve them, how to have fun outside of the lab and most importantly how to be a nice and caring lab member.

I am thankful to my committee members Dr. Dana Pe'er and Dr. Charles Sawyers for providing critical guidance and invaluable insights on my PhD projects over the years.

I would like to thank Dr. Francisco J. Sánchez-Rivera, my first postdoc mentor in the lab, for teaching me proper experimental design and execution, scientific thinking, and perseverance. I would like to thank Dr. Josef Leibold, my second mentor in the lab and the happiest German in existence, who easily managed to counterbalance my sporadic phases of fatalistic thinking. I have learned a tremendous amount from both of my mentors not only about science but also about life.

I am grateful to my collaborator Dr. Camilla Salvagno, who – together with Josef and myself – brought this project to life, discussed data, and designed and performed experiments along the way. I would also like to thank Dr. Yu-Jui (Ray) Ho, who performed impeccable bioinformatic analysis and always had an open

office door, and Dr. Dmitriy Zamarin for fruitful data discussion. I would like to say a special thanks to Alexandra Wuest and Amanda Kulick, who provided outstanding technical support for my project, are collaborative, reliable, and very fun to work with.

I am grateful to have crossed paths with other graduate students in the lab, Margaret Kennedy, Caroline Broderick, Dr. Hsuan-An (Sean) Chen, Dr. Xiang (Grace) Li, Dr. Evangelia Loizou and Dr. Chi-Chao Chen, who are all prime examples of enthusiasm and resilience.

I would like to thank all Lowe Lab members for cultivating a vibrant and friendly environment, where you can openly discuss scientific ideas and have fun. A special thank you goes to Dr. Direna Alonso Curbelo for helping me design the most complex flow panels and being an inspiring scientific role model; to Dr. Jose Reyes for teaching me everything there is to know about imaging and data analysis; to Dr. Kaloyan Tsanov, Dr. Francisco M. Barriga and Dr. Bryan Ngo for scientific discussions and support with publishing my paper; to Dr. Clemens Hinterleitner for good mood in the bay; to Dr. Riccardo Mezzadra for help with immunology experiments; to Dr. Almudena Chaves Perez for patiently answering every question about macro usage; and to Dr. Changyu Zhu for having an open ear during rough times.

I started my grad school endeavor with other fearless individuals and would like to thank my GSK class mates Miguel de Jesus, Michael Galiano, Dr. Zhongmin Wang, Dr. Tyler Hitchman, and Dr. Yu-Jung Chen for supporting each other and making graduate school more colorful. A special thanks to Dr. Amy Shyu for

endless discussions about career and life choices. She always knew the right path to take way before I did.

Being far away from home, I would like to thank my supportive family, my dad Norbert Paffenholz for his never-ending positivity and encouragement of my restlessness; my mom Dr. Veronika Paffenholz for keeping my life on track; my grandmother Elisabeth Koch for her love and support; my sister Dr. Pia Paffenholz and brother-in-law Dr. Sven Loosen for fun times in New York City during your visits and discussing scientific questions from a clinical angle; and Josef and Stefani Langel for welcoming me to family festivities away from home.

Lastly, I am hugely grateful for all the friendships that I made in New York City while running, biking, hiking, or doing other crazy things. Those interactions and activities gave me energy and strength when life in the lab was challenging.

TABLE OF CONTENTS

LIST OF FIGURES ..... **x**

LIST OF TABLES ..... **xi**

LIST OF ABBREVIATIONS ..... **xii**

INTRODUCTION **1**

OVARIAN CANCER 1
Epidemiology of Human Ovarian Cancer 1
Subtypes of Human Ovarian Cancer 1
Clinical Management of Human HGSOC 2
Cell of origin of HGSOC 2
Understanding of Ovarian Cancer from its Molecular Basis 3
Tumor microenvironment of HGSOC 5
MOUSE MODELS OF OVARIAN CANCER 6
Cell line models 6
Organoid models 7
In vivo models 7
SENESCENCE 10
Hallmarks of Senescence 10
Biomarkers of Senescence 11
Senescence in cancer treatment 12

OBJECTIVES **15**

MATERIALS AND METHODS **16**

PRODUCTION OF EPO-GEMM TUMORS 16
Animal studies 17
DNA constructs for electroporation 17
Ultrasound and bioluminescence imaging 17
PRECLINICAL DRUG STUDIES 18
CHARACTERIZATION OF EPO-GEMM TUMORS 19
Clonality analysis of EPO-GEMM tumors 20
CNA inference 20
Tumor RNA-sequencing (RNA-seq) 21
Clustering and Gene Set Enrichment Analysis (GSEA) 22

Immunohistochemistry and immunofluorescence 22
Flow Cytometry 23
CHARACTERIZATION OF CELLULAR SENESCENCE AND CGAS/STING RESPONSE 24
Senescence-associated beta-galactosidase staining 25
Cytokine array 25
Micronuclei quantification 26
IN VITRO CELL ASSAYS 26
Rad51 assay 27
RT-qPCR 28
HUMAN CELL LINE AND TUMOR ANALYSES 28
STATISTICS 29
FIGURE PREPARATION 29
RESULTS 36
SOMATIC INTRODUCTION OF ONCOGENIC LESIONS GENERATES HIGH-GRADE SEROUS OVARIAN CARCINOMA 36
HR-DEFICIENT TUMORS HAVE UNIQUE GENOMIC, IMMUNE, AND THERAPY RESPONSE FEATURES 45
CISPLATIN TREATMENT PREFERENTIALLY INDUCES TUMOR CELL SENESCENCE AND ALTERS IMMUNE INFILTRATES IN HR-DEFICIENT HGSOC 51
CISPLATIN TREATMENT LEADS TO A CGAS/STING-DEPENDENT INFILTRATION OF T- AND NK CELLS IN HR-DEFICIENT TUMORS. 58
BRCA1 LOSS SENSITIZES TUMORS TO CHEMO AND ICB COMBINATION THERAPY 64
DISCUSSION 70
APPENDIX 77
CHOLESTEROL METABOLISM AS A THERAPEUTIC VULNERABILITY IN PI3K HYPER-ACTIVATED HGSOC TUMORS 77
TREATMENT OF OVARIAN CANCER WITH CELLULAR IMMUNOTHERAPIES 84
BIBLIOGRAPHY 88
PUBLICATION 105

LIST OF FIGURES

Figure 1: Overview of the advantages and disadvantages of HGSOC models systems. 9
Figure 2. Somatic introduction of oncogenic lesions generates high-grade serous ovarian carcinoma..... 42
Figure 2.1: EPO-GEMM approach generates high-grade serous ovarian cancer that is of epithelial origin. 43
Figure 3. HR-deficient tumors have unique genomic, immune, and therapy response features. 48
Figure 3.1: HR deficiency drives tumors with increased T-cell infiltration and improved therapy response. 50
Figure 4. Cisplatin treatment preferentially induces tumor cell senescence and alters immune infiltrates in HR-deficient HGSOC. 55
Figure 4.1: Chemotherapy treatment induces senescence and SASP in HR-deficient HGSOC. 57
Figure 5. Cisplatin treatment leads to a cGas/STING-dependent infiltration of T- and NK cells in HR-deficient tumors. 61
Figure 5.1: cGas knockdown does not alter the myeloid immune compartment or cell-intrinsic senescence response. 63
Figure 6. *Brca1* loss sensitizes tumors to chemo and ICB combination therapy. 67
Figure 6.1: Treatment response of HR-proficient and -deficient HGSOC after treatment with chemotherapy and ICB..... 68
Figure 7: EPO-GEMMs recapitulate genetic features of human HGSOC and provide insights into human biology and treatment response..... 70
Figure 8. Pten loss in EPO-GEMM tumors accelerates onset and severity of disease..... 79
Figure 9. Loss of Pten promotes upregulation of cholesterol biosynthesis..... 83
Figure 10. Targeting of murine ovarian cancer with uPAR CAR-T cells. 87

LIST OF TABLES

Table 1: Overview of electroporation plasmid mixes 30
Table 2: sgRNA sequences 31
Table 3: Primary antibodies for IHC and IF..... 32
Table 4: Antibodies used for flow cytometry analysis (myeloid panel)..... 33
Table 5: Antibodies used for flow cytometry analysis (lymphoid panel) 34
Table 6: Primer sequences used for RT-qPCR 35

LIST OF ABBREVIATIONS

BRCA	Breast Cancer Gene
CA-125	Cancer Antigen 125
CAR	Chimeric antigen receptor
cDNA	Complementary DNA
CEBPB	CCAAT/enhancer-binding protein beta
cGAS	Cyclic GMP-AMP synthase
CK7	Cytokeratin-7
CK8	Cytokeratin-8
CNAs	Copy Number Alterations
CreER	Causes Recombination Estrogen Receptor
CRISPR	Clustered Regularly Interspaced Short Palindromic Repeats
CTLA-4	Cytotoxic T-lymphocyte–associated antigen 4
DMEM	Dulbecco's Modified Eagle Medium
DNA	Deoxyribonucleic Acid
ECM	Extracellular matrix
EPO-GEMM	Electroporation-based GEMM
FDR	False Discovery Rate
FMO	Fluorescence Minus One
FOXM1	Forkhead box protein M1
FTE	Fallopian tube epithelium
GEMMs	Genetically Engineered Mouse Models
GSEA	Gene Set Enrichment Analysis
H&E	Hematoxylin & Eosin
HGSOC	High-Grade Serous Ovarian Carcinoma
HR	Homologous Recombination
ICB	Immune Checkpoint Blockade
ISG	Interferon Stimulated Genes
IR	Ionizing Radiation
KEGG	Kyoto Encyclopedia of Genes and Genomes
LSL	Lox-Stop-Lox

MSKCC	Memorial Sloan-Kettering Cancer Center
NF-κB	Nuclear Factor kappa-light-chain-enhancer of active B-cells
OSE	Ovarian surface epithelium
OTTA	Ovarian Tumor Tissue Analysis
Pax-8	Paired Box 8
PARP	Poly (ADP-Ribose) Polymerase
PD-1	Programmed death 1
PI3K	Phospho-inositide 3-kinase
PBS	Phosphate Buffered Saline
PCR	Polymerase Chain Reaction
Rb	Retinoblastoma Protein
RNA	Ribonucleic Acid
RNA-seq	RNA-sequencing
SA-β-gal	Senescence-Associated β-Galactosidase
SASP	Senescence-Associated Secretory Phenotype
SB	Sleeping Beauty
sgRNA	Single guide RNA
shRNA	Short hairpin RNA
STIC	Serous tubular intra-epithelial carcinoma
STING	Stimulator of Interferon Genes
TNFa	Tumor Necrosis Factor alpha
TP53	Tumor Protein P53
VEGF	Vascular endothelial growth factor
WGS	Whole-Genome Sequencing
WT	Wild-Type
WT1	Wilms Tumor 1

INTRODUCTION

OVARIAN CANCER

Epidemiology of Human Ovarian Cancer

According to recently published cancer statistics, 21,750 new cases of ovarian cancer occur annually with the projected number of deaths being 13,940 in 2020 (Siegel, Miller, and Jemal 2020). Minimal improvement in survival has been observed over the past decades with overall survival being 45.6% (Jemal et al. 2011). However, stage at initial diagnosis greatly influences survival, which is more than 90% for patients with stage I cancer but less than 25 % for stage III and IV cancer (Siegel, Miller, and Jemal 2020). Ovarian cancer represents a global health problem. It is typically diagnosed at late stage and no effective screening strategies exist (Matulonis 2018).

Subtypes of Human Ovarian Cancer

Ovarian cancer can be subdivided into different histological subtypes. 90% of ovarian cancers are of epithelial origin and the remaining 10% are non-epithelial ovarian cancers, which include germ-cell and sex cord stromal tumors. The epithelial subtype can be further divided into serous, endometroid, clear cell and mucinous carcinomas. Of these, high-grade serous ovarian carcinoma (HGSOC) is the most common subtype (Matulonis 2018). Over 70% of women diagnosed with high-grade serous ovarian carcinoma (HGSOC) succumb to their disease, making it the deadliest gynecological disease (Bowtell et al. 2015).

Clinical Management of Human HGSOC

As there is no curative treatment for ovarian cancer, the primary aim of the treatment is to ensure cancer control and palliate disease symptoms. The standard of care for most patients consists of surgical debulking and platinum/taxane-based chemotherapy, though responses are typically transient, and resistance invariably emerges. Despite recent advances in targeted therapies such as Poly (ADP-ribose) polymerase (PARP) inhibitors and anti-angiogenic therapies, survival has only marginally improved in the past 30 years (Bowtell et al. 2015). Moreover, immune checkpoint blockade (ICB), which has revolutionized the treatment of several cancer types (Brahmer et al. 2015; Wolchok et al. 2017; Borghaei et al. 2015), shows only modest results in HGSOC (Liu and Zamarin 2018; Disis et al. 2016; Matulonis et al. 2019). Little is known about molecular mechanisms that dictate response or resistance to any of these modalities.

Cell of origin of HGSOC

As the disease is usually diagnosed after metastasizing through the peritoneal cavity (Peres et al. 2019), the identification of the cell of origin of HGSOC remains controversial (Karnezis et al. 2017; Klotz and Wimberger 2017). While initially the ovarian surface epithelium (OSE) was believed to be the tissue of origin (Scully 1995), attention later turned to the fallopian tube epithelium (FTE). This is supported by the presence of serous tubular intra-epithelial carcinomas (STICs) in many patients, which were initially discovered in BRCA1/2-mutant patients undergoing risk-reducing surgical removal of the reproductive tract (Jarboe et al.

2008) but were later found in more than half of sporadic HGSOC cases (Labidi-Galy et al. 2017). Current evidence from clinical and pre-clinical studies suggest that both the OSE and FTE could act as the cell of origin for HGSOC (D. Hao et al. 2017; Shuang Zhang et al. 2019; Lawrenson et al. 2019). As the cell of origin can impact cellular growth, metastatic patterns, transcriptional expression, and chemotherapy response (Shuang Zhang et al. 2019), determining the correct cell of origin is required for determining optimal treatment strategies.

Understanding of Ovarian Cancer from its Molecular Basis

The Cancer Genome Atlas and similar mapping projects have characterized the molecular composition of HGSOC, which is a cancer of TP53 mutations, genomic instability, DNA repair defects and copy number alterations (Patch et al. 2015; Cancer Genome Atlas Research Network 2011). The molecular complexity, absence of druggable driver mutations and high rate of copy number alterations complicate the development of effective therapies for HGSOC.

The disease is characterized by an almost universal appearance of *TP53* mutations. The p53 protein is a transcription factor that responds to a variety of cellular stress signals, including oncogenic stress and DNA damage. Upon activation, p53 transcriptionally activates a large number of genes involved in various tumor suppressive programs, including cellular senescence, cell cycle arrest and cell death (Lane and Levine 2010). While inactivation of p53 function contributes to tumorigenesis, the majority of cancer-associated alterations in the *TP53* gene are missense mutations, some of which endow p53 with gain-of-

function activities (Brosh and Rotter 2009). The rare proportion of patients without a *TP53* mutations often display copy number gains of negative regulators of p53, including *MDM2* or *MDM4* (Ahmed et al. 2010).

Another defining feature of HGSOC is inactivating mutations in genes important for homologous recombination (HR) DNA repair, which occur in around one third of HGSOC patients (Shiyu Zhang et al. 2011). HR defects are associated with either germline or somatic BRCA mutations, as well as mutations in other DNA repair pathway genes, including genes of the Fanconi anaemia pathway (*RAD51C*, *RAD51D*, *BRIP1*, *PALB2* and *BARD1*) and the DNA mismatch repair pathway (*MSH2*, *MSH6*, *MLH1* and *PMS2*). *BRCA1* is required for cell cycle checkpoint control, chromatin remodeling, transcriptional regulation, and DNA repair. *BRCA*2 is involved in homologous recombination and DNA repair (O'Donovan and Livingston 2010). In addition to mutation, promoter hypermethylation of the BRCA1 locus has been commonly detected in HGSOC patients, but does not influence outcome (Cancer Genome Atlas Research Network 2011). HR-deficient tumors display an even greater degree of genomic rearrangements than HR-proficient tumors (Y. K. Wang et al. 2017). While HR deficiency appears to sensitize tumors to platinum-based therapies and PARP inhibitors (Ashworth 2016), little is known about the cellular and molecular mechanisms that contribute to these therapeutic responses. HR mutations may also sensitize tumors to immune-modulating agents in some cancers, but it is unclear to what extent this process plays a role in HGSOC (Liu et al. 2020; Keenan, Burke, and Van Allen 2019).

Additional pathways that are recurrently altered in HGSOC by mutations or more commonly copy number alterations include RAS–MEK, phospho-inositide 3-kinase (PI3K), Notch and forkhead box protein M1 (FOXM1) signaling pathways. Moreover, HGSOC has been divided into four subtypes (proliferative, differentiated, immunoreactive and mesenchymal) using gene expression data. However, this subdivision has not been useful for clinical management (Verhaak et al. 2013).

Tumor microenvironment of HGSOC

An emerging field of research in HGSOC pathogenesis is the influence of the tumor microenvironment on tumor progression and treatment response. Several studies have demonstrated that infiltration of cytotoxic T cells correlates with improvement in overall survival (Hwang et al. 2012; Lin Zhang et al. 2003). Ovarian cancer patients harbor various endogenous mechanisms that can eradicate cancer cells. Tumor-reactive antibodies and T cells are detected in ovarian cancer tissue, ascites and blood (Schlienger et al. 2003; Zsiros et al. 2014). However, these antitumor immune processes are often suppressed. T cell function is dampened by negative regulators, like checkpoints cytotoxic T-lymphocyte–associated antigen 4 (CTLA-4) and programmed death 1 (PD-1) receptors (Odunsi 2017). While CTLA-4 inhibits the priming phase in lymphoid organs, PD-1 inhibits the effector phase in the tumor tissue (Wolchok et al. 2013). ICB exploits these mechanisms to treat cancer by re-activating the immune system. While an early study of PD-1 blockade showed promising results in

ovarian cancer (Hamanishi et al. 2015), this could not be recapitulated in larger phase Ib and II trials, in which objective response rates ranged from 8 to 10% with a small increase in median progression-free survival of just 2 months (Disis et al. 2019; Matulonis et al. 2019).

In addition to cellular immune mechanisms, angiogenesis plays a role in the pathogenesis of ovarian cancer. Pro-angiogenic signals mediated by vascular endothelial growth factor (VEGF) contribute to tumor growth and metastasis (X. Yang et al. 2015).

MOUSE MODELS OF OVARIAN CANCER

Relating clinical observations to mechanisms requires the availability of accurate and immune competent model systems. However, until recently, models that faithfully recapitulate the heterogeneity of human HGSOC have been limited. Figure 1 provides an overview of the advantages and disadvantages of different HGSOC models systems.

Cell line models

Commonly used models of ovarian cancer include peritoneal xenografts of human cells lines of uncertain origin or syngeneic murine transplantable models. Mouse OSE cells were shown to spontaneously transform *in vitro* by serial passaging (Roby et al. 2000). However, the most used spontaneously tumorigenic cell line, ID8, does not resemble mutations found in human patients (Greenaway et al. 2008). More suitable transplantable murine models were generated by genetic

engineering of the ID8 model (Walton et al. 2016). The first mouse model of ovarian cancer with defined genetic lesions was developed in 2002. This model required the *ex vivo* manipulation of OSE cells derived from p53-null mice with oncogene-overexpressing vectors (Orsulic et al. 2002).

Organoid models

More recently, both patient and murine HGSOC organoid models covering a range of genomic configurations have been developed, which enable perturbations *in vitro* or following orthotopic transplantation *in vivo* (Shuang Zhang et al. 2020; Lõhmussaar et al. 2020; Kopper et al. 2019; Hill et al. 2018; Maru et al. 2019). While these systems are flexible, time- and cost-efficient, they have limitations: the human models cannot be studied in the presence of the intact immune system and the murine models that employ *in vitro* transformed cells do not undergo immunoediting and lack other microenvironmental factors that shape tumor development *in vivo* (Binnewies et al. 2018; Wellenstein and de Visser 2018).

In vivo models

Genetically engineered mouse models (GEMMs), which are generated by intercrossing a series of tissue specific and/or conditional alleles and result in production of autochthonous tumors, have been used to study the consequences of cancer-associated mutations on HGSOC tumorigenesis (Morin and Weeraratna 2015). The first GEMM of epithelial ovarian cancer was developed in 2003 by

injecting Cre adenovirus into the ovarian bursa of mice with floxed p53 and Rb alleles. (Flesken-Nikitin et al. 2003). SV40-mediated models confirmed p53 and Rb being drivers of murine ovarian cancer (Szabova et al. 2012; Connolly et al. 2003; Sherman-Baust et al. 2014). To generate an FTE derived model, mice with floxed p53, Rb and Brca1 or Brca2 alleles were crossed to mice carrying a Cre recombinase driven by the fallopian tube specific Pax8 promoter (Perets et al. 2013). Recently, refined models that mimic the human ovarian tumor microenvironment have been reported (Maniati et al. 2020).

While such autochthonous models are powerful, they are time consuming, expensive, and the complex breeding programs and specific requirement for female mice leads to substantial animal waste. Moreover, most models are on a mixed background making them unsuitable for studies of tumor immunity. Consequently, it is impractical to develop animal cohorts of sufficient size and genotypic diversity to understand the behavior of different HGSOC subtypes in an immune-competent setting.

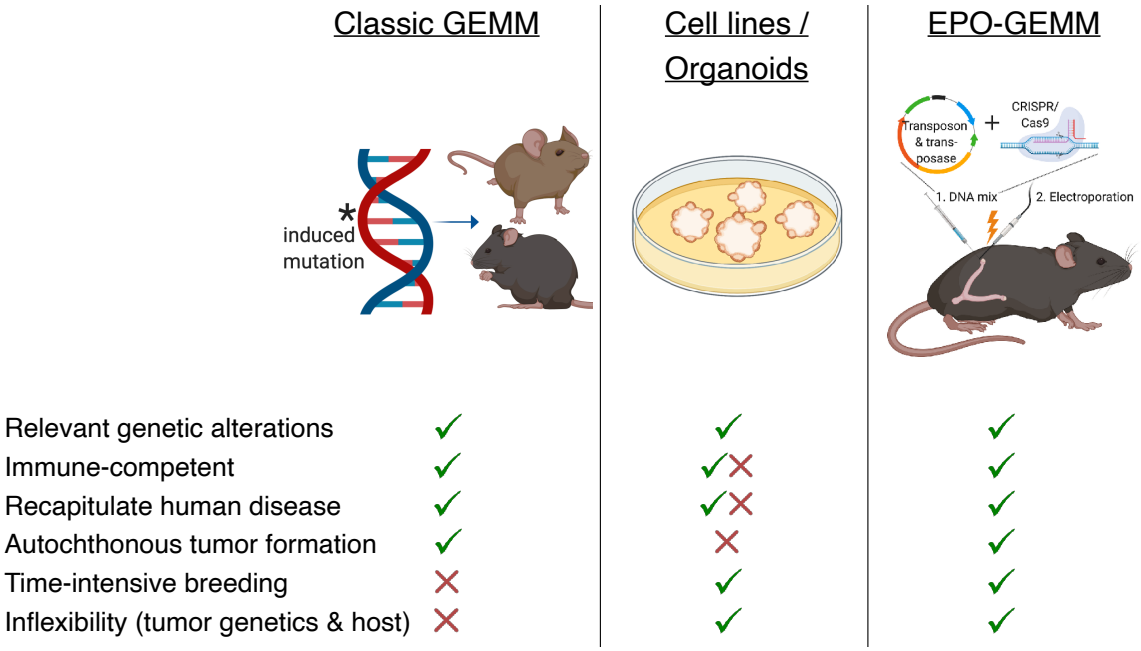

Figure 1: Overview of the advantages and disadvantages of HGSOC models systems.

While GEMMs model relevant genetic alterations in an autochthonous and immune-competent manner, they are very time- and cost-intensive and inflexible. Cell lines or organoids provide more flexibility, but do not mimic autochthonous tumor formation. The EPO-GEMM approach developed in this work overcomes the limitations of currently existing models.

SENESCENCE

In the lifetime of a cell, endogenous and exogenous factors result in an accumulation of DNA damage. Despite different layers of DNA damage repair, in certain instances the damage can be too much to repair and persists. One mechanism to prevent the negative impact of persistent damage on organ function and to counteract tumor development is the induction of a non-proliferative, but metabolically active state. This phenomenon, originally described in 1961 by Hayflick and Moorhead (Hayflick and Moorhead 1961), is termed cellular senescence. Senescence can be triggered by different intracellular stimuli, including telomere attrition4 (Fumagalli et al. 2012), oxidative stress (Moiseeva et al. 2009), endoplasmic reticulum stress (Pluquet, Pourtier, and Abbadie 2015) or oncogene induction (Serrano et al. 1997), and external stimuli, like depletion of nutrients (Carroll et al. 2017), pathogens (Lee et al. 2021) or DNA-damage inducing therapies (Wyld et al. 2020).

Hallmarks of Senescence

Senescent cells acquire several unique characteristics that distinguish them from normal cells (Hernandez-Segura, Nehme, and Demaria 2018). The most defining feature is a stable proliferation arrest, which is mediated by the activation of the cell cycle inhibitor genes *CDKN2A*, *CDKN1A* and *TP53* and heterochromatinization of proliferation genes. Further hallmarks include the upregulation of pro-survival pathways that results in resistance to apoptotic cell death, increased lysosomal activity, altered metabolism, loss of lamin B1 (a protein

of the nuclear envelope) and endoplasmic reticulum stress (Gorgoulis et al. 2019). A distinctive feature of senescent cells is that they secrete a plethora of soluble factors, a process termed senescence-associated secretory phenotype (SASP) (Coppé et al. 2008). The induction of senescence *in vivo* leads to the recruitment of immune cells via the SASP that results in clearance of premalignant senescent cells (Kang et al. 2011). The SASP can also reinforce the senescence phenotype through both autocrine and paracrine manners (Ritschka et al. 2017; Di Mitri and Alimonti 2016). A wide range of pro-inflammatory cytokines and chemokines, growth factors and extracellular matrix (ECM) degrading enzymes are components of the SASP (Coppé et al. 2008). Depending on the context, the SASP is activated by different transcriptional activators, including nuclear factor kappa B (NF-κB), CCAAT/enhancer-binding protein beta (CEBPB) (Kuilman et al. 2008; Chien et al. 2011) and the cyclic GMP-AMP synthase (cGas) / Stimulator of Interferon Genes (STING) pathway (Dou et al. 2017; Glück et al. 2017).

Biomarkers of Senescence

There is not one defined biomarker that characterizes a senescent cell (Sharpless and Sherr 2015). Various markers, including phosphorylation of the cell cycle regulator Rb, decrease of the proliferation marker Ki67, up-regulation of senescence-associated β-galactosidase (SA-β-gal) or the up-regulation and secretion of the SASP cytokines are common readouts to study senescence. Recently, multigene transcriptional signatures have been developed to describe the senescent cell state (Jochems et al. 2021). None of these markers are specific

or sufficient. For example, increased SA-β-gal activity is also found in non-senescent macrophages (Hall et al. 2016) and some senescent cells do not increase SA-β-gal activity (Kuilman et al. 2010). Similarly, the SASP shows extensive heterogeneity depending on tissue type, senescence trigger and microenvironmental context (Hoare et al. 2016; Hernandez-Segura et al. 2017) and is not a universal feature of senescence, as senescence caused by p16 overexpression is not characterized by an altered SASP transcriptional program (Coppé et al. 2011).

Senescence in cancer treatment

Beneficial role of senescence

Many conventional anticancer drugs, including chemo- and radiotherapy, are potent inducers of senescence in cancer cells (Ewald et al. 2010; Chang et al. 1999; Gewirtz, Holt, and Elmore 2008; Schmitt et al. 2002). For example, platinum-based compounds trigger extensive DNA damage through DNA crosslinking that causes a senescent state (Rottenberg, Disler, and Perego 2021; Dasari and Tchounwou 2014). Given its growth limiting characteristic, senescence can act as a barrier of tumorigenesis and cancer progression. In addition to the cell-intrinsic feature of growth arrest, the SASP can also have antitumorigenic properties. It has been demonstrated to recruit cancer-fighting immune cells and improve the vasculature (Kuilman et al. 2008; Ruscetti et al. 2018; Ruscetti et al. 2020; Xue et al. 2007; Krizhanovsky et al. 2008; Lujambio et al. 2013; Kang et al. 2011).

Detrimental role of senescence

More recent results suggest that persistence of therapy-induced senescent cells can be detrimental in the long term. Lingering senescent cells and the accompanying secretion of SASP factors create a pro-inflammatory, but immunosuppressive microenvironment. For example, the recruitment of immunosuppressive immature myeloid cells inhibits T cells function in premalignant prostate cancer lesions (Di Mitri et al. 2014). Secretion of ECM remodeling factors increases cancer cell proliferation by increasing exposure to nutrients and mitogens (Rodier et al. 2009). Moreover, the SASP can promote angiogenesis that enhances cancer cell growth and an epithelial-to-mesenchymal transition that promotes metastatic spread (L. Yang, Fang, and Chen 2017; Ruhland et al. 2016; Rodier et al. 2009).

In sum, the role of senescence and SASP in tumorigenesis appears to be highly context dependent. It varies depending on the timing and dynamic features of the cellular response, the nature of the inducing stimuli, the cell types undergoing senescence, and the surrounding in which it takes place (Faget, Ren, and Stewart 2019). Experimental evidence suggests that senescent cells play a beneficial role in tumorigenesis in an acute setting but promote cancer progression and invasion when persistently present. These results highlight the need to develop immunocompetent models to study the senescence response *in vivo* in a flexible and dynamic fashion.

Selective elimination of senescent cells

While initially developed to fight age-related pathologies and improve health span (Childs et al. 2015; Baker et al. 2011; Baker et al. 2016; van Deursen 2014), senolytic therapeutics that selectively eliminate senescent cells could find applications in the cancer therapy settings. For example, the genetic depletion of p16-positive senescent cells decreases cancer relapse after chemotherapy-induced senescence (Demaria et al. 2017). More translatable strategies to eliminate lingering senescent cells include small molecule pharmacological agents, called 'senolytics', or immune response-mediated senolysis harnessing endogenous or synthetic immune components. Treatment of KRAS-mutant lung cancer with the combination of CDK4/6 and MEK inhibitors triggers senescence and a potent NK response that clears senescent tumor cells (Ruscetti et al. 2018). In pancreatic cancer, the same combination of drugs promotes infiltration of exhausted cytotoxic T cells. Combination with ICB reactivates the senolytic properties of the infiltrated T cells (Ruscetti et al. 2020). Recently, chimeric antigen receptor (CAR) T cells that target a surface molecule on senescent cells have been engineered (Amor et al. 2020).

While these results are a proof of concept that the immune system can be re-activated to clear senescent cells, the highly heterogeneous nature of senescence warrants further research to determine whether these processes can be harnessed in different contexts or tumor types.

OBJECTIVES

Considering the urgent need for more accurate and facile autochthonous models, we combined CRISPR genome engineering approaches with transposon/transposase-based systems and *in vivo* organ electroporation (EPO-GEMM) to model HGSOC in mice. The EPO-GEMM approach allows study of autochthonous tumors in an immune competent background while overcoming the logistical disadvantages of traditional GEMMs. Using this approach, we developed genetically and histopathologically accurate models of HGSOC and used them to gain mechanistic insights into genotype-dependent therapy responses to chemo- and immune-therapies. A better understanding of the biological and molecular mechanisms responsible for genotype-response patterns in human HGSOC are needed to use existing therapies to their greatest effect and develop novel strategies to overcome resistance.

MATERIALS AND METHODS

PRODUCTION OF EPO-GEMM TUMORS

8-12 weeks old wild-type (WT) C57BL/6, or transgenic CK8-CreER;LSL-Cas9-IRES-GFP female mice were anesthetized with isofluorane, and the surgical site scrubbed with a povidone-iodine scrub (Betadine) and rinsed with 70% alcohol. The target organ was accessed from the left flank, as this allowed for more readily stabilization of the organ for electroporation than when accessing it from the back. After opening the skin and peritoneum, the left ovary and oviduct were exteriorized. 25 µl of a plasmid mix (details in Table 1) were injected under the ovarian bursa using a 27.5 gauge syringe, which led to the formation of a round, liquid-containing bubble. Tweezer electrodes were tightly placed around this 'injection bubble'. Two poring pulses of electrical current (50 V) for 30 ms lengths at 450 ms intervals and five transfer pulses (60 V, 50 ms length, 450 ms intervals) were then applied using an *in vivo* electroporator (NEPAGENE NEPA21 Type II electroporator). After electroporation, the peritoneal cavity was rinsed with 0.5 ml of pre-warmed saline. After the procedure, the peritoneal cavity was sutured, and the skin was closed with skin staples. The mice were kept at 37 ºC until they awoke, and post-surgery pain management was done with injections of buprenorphine for the following three days. Tumor formation was assessed by ultrasound imaging and abdominal palpation, and tumors were isolated at a humane endpoint.

Animal studies

Mice were maintained under specific pathogen-free conditions, and food and water were provided ad libitum. Mice were purchased from Jackson laboratory. CK8-CreER (Van Keymeulen et al. 2011) male mice were crossed with LSL-Cas9-IRES-GFP female mice to produce CK8-CreER;LSL-Cas9-IRES-GFP female mice for the generation of EPO-GEMMs. All mouse experiments were approved by the Memorial Sloan-Kettering Cancer Center (MSKCC) Internal Animal Care and Use Committee.

DNA constructs for electroporation

The Sleeping Beauty transposase (SB13) and the pT3 transposon vector were a generous gift of Dr. Xin Chen, UCSF San Francisco. The pX330 vector was a gift from Feng Zhang (Addgene plasmid # 42230). Table 2 provides the sgRNA sequences used in this study.

Ultrasound and bioluminescence imaging

High-contrast ultrasound imaging was performed on a Vevo 2100 System with a MS250 13- to 24-MHz scanhead (VisualSonics) to stage and quantify ovarian EPO-GEMM tumor burden. Tumor volume was analyzed using Vevo LAB software.

For visualizing ovarian tumor cells with luciferase, luciferase-blasticidin (Luc-Blast) constructs were cloned into MSCV-based vectors, and retroviruses were packaged by co-transfection of Gag-Pol expressing 293 T cells with expression

constructs and envelope vectors (VSV-G) using the Lipofectamine method (Thermo Fisher). Following transduction, cells were selected with Blasticidin S (10 μg/ml; Life Technologies) for 5 days. Bioluminescence imaging was used to track luciferase expression in tumor cells expressing the Luc-Blast reporter. Mice were injected intraperitoneally (ip) with luciferin (5 mg/mouse; Gold Technologies) and then imaged on a Xenogen IVIS Spectrum imager (PerkinElmer) 10 minutes later for 30 s. Quantification of luciferase signaling was analyzed using Living Image software (Caliper Life Sciences).

PRECLINICAL DRUG STUDIES

For preclinical treatment studies, EPO-GEMM mice were monitored for tumor development by palpation or ultrasound and randomized into treatment groups. For subcutaneous studies, EPO-GEMM derived cell lines were resuspended in Matrigel (BD Biosciences) and injected in the subcutaneous space. Following inoculation, mice were monitored three times a week. Caliper measurements began when tumors became visible. Tumor volume was calculated using the following formula: tumor volume = $(D \times d^2)/2$, in which D and d refer to the long and short tumor diameter, respectively. When tumors reached a size of 100-150 mm^3, mice were randomized based on starting tumor volume and enrolled into treatment groups. Tumor size and mouse weights were recorded three times weekly. Experimental endpoints were achieved when tumors reached 2000 mm^3 or became ulcerated. For ip studies, 1 to 2.5 million cells of EPO-GEMM derived cell lines carrying a luciferase reporter were resuspended in PBS and injected into the

ip space in a volume of 200 µl. Tumor volume was monitored using IVIS imaging and mice were randomized based on starting tumor signal.

Mice were treated with vehicle or cisplatin (3 mg/kg body weight) by ip injection once a week. Anti-PD-1 antibody (200mg/mouse; RMP1-14, BioXCell) was given 3 times per week ip alone or in combination with cisplatin. No obvious toxicities were observed in vehicle- or drug-treated animals as assessed by changes in body weight. Upon sacrifice, ovarian tumor tissue was allocated to either 10% formalin fixation, flow cytometry analysis on fresh tissue or snap frozen for DNA/RNA analysis.

CHARACTERIZATION OF EPO-GEMM TUMORS

Histopathological features of EPO-GEMM primary tumors and metastases were assessed by a trained veterinary pathologist (J. Wilkinson) and their relationship to human HGSOC was determined by immunohistochemistry for relevant markers and through bulk RNA-sequencing of tumor tissue. Tumors were shown to harbor intended lesions using Sanger Sequencing of the CRISPR-Cas9 induced scar and immunoblotting for MYC. Tumor clonality was analyzed using next-generation DNA sequencing of the p53 amplicon and sparse whole genome sequencing was used to characterize CNA (Baslan et al. 2012; Baslan et al. 2015). Flow cytometry was performed to evaluate tumor immune infiltration.

Clonality analysis of EPO-GEMM tumors

Genomic DNA was isolated from EPO-GEMM tumors using QIAGEN DNeasy Blood and Tissue kit following manufacturer's instructions. The p53 locus was amplified using a 50 µl reaction following standard Q5 High Fidelity Master Mix (NEB) protocol (forward primer: CAGAAGATATCCTGGTAAGG, reverse primer: CTACAGGCTGAAGAGGAACC). Amplicons were confirmed on a 2% agarose gel and PCR purified using QIAGEN QIAquick PCR purification kit. DNA concentration were measured using Nanodrop and samples were normalized to 20 ng/µl and sequenced using EZ-amplicon sequencing (MiSeq, 2 x 250 bp by GENEWIZ, Inc, South Plainfield, NJ, USA).

CNA inference

1 µg of bulk genomic DNA (gDNA) was extracted from ovarian tumors and tissue using the DNeasy Blood & Tissue Kit (Qiagen) and sonicated using the Covaris instrument. Sonicated DNA was subsequently end-repaired/A-tailed, followed by ligation of TruSeq dual indexed adaptors. Indexed libraries were enriched via PCR and sequenced in multiplex fashion using the Illumina HiSeq2500 instrument to achieve roughly 1 million uniquely mappable reads per sample – a read count sufficient to allow copy number inference to a resolution of approximately 400kb. For data analysis, uniquely mapped reads were counted in genomic bins corrected for mappability. Read counts were subsequently corrected for GC content, normalized, and segmented using Circular Binary Segmentation (CBS).

Segmented copy number calls are illustrated as relative gains and losses to the median copy number of the entire genome.

Tumor RNA-sequencing (RNA-seq)

For RNA-seq analysis of the transcriptional profiles of EPO-GEMM ovarian tumors, as well as normal ovaries of WT C57BL/6 mice, total RNA was extracted from bulk tissue using the RNeasy Mini Kit (Qiagen). Purified polyA mRNA was subsequently fragmented, and first and second strand cDNA synthesis performed using standard Illumina mRNA TruSeq library preparation protocols. Double stranded cDNA was subsequently processed for TruSeq dual-index Illumina library generation. For sequencing, pooled multiplexed libraries were run on a HiSeq 2500 machine on RAPID mode. Approximately 10 million 76bp single-end reads were retrieved per replicate condition. Resulting RNA-seq data was analyzed by removing adaptor sequences using Trimmomatic (Bolger, Lohse, and Usadel 2014), aligning sequencing data to GRCm38.91(mm10) with STAR (Dobin et al. 2012), and genome wide transcript counting using featureCounts (Anders, Pyl, and Huber 2015) to generate a TPM matrix of transcript counts. Genes were identified as differentially expressed using R package DESeq2 with a cutoff of absolute log2(fold change) ≥ 1 and adjusted p-value < 0.05 between experimental conditions (Love, Huber, and Anders 2014).

Clustering and Gene Set Enrichment Analysis (GSEA)

Principal component analysis was performed using the DESeq2 package in R. Gene expressions of RNA-seq data were clustered using hierarchical clustering based on one minus pearson correlation test. For pathway enrichment analysis, the weighted GSEA Preranked mode was used on a set of curated signatures in the molecular signatures database (http://www.broadinstitute.org/gsea/msigdb/index. jsp, MSigDB v7.0). From 22,596 signatures, signatures with 15-500 genes were considered for further analyses. From the results, enriched signatures with an adjusted p-value less than 0.05 were considered as statistically significant. Hallmark and Kegg pathways were used to run GSEA on our murine EPO-GEMM models and human patient data (Pearce et al. 2018), and $-\log_{10}$(FDR) values were plotted in the XY plot.

Immunohistochemistry and immunofluorescence

Tissues were fixed overnight in 10% formalin, embedded in paraffin, and cut into 5 μm sections. Haematoxylin and eosin (H&E), immunohistochemical and immunofluorescence stainings were performed using standard protocols. Sections were de-paraffinized, rehydrated, and boiled in a microwave for 15 minutes in 10 mM citrate buffer (pH 6.0) for antigen retrieval. Antibodies were incubated overnight at 4ºC. Primary antibodies are listed in Table 3. HRP-conjugated secondary antibodies (Vectastain Elite ABC HRP Kits) were applied for 30 minutes and visualized with DAB (Vector Laboratories; SK-4100), or secondary Alexa Fluor 488 or 594 dye-conjugated antibodies (Life Technologies) applied for 1 hour at

room temperature. Fluorescence antibody-labeled slides were mounted with Prolong Gold Antifade mountant (Prolong Molecular Probes; P36934) after counterstaining with DAPI.

Flow Cytometry

To prepare single cell suspensions for flow cytometry analysis, tumors were minced with a razorblade into small pieces and placed in 5 ml of pre-warmed collagenase buffer (1x HBSS with calcium and magnesium (GIBCO), 2 mg/ml Collagenase D (11088858001; Sigma), 0.1 mg/ml DNase I (DN25; Sigma)). Samples were then transferred to C tubes and processed using program 37C_m_TDK1_1 on a gentleMACSC Octo dissociator with heater (Miltenyi Biotec). Dissociated tissue was filtered through a 70 µm cell strainer and centrifuged at 1500 rpm for 5 minutes. Samples were resuspended in FACS buffer (1x PBS, 2% FBS, 2 mM EDTA) and 3 x 10^6 cells were seeded in a U-bottom 96-well plate. Samples were blocked with anti-CD16/32 (FC block, BD Pharmigen) for 10 minutes and then incubated with antibodies for 30 minutes on ice. In each experiment, a myeloid and a lymphoid panel were set up. The antibodies used for flow cytometry are provided in Table 4 and 5. Gates were set using fluorescence minus one (FMO) controls. Flow cytometry was performed on a LSR Fortessa or LSR II flow cytometer, and data were analyzed using FlowJo (TreeStar).

EPO-GEMM CELL LINE GENERATION

For cell line generation, a tumor piece was minced with a razorblade into small pieces, placed in 5 ml of pre-warmed collagenase V buffer (1 µg/ml, Sigma-Aldrich) and incubated at 37ºC for 30 minutes. Dissociated tissue was washed once with PBS, filtered through a 70 µm cell strainer and centrifuged at 1500 rpm for 5 minutes. Cells were plated on 10-cm culture dishes coated with 100 µg/mL collagen (PureCol; 5005; Advanced Biomatrix). Primary cultures were passaged at least three times to remove fibroblast contamination. All ovarian cancer cell lines were maintained in a humidified incubator at 37°C with 5% CO_2 and grown in DMEM supplemented with 10% FBS and 100 IU/mL penicillin/streptomycin. All cell lines used in this study tested negative for *Mycoplasma*. Cell lines were validated to carry the correct genotype, and to have tumor initiating capabilities following subcutaneous and ip injection. Multiple tumor-derived cell lines were confirmed to produce consistent treatment response patterns *in vitro*.

CHARACTERIZATION OF CELLULAR SENESCENCE AND CGAS/STING RESPONSE

Assays to evaluate cellular senescence involved senescence-associated beta-galactosidase (SA-β-gal) staining (Krizhanovsky et al. 2008) and replating assays after drug withdrawal. SASP profiles were assessed using murine cytokine arrays (Eve Technologies) and RT-qPCR. Micronuclei were visualized and quantified by nuclear DAPI staining. The DNA damage response was determined using immunofluorescence for 53BP1, γH2AX, and Rad51 (Hill et al. 2018). The role of

the cGas/STING pathway was assessed by transducing cells with two independent cGas shRNAs validated for knockdown and compared to a well-established control shRNA.

Senescence-associated beta-galactosidase staining

Senescence-associated beta-galactosidase (SA-β-gal) staining was performed as previously described at pH 5.5 for mouse cells and tissue and pH 6 for human cells (Krizhanovsky et al. 2008). Fresh frozen ovarian tumor sections, or adherent cells plated in 6-well plates, were fixed with 0.5% glutaraldehyde in PBS for 15 minutes, washed with PBS supplemented with 1mM $MgCl_2$, and stained for 18-24 hours in PBS containing 1 mM $MgCl_2$, 1 mg/ml X-Gal, and 5 mM each of potassium ferricyanide and potassium ferrocyanide. Tumor tissue sections were counterstained with eosin. For the fluorescent SA-β-gal labelling, frozen sections were incubated in 300 μM chloroquine solution for 30 minutes at 37ºC followed by exposure to the C12RG substrate (ImaGene Red C12RG *lacZ* Gene Expression Kit, Molecular Probes, I2906) for 2 hours at 37°C. The reaction was stopped by addition of 1 μM PETG. Slides were fixed with 4% PFA for 10 minutes at room temperature. 5 high power fields per well/section were counted and averaged to quantify the percentage of SA-β-gal$^+$ cells.

Cytokine array

EPO-GEMM derived ovarian cancer cell lines were plated in 6-well plates and treated for 48h with vehicle or cisplatin at IC50 concentrations. Conditioned media

was collected, and the cells were trypsinized and counted using a cellometer (Nexcelom Biosciences). Conditioned media samples were normalized based on cell number by diluting with complete DMEM. 50 µl aliquots of the conditioned media were analyzed using multiplex immunoassays (Mouse Cytokine/Chemokine Array 31-Plex) from Eve Technologies. Biological replicates were averaged to determine cytokine levels.

Micronuclei quantification

Cells were seeded on chamber slides. Following vehicle or cisplatin treatment, the cells were washed and fixed in 4% formaldehyde/PBS for 10 minutes at room temperature. For confocal microscopy, cells were mounted on coverslips using ProLong Gold antifade reagent with DAPI counterstaining (#P36935, Life Technologies). Images were analyzed using ImageJ/Fiji software.

IN VITRO CELL ASSAYS

For knockdown studies, two independent MiRE-based shRNAs targeting *cGas* (shcGas1: CGAAGAAGTTAAAGAAATCAAA, shcGas2: CTCGAAGAAAATT GAATATGAA) were cloned into MSCV-based vectors as described previously (Chicas et al. 2010). An shRNA targeting *Renilla* was used as a control (Saborowski et al. 2014). Following transduction with shRNA retroviral constructs, cell selection was performed with 4 µg/mL puromycin for 3 days. Knockdown efficiency was evaluated by RT-qPCR.

For cell viability assays, two thousand cells were plated in 100 µl of media per well of a black-walled 96-well plate (Perkin Elmer). The next day, media was changed, and cells were treated with drugs for 72 hours. Following treatment, cell viability was assessed using the CellTiter-Glo Viability Assay (Promega) according to the manufacturer's protocol. IC_{50} calculations were made using Prism 6 Software (GraphPad Software). Drugs for *in vitro* studies were dissolved in DMSO. Growth medium with vehicle or drugs was changed every 3 days.

For drug withdrawal assays, cells were pretreated for 5-7 days with vehicle (DMSO) or cisplatin, and then replated (5 x 10^3 cells per well of 6-well plate) in the absence of drugs for 5 to 7 days. Relative growth was quantified with Crystal Violet staining.

Rad51 assay

Cells were irradiated with a 10 Gy dose of ionizing radiation (IR) and allowed to recover for 4 hr. Cells were fixed with 4% solution of formaldehyde in PBS for 30 min and permeabilized in 0.2% Triton X-100 in PBS^{++} (PBS solution containing 1 mM $CaCl_2$ and 0.5 mM $MgCl_2$) for 20 min. For blocking, cells were incubated for 30 min in staining buffer (1% BSA, 0.15% glycine and 0.1% Triton X-100 in PBS^{++}). Cells were incubated with primary RAD51 antibody (70-001, BioAcademia, 1:5000) in staining buffer for 2h at room temperature followed by incubation of fluorophore-conjugated secondary antibody for 1h at room temperature. Samples were mounted with Prolong Gold Antifade mountant (Prolong Molecular Probes;

P36934) after counterstaining with DAPI. RAD51 foci were quantified with ImageJ/Fiji software.

RT-qPCR

Total RNA was extracted from cell lines treated with vehicle or cisplatin for 48h using the RNeasy Mini Kit (QIAGEN). Complementary DNA (cDNA) was obtained using the TaqMan reverse transcription reagents (Applied Biosystems). Real-time quantitative PCR was performed in duplicate or triplicate using SYBR Green PCR Master Mix (Applied Biosystems) on the ViiA 7 Real-Time PCR System (Invitrogen). Expression was calculated using the ΔΔCt method, *Gapdh* served as an endogenous normalization control. Table 6 indicates the primer sequences used for RT-qPCR.

HUMAN CELL LINE AND TUMOR ANALYSES

UWB1.289, UWB.289+BRCA1, MDA-MB-231 and MDA-MB-436 cell lines were purchased from ATCC and cultured according to instructions. CBioPortal.org was used to plot the frequency of mutations, amplifications, and/or deletions in genes of interest in HGSOC patients from various datasets. To evaluate senescence signatures in human tumor samples, senescence signatures were derived from KEGG and previously published works (Tasdemir et al. 2016; Ruscetti et al. 2018). TPM (Transcripts Per Million) normalized expression data were used to calculate geometric mean score as the senescence signature scores.

STATISTICS

Statistical analyses were performed as described in the figure legend for each experiment. Group size was determined based on the results of preliminary experiments and no statistical method was used to predetermine sample size. The indicated sample size (*n*) represents biological replicates unless otherwise stated. Group allocation and outcome assessment were not performed in a blinded manner. All samples that met proper experimental conditions were included in the analysis. Survival was measured using the Kaplan–Meier method. Statistical significance was determined by one-way ANOVA, Student's t test, log-rank test, Pearson's correlation, or Wilcoxon signed-rank test using Prism 6 software (GraphPad Software) as indicated. Significance was set at $P<0.05$.

FIGURE PREPARATION

Figures were prepared using BioRender.com for scientific illustrations and Illustrator CC 2020 (Adobe).

Table 1: Overview of electroporation plasmid mixes

Mouse Strain	***Plasmid Mix***	***Genotype***
WT C57BL/6	20 µg sg*Trp53*/sg*Pten* Cas9 pX330 vector 20 µg sg*Rb* Cas9 pX330 vector	PPtRb
WT C57BL/6	20 µg sg*Trp53/Pten* Cas9 pX330 vector	PPt
WT C57BL/6	20 µg sg*Trp53* Cas9 pX330 vector	p53_only
WT C57BL/6	1 µg SB13 transposase 5 µg *MYC* transposon vector 20 µg sg*Trp53* Cas9 pX330 vector	MP
WT C57BL/6	1 µg SB13 transposase 5 µg *MYC* transposon vector 20 µg sg*Trp53*/*Brca1* Cas9 pX330 vector	MPB1
CK8-CreER;LSL-Cas9-IRES-GFP	1 µg SB13 5 µg *MYC* transposon vector 20 µg sg*Trp53* vector	CK8-MP

Table 2: sgRNA sequences

Gene	***sgRNA sequence***
p53	ACCCTGTCACCGAGACCCC
Pten	GTTTGTGGTCTGCCAGCTAA
Rb	TGCGCGGGGTCGTCCTCCCG
Brca1_1	TGTTATCCAAGGAACATCGG
Brca1_2	GCAGCAGGAAATGGCTCACC

Table 3: Primary antibodies for IHC and IF

Antigen	***Manufacturer and catalogue number***
MYC	Abcam AB32072
Wilms-Tumor 1	Abcam AB89901
Cytokeratin-7	Abcam AB181598
Granzyme B	Abcam AB4059
Ki67	Abcam AB16667
Cancer antigen 125	Abbiotec 250566
Pax8	Proteintech 10336
CD8	Ebioscience 4SM15
Cleaved Caspase3	Cell Signaling 9664
γH2AX	Millipore JBW301
53BP1	Novus Biologicals NB100-305

Table 4: Antibodies used for flow cytometry analysis (myeloid panel)

Antigen	***Fluorophore***	***Company***	***Clone #***	***Catalogue #***
CD45	AF700	Biolegend	30-F11	103128
CD3	BUV737	BD	17A2	612803
Ly6G	BV605	BD	1A8	563005
SIGLECF	PerCp-Cy5.5	BD	E50-2440	565526
LY6C	APC-C7	Biolegend	HK1.4	128026
CD11b	BUV395	BD	M1/70	563553
CD11c	BV785	Biolegend	N418	117335
MHCII	AF488	Biolegend	M5/114.15.2	107616
F4/80	PE-eFluor610	ThermoFisher	BM8	61-4801-82
CD19	BV650	BD	1D3	563235
CD103	PE	Biolegend	2E7	121405
PD-L1	APC	Biolegend	10F.9G2	124312
CD80	BV421	Biolegend	16-10A1	104725
CD206	BV711	Biolegend	C068C2	141727
Viability	eFluor506	ThermoFisher	-	65-0866-18

Table 5: Antibodies used for flow cytometry analysis (lymphoid panel)

Antigen	*Fluorophore*	*Company*	*Clone #*	*Catalogue #*
CD45	AF700	Biolegend	30-F11	103128
CD3	AF488	Biolegend	17A2	100210
CD4	BUV395	BD	GK1.5	563790
CD8	PECy7	Biolegend	53-6.7	100722
CD25	BV605	Biolegend	PC61	102035
CD69	Percp-Cy5.5	Biolegend	H1.2F3	104522
CD62L	BV421	BD	MEL-14	562910
CD44	ApC-Cy7	BD	IM7	560568
PD1	PE	Biolegend	29F.1A12	135206
NK1.1	APC	Biolegend	PK136	108710
TIM3	BV711	Biolegend	RMT3-23	119727
LAG3	BV650	Biolegend	C9B7W	125227
KLRG1	BV785	Biolegend	2F1	138429
Viability	eFluor506	ThermoFisher	-	65-0866-18

Table 6: Primer sequences used for RT-qPCR

cGas_Fw	GAGGCGCGGAAAGTCGTAA
cGas_Rv	TTGTCCGGTTCCTTCCTGGA
Ccl5_Fw	ATATGGCTCGGACACCACTC
Ccl5_Rv	TCCTTCGAGTGACAAACACG
Cxcl10_Fw	CCCACGTGTTGAGATCATTG
Cxcl10_Rv	GTGTGTGCGTGGCTTCACT
IL6_Fw	ACCAGAGGAAATTTTCAATAGGC
IL6_Rv	TGATGCACTTGCAGAAAACA

RESULTS

SOMATIC INTRODUCTION OF ONCOGENIC LESIONS GENERATES HIGH-GRADE SEROUS OVARIAN CARCINOMA

To develop murine models of HGSOC that recapitulate the genetic heterogeneity observed in human disease, we optimized methods to introduce genetic elements into the ovary by direct tissue electroporation. Briefly, the ovary is surgically exposed and injected with plasmid DNA encoding CRISPR-Cas9 constructs and/or a transposon vector and a Sleeping Beauty transposase, followed by electroporation of the surrounding ovarian and fallopian tube tissue (**Fig. 2A**). Since more than 95% of HGSOC patients harbor tumors with mutations in the *TP53* tumor suppressor gene (Cancer Genome Atlas Research Network 2011), all genotypic configurations included vectors co-expressing Cas9 and a single-guide RNA (sgRNA) targeting *Trp53* that was previously validated *in vivo* (Leibold et al. 2020). In addition, various combinations of oncogene-expressing transposon vectors or sgRNAs targeting additional tumor suppressor genes that co-occur in human patients were included (**Fig. 2B**). Following electroporation, mice were monitored for tumor onset and progression by ultrasound imaging and abdominal palpation. To determine the extent to which our model recapitulates human HGSOC, murine tumor material was analyzed histologically for clinically relevant HGSOC biomarkers, and molecularly for CRISPR-Cas9-engineered somatic mutations, acquired copy number alterations and transcriptional profiles.

Our initial efforts to produce ovarian cancer in mice involved combining validated sgRNAs targeting *Trp53* with additional sgRNAs capable of inactivating *Pten* and/or *Rb* – two commonly disrupted tumor suppressors in HGSOC (**Fig. 2B)**. Since MYC gain or amplification often co-occurs with Tp53 mutations in human HGSOC and can be oncogenic in transplantation models (Karst, Levanon, and Drapkin 2011; Orsulic et al. 2002), we also combined *Trp53* sgRNAs together with a transposon vector overexpressing *MYC*. While *Trp53* disruption alone did not produce tumors over the time course of these experiments, focal tumors arose following electroporation of sgRNAs targeting *Trp53* and *Pten*, or *Trp53*, *Pten*, and *Rb1* produced tumors with 40% and 90% penetrance, respectively, with the latter configuration displaying a median survival of 214 days. Traditional GEMMs with comparable genetic configurations develop tumors with similar penetrance and latency (McCool et al. 2020; Perets et al. 2013; Zhai et al. 2017; Maniati et al. 2020). *MYC* overexpression was particularly potent, cooperating with *Trp53* loss to produce tumors in 100% of the recipients and vastly accelerate the disease (**Fig. 2C**, median survival 61 days).

Most mice developed metastatic disease to the omentum and peritoneum, which are the most common sites of metastatic spread in patients (Lengyel 2010). While tumors arising through the disruption of tumor suppressors only generated micro-metastatic nodules in the omentum (**Fig. 2D**), the addition of *MYC* resulted in macro-metastatic disease and ascites formation (**Fig. 2E**). As occurs in human HGSOC tumors (Kurman et al. 2014), EPO-GEMM tumors exhibited a solid

architecture with some glandular areas, necrosis in solid areas, large hyper-chromatic nuclei and abundant, often atypical, mitotic figures (**Fig. 2D-E**). Histologically, we never observed sarcomas or lymphomas arising in electroporated animals and, accordingly, all tumors analyzed expressed molecular hallmarks of human HGSOC, including Cytokeratin-7 (CK7), Wilms Tumor 1 (WT1), Cancer Antigen 125 (CA-125), Paired box 8 (Pax-8) and high Ki67 (**Fig. 2F and 2.1A**). These markers were mostly retained in metastases (**Fig. 2.1B**), with the exception of CK7 whose reduced expression at metastatic sites has been linked to poor prognosis in patients (Elloul et al. 2005). As expected, *MYC*-driven tumors showed high levels of MYC protein expression (**Fig. 2F**).

At the molecular level, Sanger sequencing analysis of the resulting tumors at terminal stage confirmed the presence of insertions and deletion mutations (indels) at the *Trp53*, *Pten* and *Rb1* loci, consistent with their disruption through CRISPR-Cas9 (**Fig. 2.1C**). Deep sequencing of the CRISPR-Cas9-induced p53 scar revealed that tumors were multiclonal and that the dominant clones were shared between ovarian tumors and paired omentum metastases, confirming that the disseminated cells arose from the primary tumor site (**Fig. 2.1D**). Analysis of copy number alterations using sparse whole-genome sequencing (WGS) (Baslan et al. 2015) of primary EPO-GEMM tumors revealed the presence of widespread aneuploidies that are characteristic of the human disease (Macintyre et al. 2018). Recurrent changes included loss of mouse chromosomes 10 and 12 and gains of chromosomes 1 and 2. Interestingly, some tumors generated by tumor suppressor

gene inactivation without *MYC* overexpression showed gain or amplification of the *Myc* locus on mouse chromosome 15 (**Fig. 2.1E**) and MYC protein expression (**Fig. 2.1F**), a genetic event also arising in a traditional GEMM with *Brca1*;*Trp53*;*Rb1*;*Nf1* genotype (McCool et al. 2020). These data underscore the importance of *MYC* in driving HGSOC and support the rationale for using *MYC* as a driver in our EPO-GEMM platform.

Analysis of RNA sequencing (RNA-seq) data derived from tumors demonstrated that the *MYC;p53* (MP) EPO-GEMM system faithfully recapitulates the transcriptional states characteristic of human disease (**Fig. 2G**). When compared to normal tissue, the top upregulated pathways in both the Hallmark and KEGG database were related to proliferation (Hallmark: E2F targets, Myc targets, G2M checkpoint; KEGG: Ribosome, spliceosome, oxidative phosphorylation) and DNA repair (Hallmark: DNA repair; KEGG: Base excision repair) and the top downregulated pathways were related to an active immune response (Hallmark: TNFa signaling via NFkB, inflammatory response; KEGG: Neuroactive ligand receptor interaction, cytokine receptor interaction). In line with the almost ubiquitous p53 inactivation in HGSOC, the p53 pathway was among the top downregulated pathways in the Hallmark gene sets. Collectively, these results validate the EPO-GEMM approach as a flexible platform to model HGSOC tumors of varying genotypes that resemble the metastatic, histological, genomic, and transcriptomic properties of the human disease.

The similarity of EPO-GEMM ovarian cancers to human HGSOC was striking, particularly given that our electroporation method does not discriminate between cell types within the targeted tissue.

To confirm that the tumors were, in fact, of epithelial origin, we took advantage of the flexibility of the EPO-GEMM approach to perform direct mutagenesis of Cytokeratin-8 (CK8)-expressing epithelial cells, a cell type that can serve as a tumor-initiating cell in the absence of p53 (Motohara et al. 2011) and is also retained in traditional GEMMs arising in *Brca1*;*Trp53*;*Pten* deficient mice (Perets et al. 2013). Double transgenic mice harboring a CRE-estrogen receptor fusion transgene (CreER) under the control of the CK8 promoter and a Lox-Stop-Lox (LSL) Cas9-IRES-GFP transgene were treated with tamoxifen and electroporated with vectors expressing a *MYC* transposon, a transposase and a p53 sgRNA. In this setting, only CK8-positive epithelial cells are capable of CRISPR-Cas9-mediated editing upon tamoxifen addition. (**Fig. 2.1G**). Tamoxifen treatment triggered expression of GFP in CK8-positive epithelial cells (**Fig. 2.1H**) and led to the formation of GFP-positive ovarian tumors with similar histological and transcriptional features observed in wild-type mice harboring tumors of the same genotype (**Fig. 2.1I-K**). These data confirm the epithelial origin of the EPO-GEMM tumors and imply that relevant epithelial populations in the ovary are most sensitive to the genetic alterations that co-occur in the human disease.

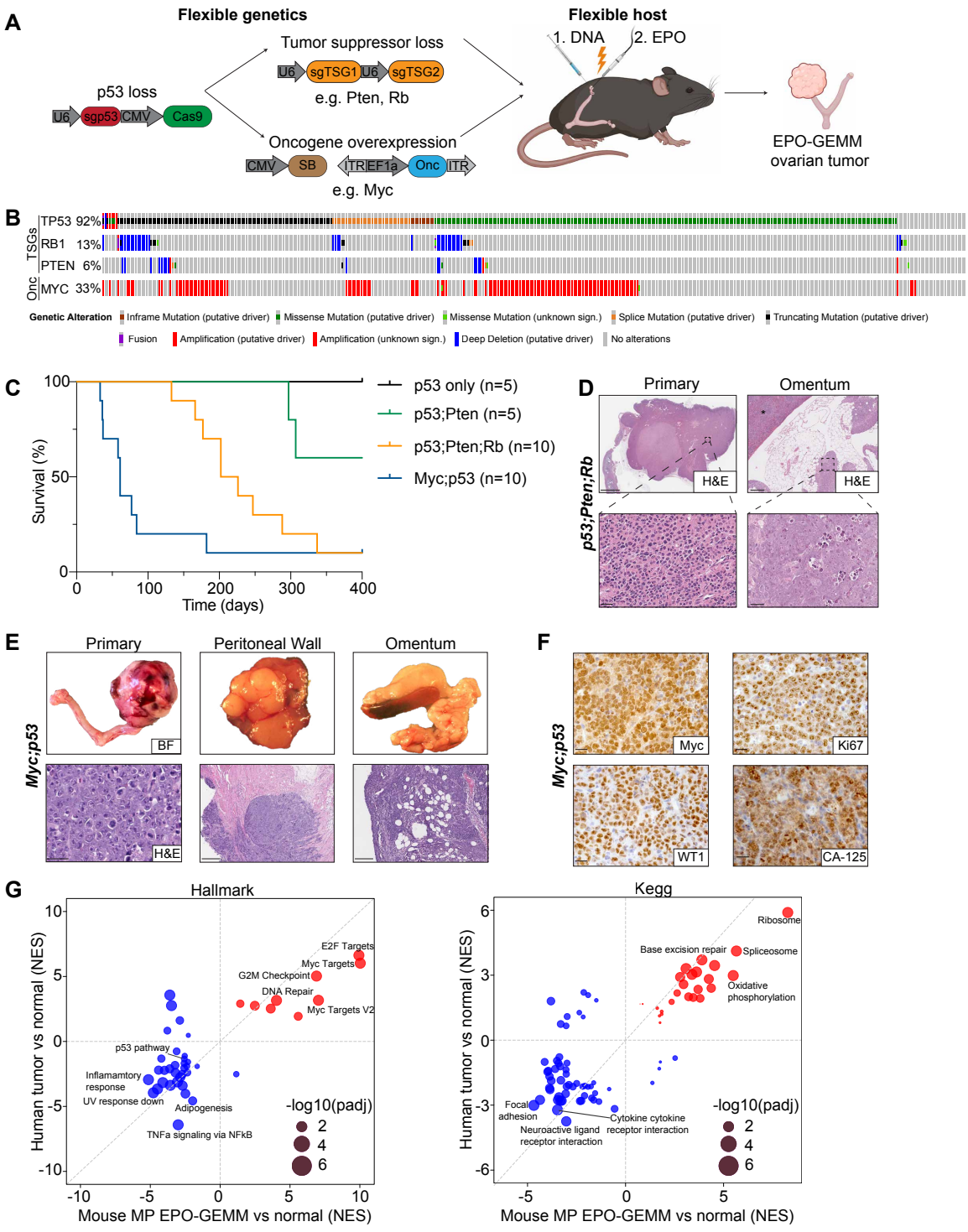
A
Flexible genetics
Flexible host
p53 loss
U6 sgp53 CMV Cas9
Tumor suppressor loss
U6 sgTSG1 U6 sgTSG2
e.g. Pten, Rb
Oncogene overexpression
CMV SB ITR EF1a Onc ITR
e.g. Myc
1. DNA
2. EPO
EPO-GEMM
ovarian tumor
B
TSGs
Onc
TP53 92%
RB1 13%
PTEN 6%
MYC 33%
Genetic Alteration
Inframe Mutation (putative driver)
Missense Mutation (putative driver)
Missense Mutation (unknown sign.)
Splice Mutation (putative driver)
Truncating Mutation (putative driver)
Fusion
Amplification (putative driver)
Amplification (unknown sign.)
Deep Deletion (putative driver)
No alterations
C
Survival (%)
Time (days)
p53 only (n=5)
p53;Pten (n=5)
p53;Pten;Rb (n=10)
Myc;p53 (n=10)
D
Primary
Omentum
p53;Pten;Rb
H&E
E
Primary
Peritoneal Wall
Omentum
Myc;p53
BF
H&E
F
Myc;p53
Myc
Ki67
WT1
CA-125
G
Hallmark
Human tumor vs normal (NES)
Mouse MP EPO-GEMM vs normal (NES)
E2F Targets
Myc Targets
G2M Checkpoint
DNA Repair
Myc Targets V2
p53 pathway
Inflamamtory response
UV response down
Adipogenesis
TNFa signaling via NFkB
-log10(padj)
Kegg
Ribosome
Base excision repair
Spliceosome
Oxidative phosphorylation
Focal adhesion
Cytokine cytokine receptor interaction
Neuroactive ligand receptor interaction

Figure 2. Somatic introduction of oncogenic lesions generates high-grade serous ovarian carcinoma.

(A) Schematic of the EPO-GEMM approach to generate ovarian cancer. A CRISPR-Cas9 vector targeting *Trp53* is co-delivered with additional sgRNAs targeting tumor suppressor genes (TSGs) or an oncogene (onc) transposon vector in combination with a Sleeping Beauty transposase (SB) into the ovary and fallopian tube by direct *in vivo* electroporation. **(B)** Oncoprint displaying the genomic status of *Trp53*, *Rb*, *Pten* and *MYC* in HGSOC (TCGA, Pan-cancer dataset). **(C)** Kaplan-Meier survival curve of C57BL/6 mice electroporated with the indicated combinations of plasmids. **(D)** Representative hematoxylin and eosin (H&E) staining of a PPtRb EPO-GEMM primary tumor (left) and omentum with a micrometastasis (right). Scale bar 5 mm (top left), 200 µm (top right), 50 µm (bottom left), 25 µm (bottom right). The spleen is labeled with an asterisk. **(E)** Macroscopic bright-field (BF) pictures (top) and H&E sections (bottom) of genital tracts, peritoneum and omentum of a mouse bearing a MP EPO-GEMM tumor. Scale bar 50 µm (bottom left), 500 µm (bottom middle and right). **(F)** Representative immunohistochemical staining of a MP EPO-GEMM ovarian tumor for MYC, the proliferation marker Ki67 and the HGSOC markers Wilms Tumor 1 (WT1) and Cancer Antigen 125 (CA-125) in representative sections. Scale bar 20 µm. **(G)** Correlation of GSEA normalized enrichment scores (NES) derived from RNA-seq data for Hallmark (left) or Kegg (right) pathways enriched in human ovarian cancer samples (y-axis) and murine EPO-GEMM ovarian cancer (x-axis) compared to normal tissue. Highlighted are key pathways, circle size represents the adjusted p-value.

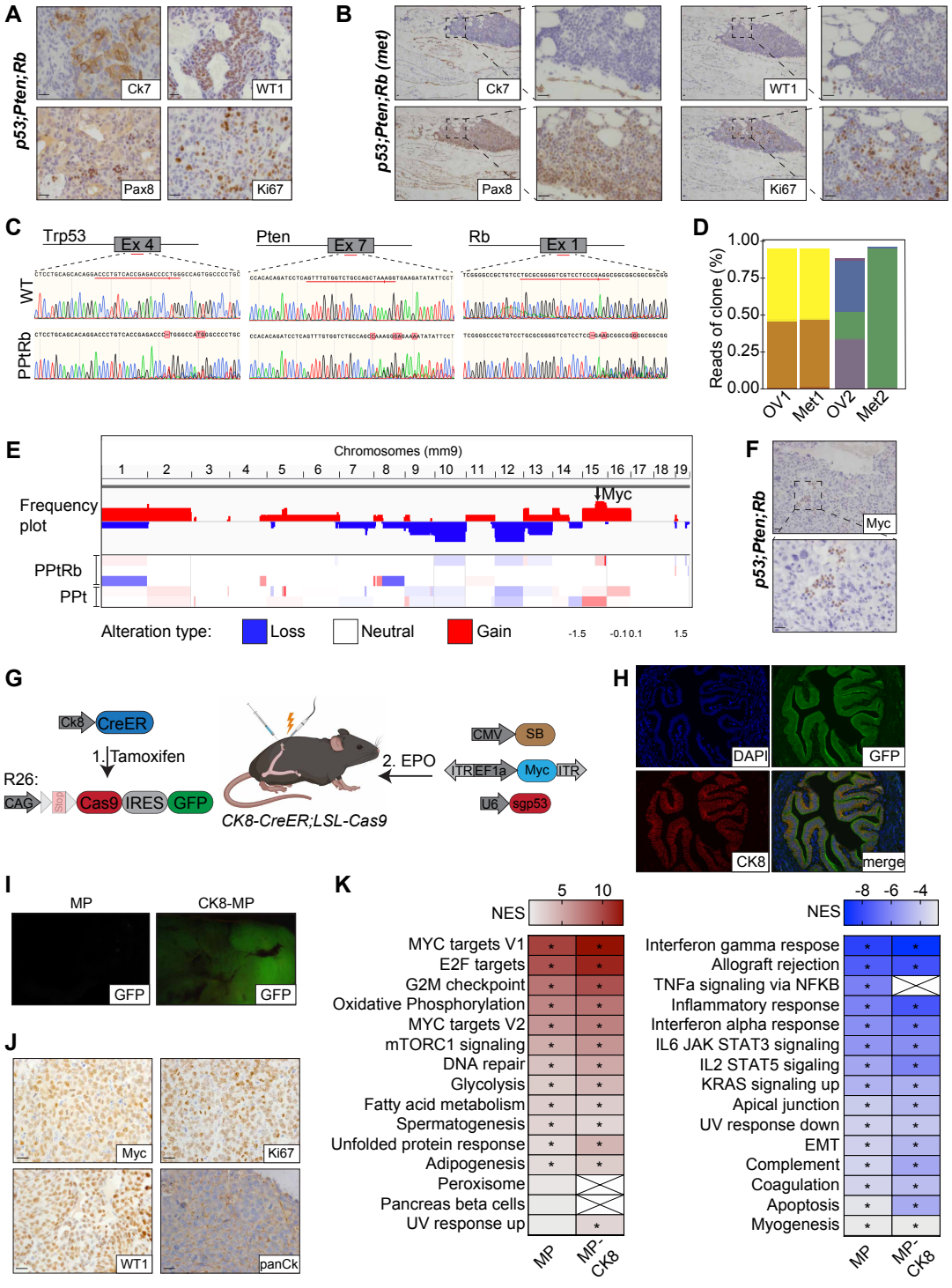
A
p53;Pten;Rb
Ck7
WT1
Pax8
Ki67
B
p53;Pten;Rb (met)
Ck7
WT1
Pax8
Ki67
C
Trp53
Ex 4
Pten
Ex 7
Rb
Ex 1
WT
PPtRb
D
Reads of clone (%)
1.00
0.75
0.50
0.25
0.00
OV1
Met1
OV2
Met2
E
Chromosomes (mm9)
1 2 3 4 5 6 7 8 9 10 11 12 13 14 15 16 17 18 19
Myc
Frequency plot
PPtRb
PPt
Alteration type:
Loss
Neutral
Gain
-1.5
-0.1 0.1
1.5
F
p53;Pten;Rb
Myc
G
Ck8
CreER
1. Tamoxifen
R26:
CAG
Stop
Cas9
IRES
GFP
CK8-CreER;LSL-Cas9
2. EPO
CMV
SB
TR
EF1a
Myc
ITR
U6
sgp53
H
DAPI
GFP
CK8
merge
I
MP
CK8-MP
GFP
GFP
J
Myc
Ki67
WT1
panCk
K
NES
5 10
MYC targets V1
E2F targets
G2M checkpoint
Oxidative Phosphorylation
MYC targets V2
mTORC1 signaling
DNA repair
Glycolysis
Fatty acid metabolism
Spermatogenesis
Unfolded protein response
Adipogenesis
Peroxisome
Pancreas beta cells
UV response up
MP
MP-CK8
NES
-8 -6 -4
Interferon gamma respose
Allograft rejection
TNFa signaling via NFKB
Inflammatory response
Interferon alpha response
IL6 JAK STAT3 signaling
IL2 STAT5 sigaling
KRAS signaling up
Apical junction
UV response down
EMT
Complement
Coagulation
Apoptosis
Myogenesis
MP
MP-CK8

Figure 2.1: EPO-GEMM approach generates high-grade serous ovarian cancer that is of epithelial origin.

(A-B) Representative immunohistochemical staining of a *Trp53;Pten;Rb* EPO-GEMM ovarian tumor **(A)** and a corresponding micrometastasis in the omentum **(B)** for the HGSOC markers CK7, WT1, Pax8 and Ki67. Scale bar 20 µm. **(C)** Sanger sequencing confirming editing of the respective gene loci targeted by the indicated CRISPR-Cas9-sgRNAs in a *Trp53;Pten;Rb* EPO-GEMM ovarian tumor compared to an unmodified wild-type (WT) tissue. **(D)** Clonality analysis of two representative paired primary tumors (OV) and omentum metastasis (Met). Percentage of reads of the dominant clones was derived by deep sequencing of the *Trp53* amplicon. **(E)** Frequency plot of CNA analysis of *Trp53;Pten;Rb* (PPtRb, n=3) and *Trp53;Pten* (PPt, n=2) EPO-GEMM ovarian tumors. **(F)** Representative immunohistochemical staining of a *Trp53;Pten;Rb* EPO-GEMM ovarian tumor for MYC. Scale bar 20 µm. **(G)** Schematic of the EPO-GEMM approach *in CK8-CreER;LSL-Cas9-IRES-GFP* mice. Tamoxifen is given to excise the Stop-cassette to drive Cas9 expression in Ck8-positive cells. A *MYC* transposon vector, a transposon vector harboring a sgRNA targeting *Trp53* (sg*p53*), and a Sleeping Beauty transposase (SB) are delivered into the ovary of *CK8-CreER-Cas9* mice by direct *in vivo* electroporation. **(H)** Representative immunofluorescence staining of the oviduct of a *CK8-CreER;LSL-Cas9-IRES-GFP* mouse one week after Tamoxifen treatment. **(I)** Macroscopic GFP expression in MP tumors generated by *in vivo* tissue electroporation of a WT mouse (left) or a *CK8-CreER;LSL-Cas9-IRES-GFP* mouse (right). **(J)** Representative immunohistochemical staining of MP EPO-GEMM ovarian tumors generated in *CK8-CreER;LSL-Cas9-IRES-GFP* mice. Scale bar 20 µm. **(K)** Comparison of top enriched (left, red) and depleted (right, blue) Hallmark genesets derived from RNA-seq data in MP and CK8-MP EPO-GEMM tumors compared to normal tissue. Star indicates p-value < 0.05.

HR-DEFICIENT TUMORS HAVE UNIQUE GENOMIC, IMMUNE, AND THERAPY RESPONSE FEATURES

More than one third of ovarian cancer patients are classified as HR-deficient (Cancer Genome Atlas Research Network 2011). To model tumors arising in this large fraction of patients, we incorporated sgRNAs targeting *Brca1* into the MP combination described above using a vector that co-expresses *Trp53* and *Brca1* sgRNAs (*MYC;p53;Brca1*, MPB1) (**Fig. 3.1A**). Tumors arising in these animals displayed an onset and histology that was similar to those harboring *MYC* and *Trp53* alterations alone (**Fig. 3.1B-C**). Despite the similar latency, tumors produced with the plasmid cocktail that included the *Brca1* sgRNA invariably displayed indels at the *Brca1* sgRNA target site (**Fig. 3.1D**), implying that *Brca1* inactivation produced a selective advantage during tumorigenesis. Accordingly, as is characteristic of HR-deficient cells (Hill et al. 2018), MPB1 tumor cells isolated from EPO-GEMM tumors (but not MP controls) showed reduced induction of Rad51-containing nuclear foci following irradiation compared to MP tumor cells with intact *Brca1* (**Fig. 3A**).

Compared to HR-proficient tumors, HR-deficient human ovarian cancers acquire even more genomic rearrangements (Y. K. Wang et al. 2017), display substantial T cell infiltration (Strickland et al. 2016; Wieser et al. 2018; Ovarian Tumor Tissue Analysis (OTTA) Consortium et al. 2017), and are more responsive to platinum-based chemotherapy (Naumann et al. 2018; Bolton et al. 2012). Similarly, murine MPB1 ovarian EPO-GEMM tumors harbored more copy number alterations (**Fig.**

3B) and a greater proportion of $CD4^+$ and $CD8^+$ T-cells expressing both activation and exhaustion markers relative to *Brca1*-proficient counterparts (**Fig. 3C-D**, **Fig. 3.1E**). Furthermore, mice harboring primary MPB1 tumors showed significantly improved survival following cisplatin therapy (**Fig. 3E**), a result that was recapitulated in mice harboring tumors derived following subcutaneous or intraperitoneal (ip) injection of primary EPO-GEMM tumor-derived cell lines (**Fig. 3.1F-H**). Therefore, *Brca1*-deficient EPO-GEMM tumors recapitulate key biological and clinical features of human HR-deficient tumors.

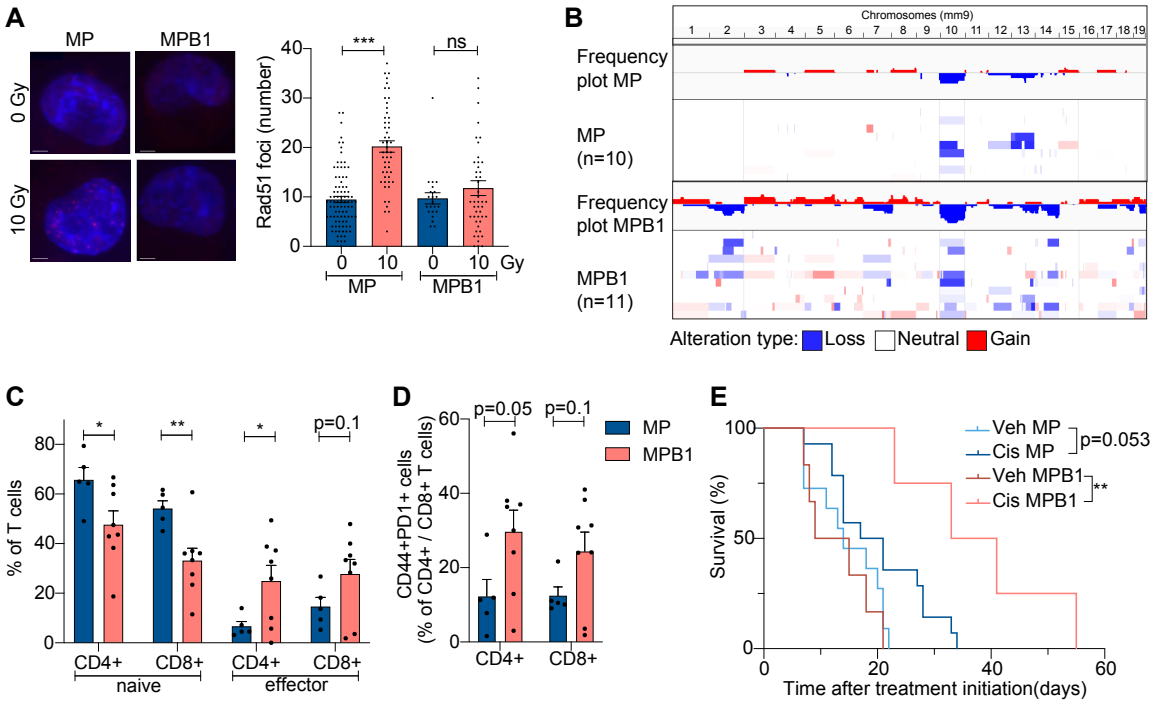
A
MP
MPB1
0 Gy
10 Gy
Rad51 foci (number)
***
ns
0
10
0
10
Gy
MP
MPB1
B
Chromosomes (mm9)
Frequency plot MP
MP (n=10)
Frequency plot MPB1
MPB1 (n=11)
Alteration type: Loss Neutral Gain
C
% of T cells
*
**
*
p=0.1
CD4+
CD8+
CD4+
CD8+
naive
effector
D
CD44+PD1+ cells (% of CD4+ / CD8+ T cells)
p=0.05
p=0.1
MP
MPB1
CD4+
CD8+
E
Survival (%)
Veh MP
Cis MP
Veh MPB1
Cis MPB1
p=0.053
**
Time after treatment initiation(days)

Figure 3. HR-deficient tumors have unique genomic, immune, and therapy response features.

(A) Representative images showing immunofluorescence staining of RAD51 (left) and the quantification of the number of RAD51 foci per nuclei (right). Cell nuclei were stained with DAPI (blue). Scale bar 5 μm. **(B)** Frequency plot of CNV analysis of MP (n = 10) and MPB1 (n = 11) EPO-GEMM ovarian tumors. **(C-D)** Immune cell analysis subtyping by flow cytometric analysis of representative EPO-GEMM tumors of the indicated genotypes (n = 5-8 mice per group). **(E)** Kaplan-Meier survival curve of C57BL/6 mice electroporated with the indicated combinations of plasmids and treated with vehicle (veh) or cisplatin (cis). Treatment was initiated after tumors were palpable (n = 4-13 mice per group). *$p \leq 0.05$, **$p \leq 0.01$, ***$p \leq 0.001$; Mean ± SEM; Analyses performed using unpaired t test (A, C-D) and log-rank test (E).

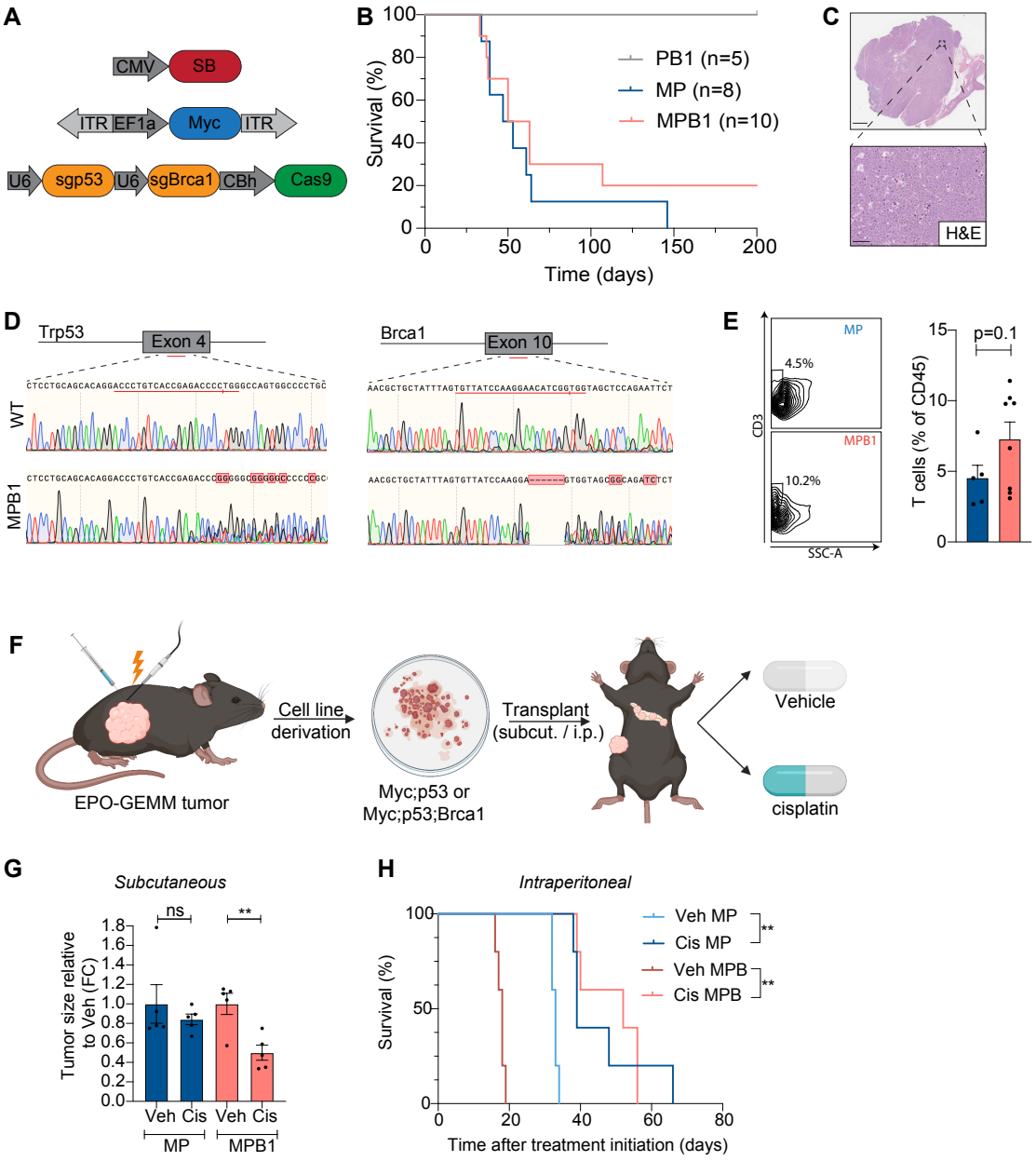
A
CMV
SB
ITR
EF1a
Myc
ITR
U6
sgp53
U6
sgBrca1
CBh
Cas9
B
Survival (%)
Time (days)
PB1 (n=5)
MP (n=8)
MPB1 (n=10)
C
H&E
D
Trp53
Exon 4
Brca1
Exon 10
WT
MPB1
E
MP
MPB1
4.5%
10.2%
CD3
SSC-A
T cells (% of CD45)
p=0.1
F
EPO-GEMM tumor
Cell line derivation
Myc;p53 or Myc;p53;Brca1
Transplant (subcut. / i.p.)
Vehicle
cisplatin
G
Subcutaneous
Tumor size relative to Veh (FC)
ns
**
Veh Cis Veh Cis
MP
MPB1
H
Intraperitoneal
Survival (%)
Time after treatment initiation (days)
Veh MP
Cis MP
Veh MPB
Cis MPB
**
**

Figure 3.1: HR deficiency drives tumors with increased T-cell infiltration and improved therapy response.

(A) Plasmid combination used to induce HR-deficient EPO-GEMM tumors. **(B)** Kaplan-Meier survival curve of C57BL/6 mice electroporated with the indicated combinations of plasmids. **(C)** Representative H&E staining of a MPB1 EPO-GEMM tumor. Scale bar 5000 µm (top), 100 µm (bottom). **(D)** Sanger sequencing confirming editing of the *Trp*53 and *Brca1* gene loci targeted by the indicated CRISPR-Cas9 sgRNAs in a MPB1 EPO-GEMM ovarian tumor. **(E)** Analysis of the T cell infiltrate of representative EPO-GEMM tumors of the indicated genotypes by flow cytometry (n=5-8 mice per group). **(F)** Schematic of transplantation approach of EPO-GEMM derived cell lines. **(G)** Relative tumor size of subcutaneously transplanted MP or MPB1 tumor cell lines treated with vehicle or cisplatin (n=5 mice per group). **(H)** Kaplan-Meier survival curve of mice after ip transplantation of MP or MPB1 tumor cell lines and treatment with vehicle or cisplatin (n=5 mice per group). Mice were randomized according to luciferase signal before treatment initiation.

*p ≤ 0.05, **p ≤ 0.01, ***p ≤ 0.001, ns: not significant; Mean ± SEM; Analyses performed using unpaired t test (E, G) and log-rank test (H).

CISPLATIN TREATMENT PREFERENTIALLY INDUCES TUMOR CELL SENESCENCE AND ALTERS IMMUNE INFILTRATES IN HR-DEFICIENT HGSOC

As a first step towards assessing mechanisms leading to genotypic differences in intrinsic cisplatin sensitivity, we analyzed the biological responses to cisplatin treatment *in vitro* and *in vivo*. Cultured cells established from MP and MPB1 tumors showed similar levels of growth inhibition and apoptosis induction following cisplatin treatment *in vitro* (**Fig. 4.1A-B**) and *in vivo* (**Fig. 4.1C**). In contrast, *Brca1*-deficient cells showed a much greater proclivity for senescence, displaying an increase in senescence-associated β-galactosidase (SA-β-gal) activity and a decrease in colony forming potential following cisplatin treatment compared to the *Brca1*-proficient MP counterparts (**Fig. 4.1D-E**). Similar results were observed *in vivo*, with MPB1-derived tumors showing more SA-ß-gal activity as measured by the fluorogenic substrate C12RG (Debacq-Chainiaux et al. 2009), reduced phosphorylated Rb, and a concomitant decrease in Ki67 staining compared to MP controls after short-term cisplatin treatment (**Fig. 4A**). Apparently, *Brca1* mutations sensitize ovarian tumor cells to cisplatin-induced senescence.

Senescence is a potent tumor suppressive mechanism that involves a stable proliferative arrest coupled to a secretory program known as the senescence-associated secretory phenotype (SASP) (Sharpless and Sherr 2015). The SASP alters the tumor microenvironment, where it can modulate ECM, tumor vasculature, and the functionality of immune cells (Krizhanovsky et al. 2008; Kang

et al. 2011) that, in some instances, produces an inflammatory tumor microenvironment (Ruscetti et al. 2018; Ruscetti et al. 2020). To assess the presence and nature of SASP in our system, we performed cytokine array analysis on a series of cisplatin-treated MP and MPB1 cell lines. Out of the 44 factors assessed in this panel, *Ccl5*, *Cxcl10* and *Il6* were the most significantly increased in the *Brca1*-deficient cells (**Fig. 4B**) and this difference could also be confirmed on mRNA expression levels in several MPB1 cell lines (**Fig. 4.1F**) as well as in an isogenic setting in which *Brca1* was disrupted in MP tumor cells following *in vitro* establishment (**Fig. 4.1G**). Similar cytokine induction was observed upon taxol treatment, implying the effects were not unique to cisplatin (**Fig. 4.1H**). Interestingly, the number of SASP factors detected in MPB1 cells following chemotherapy treatment appears much more restricted than those observed in other contexts (Ruscetti et al. 2018; Ruscetti et al. 2020), showing predominant secretion of immune modulatory cytokines and no endothelial cell regulatory factors. Accordingly, we did not detect obvious changes in tumor vasculature as assessed by CD31 immunofluorescence following cisplatin treatment (**Fig. 4.1I**).

We also examined cisplatin responses in human cancer cells and patients. We analyzed the *BRCA1*-mutant UWB1.289 cell line along with its isogenic counterpart with forced expression of the *BRCA1* wild-type gene (DelloRusso et al. 2007). Cisplatin treatment led to induction of *CCL-5* and *CXCL-10* in the *BRCA1*-mutant cells, which was dampened by forced expression of *BRCA1*-WT (**Fig. 4C**). The *BRCA1*-mutant cells showed a more pronounced senescence

response, as evaluated by increased SA-β-gal activity and a decreased colony forming potential following cisplatin treatment **(Fig. 4D-E**). Additionally, a well-characterized *BRCA1*-deficient breast cancer cell line (Elstrodt et al. 2006) was also more prone to cisplatin-induced senescence than a *BRCA1*-proficient counterpart (**Fig. 4.1J-K**). In patients, a retrospective analysis of RNA-seq data from matched pre- and post-treatment samples (Jiménez-Sanchez et al. 2020) showed an enrichment for gene signatures linked to senescence and SASP post therapy (**Fig. 4.1L**) with *CCL-5* and *IL-6* being among the most enriched genes in these signatures. Furthermore, in a dataset where outcomes are known (Ahmed et al. 2007; Ingemarsdotter et al. 2015) (GSE15622), expression of senescence signatures was higher in the sensitive tumors (**Fig. 4F**). We also observed higher expression of the cytosolic DNA sensing pathway in sensitive tumors, which has previously been associated with senescence (Dou et al. 2017). While this dataset did not allow for classification of patients based on BRCA or HR status, it is consistent with the notion that senescence induction improves outcomes in HGSOC patients. Together, our data suggest that loss of *Brca1* in ovarian cancer cells is sufficient to predispose these cells to induction of a chemotherapy-induced senescence program characterized by cell cycle arrest and a defined secretory program, both of which are associated with improved outcomes in patients.

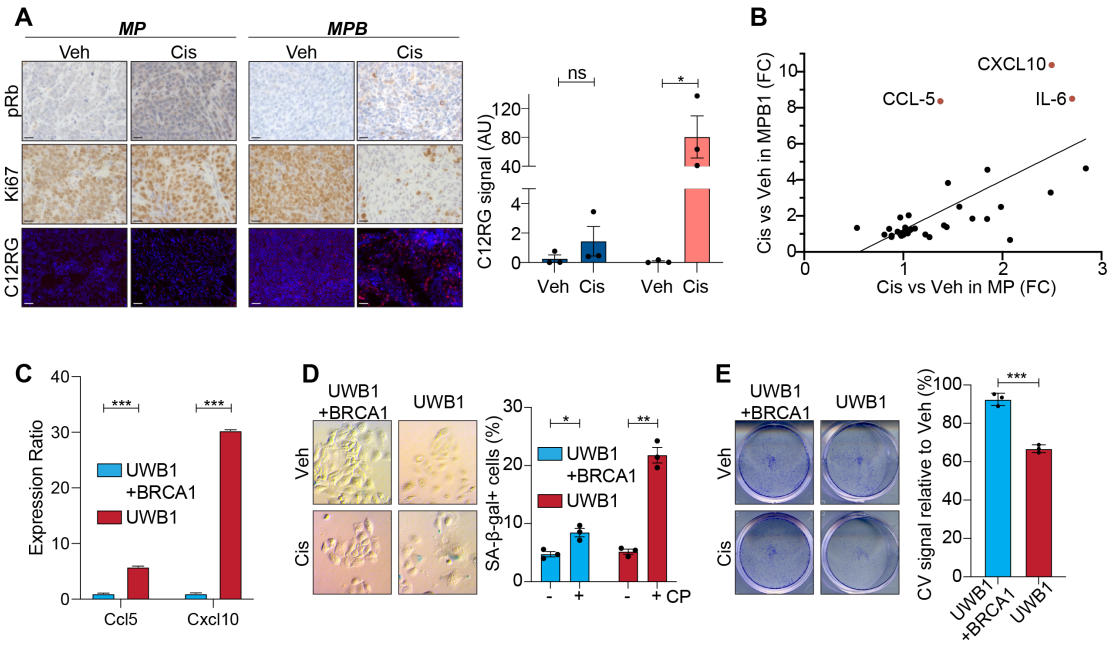
A
MP
MPB
Veh
Cis
pRb
Ki67
C12RG
C12RG signal (AU)
ns
*
B
Cis vs Veh in MPB1 (FC)
Cis vs Veh in MP (FC)
CXCL10
CCL-5
IL-6
C
Expression Ratio
UWB1 +BRCA1
UWB1
Ccl5
Cxcl10
D
SA-β-gal+ cells (%)
+ CP
E
CV signal relative to Veh (%)
F
Cell Cycle (KEGG)
Senescence (Tasdemir et al.)
SASP (Ruscetti et al.)
Cytosolic DNA sensing (KEGG)
Score
Pre-treat
Resistant
Sensitive

Figure 4. Cisplatin treatment preferentially induces tumor cell senescence and alters immune infiltrates in HR-deficient HGSOC.
(A) Immunohistochemical staining of phospho-Rb (pRb) and Ki67 and staining of C12RG, a fluorogenic substrate for SA-ß-gal activity, of subcutaneously transplanted tumors treated with vehicle or cisplatin. Scale bar 20 µm. Quantification of SA-ß-gal activity is shown on the right (n = 3). **(B)** Cytokine expression in MP (x-axis) or MPB1 (y-axis) cell lines treated with cisplatin relative to vehicle (n = 2 independent cell lines per genotype). **(C)** RT-qPCR analysis of *Ccl5* and *Cxcl10* in cisplatin-treated *BRCA1*-proficient (UWB1+BRCA1) or -deficient (UWB1) human ovarian cancer cells (n = 3). **(D)** SA-ß-gal staining (left) and quantification (right) of either *BRCA1*-proficient (UWB1+BRCA1) or -deficient (UWB1) human ovarian cancer cell lines after treatment with vehicle or 100 nM cisplatin for 6 days (n = 3). **(E)** Clonogenic crystal violet (CV) assay of human ovarian cancer cells replated in the absence of drugs after 6-day pretreatment as in (D) (n = 3). **(F)** Expression of senescence and SASP signatures in patient samples isolated pre-treatment and after 3 cycles of chemotherapy during the CTCR-OV01 clinical trial (Ahmed et al. 2007; Ingemarsdotter et al. 2015) (GSE15622). Post-treatment samples are sub-divided into resistant and sensitive cases. *p ≤ 0.05, **p ≤ 0.01, ***p ≤ 0.001; Mean ± SEM; Analyses performed using unpaired t-test (A, C-E) and Wilcoxon signed-rank test (F).

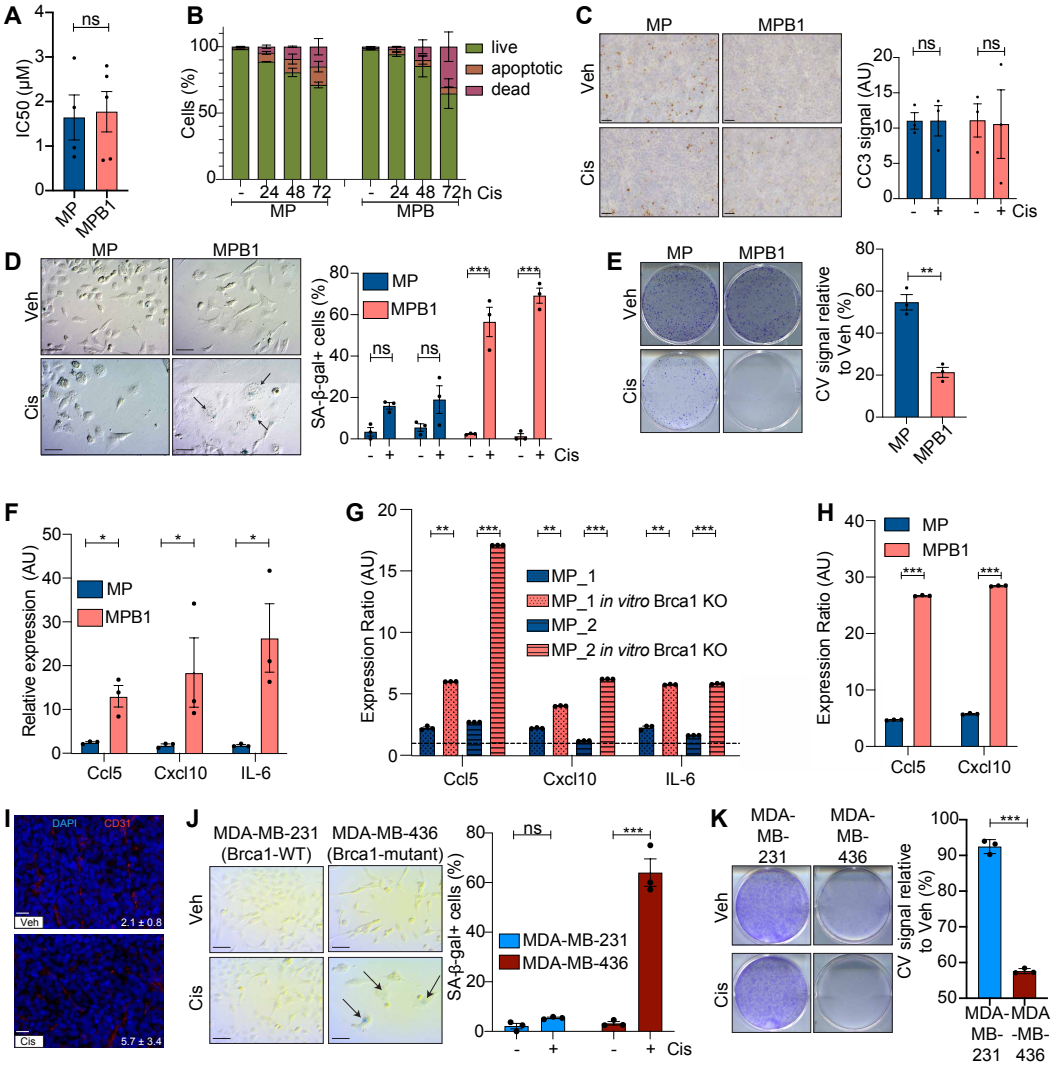
A
IC50 (μM)
ns
MP
MPB1
B
Cells (%)
live
apoptotic
dead
- 24 48 72 - 24 48 72h Cis
MP
MPB
C
MP
MPB1
Veh
Cis
CC3 signal (AU)
ns
ns
- + - + Cis
D
MP
MPB1
Veh
Cis
SA-β-gal+ cells (%)
MP
MPB1
ns
ns
***
***
- + - + - + - + Cis
E
MP
MPB1
Veh
Cis
CV signal relative to Veh (%)
**
MP
MPB1
F
Relative expression (AU)
MP
MPB1
*
*
*
Ccl5
Cxcl10
IL-6
G
Expression Ratio (AU)
MP_1
MP_1 in vitro Brca1 KO
MP_2
MP_2 in vitro Brca1 KO
**
***
Ccl5
Cxcl10
IL-6
H
Expression Ratio (AU)
MP
MPB1
***
***
Ccl5
Cxcl10
I
DAPI
CD31
Veh
2.1 ± 0.8
Cis
5.7 ± 3.4
J
MDA-MB-231 (Brca1-WT)
MDA-MB-436 (Brca1-mutant)
Veh
Cis
SA-β-gal+ cells (%)
ns
***
MDA-MB-231
MDA-MB-436
- + - + Cis
K
MDA-MB-231
MDA-MB-436
Veh
Cis
CV signal relative to Veh (%)
***
MDA-MB-231
MDA-MB-436
L
Rb targets senescent (Chicas et al.)
NES = 4.32
FDR q = 0.000
TNFa signaling via NFkB (Hallmark)
NES = 6.04
FDR q = 0.000
Regulation of cytokine production (GO)
NES = 4.64
FDR q = 0.000
Protein secretion (Hallmark)
NES = 4.32
FDR q = 0.000

Figure 4.1: Chemotherapy treatment induces senescence and SASP in HR-deficient HGSOC.

(A) IC50 values of MP or MPB1 cell lines treated with cisplatin. Cell viability was calculated relative to vehicle-treated control cells, measured with CellTiter-Glo assay 72h after treatment (n = 4-5). **(B)** Quantification of live (Annexin-V^-, PI^-), apoptotic (Annexin-V^+, PI^-) or dead (Annexin-V^+, PI^+) cells in MP or MPB1 cell lines after 24, 48 or 72 h of cisplatin treatment (n = 3). **(C)** Representative immunohistochemical staining and quantification of cleaved caspase-3 (CC3) signal in subcutaneously transplanted MP or MPB1 ovarian tumors after two cycles of cisplatin treatment (n = 3). Scale bar 40 µm. **(D)** SA-ß-gal staining of cell lines treated with vehicle or 1 µM cisplatin for 6 days (n = 2 independent cell lines per genotype with n = 3 technical replicates). Scale bar 50 µm. **(E)** Clonogenic crystal violet (CV) assay of MP or MPB1 cells replated in the absence of drugs after 6-day pretreatment as in (D) (n = 3 independent cell lines per genotype). **(F)** RT-qPCR analysis of *Ccl5*, *Cxcl10* and *Il6* in MP or MPB1 cell lines. Expression ratio of cisplatin-treated relative to untreated is shown. Each point represents a cell line derived from a different mouse tumor (n = 3). **(G)** RT-qPCR analysis of *Ccl5*, *Cxcl10* and *Il6* in MP cell lines transfected with control or *Brca1*-targeting sgRNA. Expression ratio of cisplatin-treated relative to untreated is shown. The different patterns represent a cell line derived from a different MP mouse tumor, in which *Brca1* was knocked-out after cell line establishment (n = 3 technical replicates per independent line). **(H)** RT-qPCR analysis of *Ccl5* and *Cxcl10* in MP or MPB1 cell lines treated with 50 nM Taxol. Expression ratio of treated relative to untreated is shown (n = 3). **(I)** IF staining and quantification of $CD31^+$ blood vessels of transplanted tumors after two cycles of cisplatin treatment (n = 3). Scale bar 20 µm. **(J)** SA-ß-gal staining (left) and quantification (right) of either *BRCA1* wild-type (WT) (MDA-MB-231) or -mutant (MDA-MB-436) human breast cancer cell lines after treatment with vehicle or cisplatin for 6 days (n = 3). Scale bar 50 µm. **(K)** Clonogenic crystal violet (CV) assay of human BRCA-WT or -mutant breast cancer cells replated in the absence of drugs after 6-day pretreatment as in (J) (n = 3). **(L)** Gene set enrichment analysis (GSEA) comparing expression of senescence and SASP signatures in patients after and before chemotherapy treatment in a human ovarian cancer dataset (Jiménez-Sanchez et al. 2020).

*p ≤ 0.05, **p ≤ 0.01, ***p ≤ 0.001, ns: not significant; Mean ± SEM; Analyses performed using unpaired t-test (A, C, E-K), one-way ANOVA (D) and Wilcoxon signed-rank test (L).

CISPLATIN TREATMENT LEADS TO A CGAS/STING-DEPENDENT INFILTRATION OF T- AND NK CELLS IN HR-DEFICIENT TUMORS.

Ccl5, *Cxcl10* and Il6 are immune modulatory cytokines and members of the Interferon Stimulated Genes (ISG) family that act downstream of cGAS/STING signaling (Li and Chen 2018) and are often associated with the SASP (Glück et al. 2017; H. Yang et al. 2017). cGAS is an intracellular innate immune sensor of cytosolic double-stranded DNA (Wu and Chen 2014) that can be activated by nucleic acids present in micronuclei and can increase in cells with rampant genome instability (Mackenzie et al. 2017). Breast and ovarian cancers harboring BRCA mutations have been shown to harbor high levels of micronuclei and cGas/STING activity (Parkes et al. 2017; Heijink et al. 2019). In agreement, cultured MPB1 tumor cells displayed a trend towards more micronuclei than MP tumor cells, a difference that was exacerbated following cisplatin treatment (**Fig. 5A**). A similar increase was seen in DNA damage as evaluated by yH2AX staining (**Fig. 5B**). These effects correlated with a genotype specific difference in immune infiltrates of transplanted tumors following cisplatin therapy. Specifically, MPB1 tumors showed a substantial increase in T and NK cells (**Fig. 5C-D**), and a marked reduction of M2-like macrophages (**Fig. 5.1A-C**), compared to MP controls.

To test whether the cGas/STING pathway contributed to the observed genotype-specific effects on drug responses, we generated two independent shRNAs capable of suppressing cGas expression (**Fig. 5.1D**), transduced these into MPB1 tumor cells, and examined their impact on senescence and tumor phenotypes

following cisplatin treatment. While cGAS suppression did not prevent drug-induced proliferative arrest or the appearance of senescence markers (**Fig. 5.1E-G**), it substantially reduced *Ccl5* and *Cxcl10* expression (**Fig. 5E, 5.1H**). *In vivo*, cGas/STING suppression blunted the therapy-induced accumulation of T- and NK cells in transplanted MPB1 tumors (**Fig. 5F-G**), while having no effect on myeloid cell infiltration (**Fig. 5.1I-K).** These data are consistent with a model whereby preferential induction of cisplatin-induced senescence in *Brca1*-deficient tumor cells contributes to cGas/STING activation and the establishment of a pro-inflammatory tumor microenvironment.

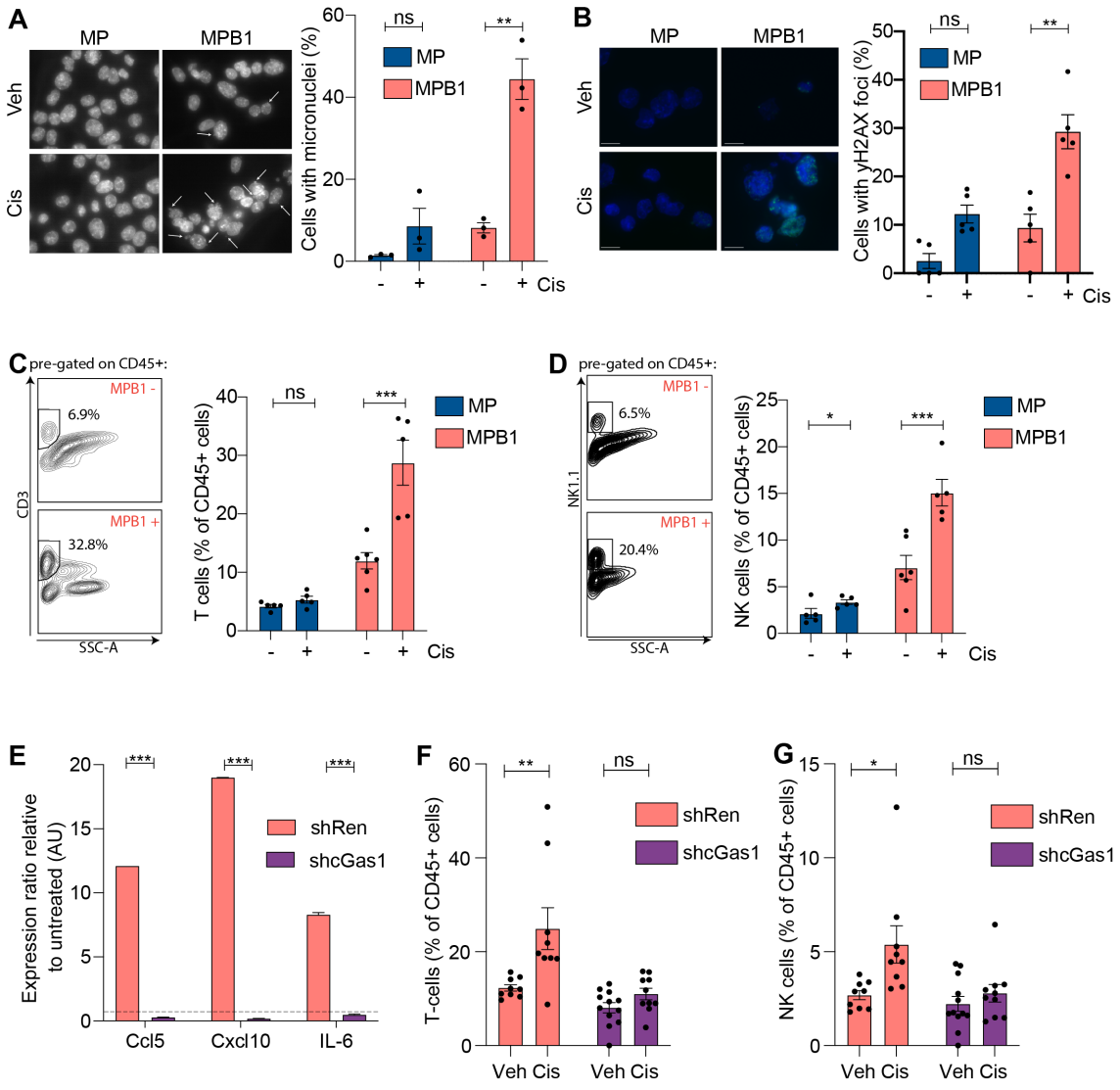
A
MP
MPB1
Veh
Cis
Cells with micronuclei (%)
ns
**
MP
MPB1
- + - + Cis
B
MP
MPB1
Veh
Cis
Cells with γH2AX foci (%)
ns
**
MP
MPB1
- + - + Cis
C
pre-gated on CD45+:
MPB1 -
6.9%
MPB1 +
32.8%
CD3
SSC-A
T cells (% of CD45+ cells)
ns
***
MP
MPB1
- + - + Cis
D
pre-gated on CD45+:
MPB1 -
6.5%
MPB1 +
20.4%
NK1.1
SSC-A
NK cells (% of CD45+ cells)
*
***
MP
MPB1
- + - + Cis
E
Expression ratio relative to untreated (AU)
***
***
***
shRen
shcGas1
Ccl5
Cxcl10
IL-6
F
T-cells (% of CD45+ cells)
**
ns
shRen
shcGas1
Veh Cis Veh Cis
G
NK cells (% of CD45+ cells)
*
ns
shRen
shcGas1
Veh Cis Veh Cis

Figure 5. Cisplatin treatment leads to a cGas/STING-dependent infiltration of T- and NK cells in HR-deficient tumors.

(A) Micronuclei staining of MP or MPB1 cell lines treated with cisplatin. Cell nuclei were stained with DAPI (grey) (n = 3 independent cell lines per genotype). **(B)** yH2AX staining (green) of MP or MPB1 cell lines treated with cisplatin. Cell nuclei were stained with DAPI (blue) (n = 5). **(C-D)** Representative flow cytometry plots (left) and quantification (right) of T-cell **(C)** or NK-cell **(D)** infiltration in subcutaneously transplanted ovarian tumors after treatment with 2 cycles of cisplatin (n = 5-6 mice per group). **(E)** RT-qPCR analysis of *Ccl5*, *Cxcl10* and *Il6* in cell lines containing control Renilla (shRen) or cGas shRNAs (shcGas). Expression ratio of cisplatin-treated relative to vehicle-treated is shown (n = 3). **(F-G)** Flow cytometry analysis of T- **(F)** and NK cell **(G)** infiltration in subcutaneously transplanted MPB1 ovarian tumors containing control Renilla or cGas shRNAs after treatment with 2 cycles of cisplatin (n=8-12 mice per group). *p ≤ 0.05, **p ≤ 0.01, ***p ≤ 0.001; Mean ± SEM; Analyses performed using unpaired t-test (A-G).

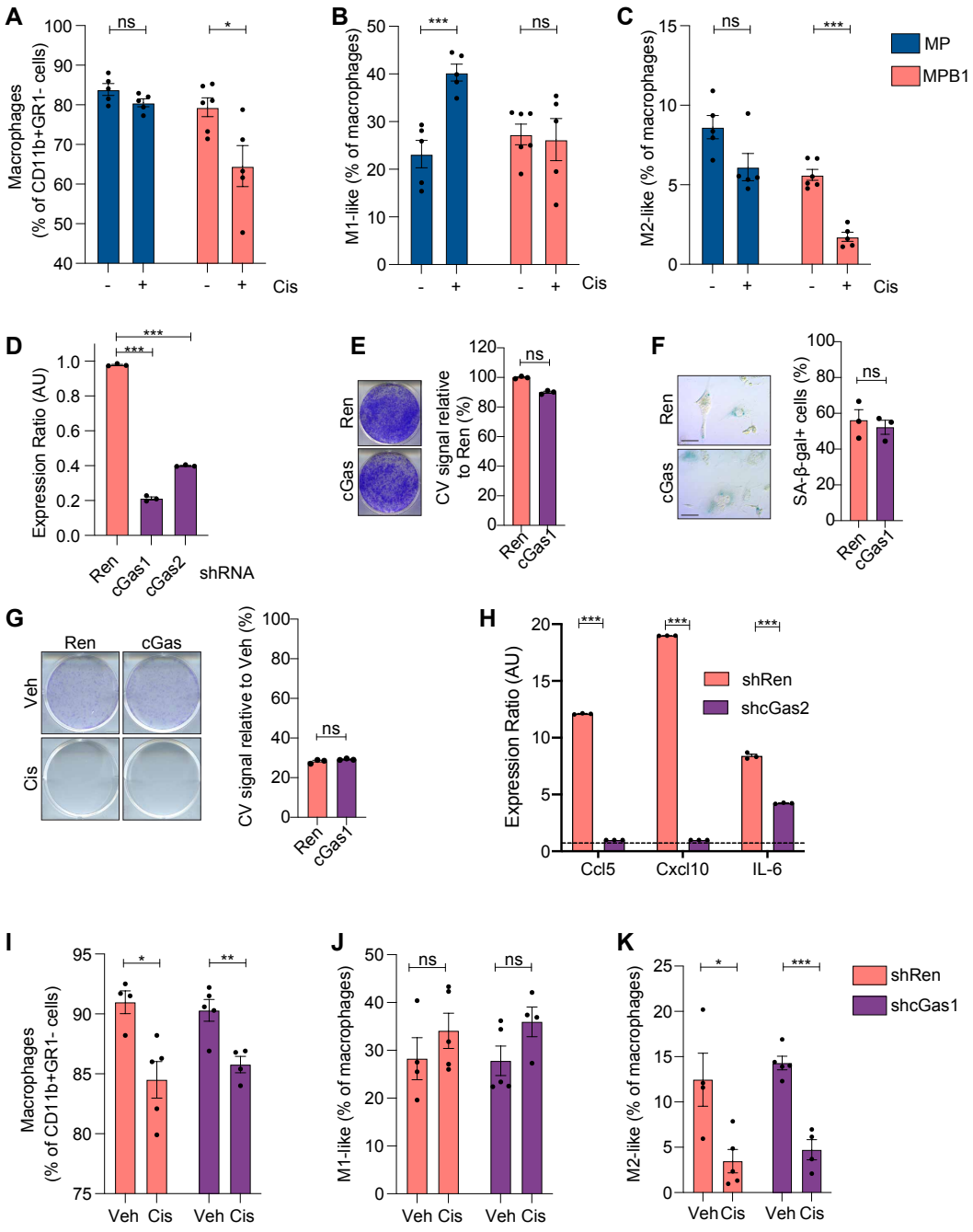
A
Macrophages (% of CD11b+GR1- cells)
ns
*
Cis
B
M1-like (% of macrophages)
***
ns
C
M2-like (% of macrophages)
MP
MPB1
D
Expression Ratio (AU)
Ren
cGas1
cGas2
shRNA
E
Ren
cGas
CV signal relative to Ren (%)
F
SA-β-gal+ cells (%)
G
Veh
Cis
CV signal relative to Veh (%)
H
Expression Ratio (AU)
shRen
shcGas2
Ccl5
Cxcl10
IL-6
I
Veh
J
K
shcGas1

Figure 5.1: cGas knockdown does not alter the myeloid immune compartment or cell-intrinsic senescence response.

(A-C) Infiltration of macrophages (**A**) and percentages of M1-like (CD206-, CD80+) (**B**) and M2-like (CD206+, CD80-) (**C**) macrophages in subcutaneously transplanted MP or MPB1 ovarian tumors after treatment with 2 cycles of cisplatin (n = 5-6 mice per group). **(D)** RT-qPCR analysis of cGas in MPB1 cell lines containing control Renilla (shRen) or cGas shRNAs (shcGas) shRNAs targeting (n = 3). **(E)** Clonogenic assay of MPB1 cell lines containing control Renilla (shRen) or cGas (shcGas) shRNAs (n = 3). **(F)** SA-ß-gal staining of MPB1 cell lines containing control Renilla (shRen) or cGas (shcGas) shRNAs after treatment with vehicle or cisplatin for 6 days (n = 3). Scale bar 20 μm. **(G)** Clonogenic crystal violet (CV) assay of MP or MPB1 cells replated in the absence of drugs after 6-day pretreatment as in (F) (n = 3). (**H**) RT-qPCR analysis of *Ccl5*, *Cxcl10* and *Il6* in MPB1 cell lines containing control Renilla (shRen) or cGas (shcGas) shRNAs. Expression ratio of cisplatin-treated relative to untreated is shown (n = 3). (**I-K**) Infiltration of macrophages (**I**) and percentages of M1 (**J**) and M2 (**K**) macrophages in transplanted shRen or shcGas MPB1 ovarian tumors after treatment with 2 cycles of cisplatin (n = 4-5 mice per group).

*p ≤ 0.05, **p ≤ 0.01, ***p ≤ 0.001, ns: not significant; Mean ± SEM; Analyses performed using unpaired t-test (A-C, E-K) or one-way ANOVA (D).

BRCA1 LOSS SENSITIZES TUMORS TO CHEMO AND ICB COMBINATION THERAPY

Tumors displaying an inflamed microenvironment often upregulate molecules that blunt anti-tumor immunity, a phenomenon that can also occur following cisplatin treatment (Fournel et al. 2019; Tran et al. 2017). Accordingly, cisplatin treatment induced cell surface expression of the immune checkpoint molecule PD-L1 in MBP1 (but not MP) tumor cells (**Fig. 6.1A-B**). In patients and in a range of preclinical models, such a scenario often predicts increased tumor sensitivity to ICB (Herbst et al. 2014). To test this in our system, treatment outcomes were examined in MP or MPB1 EPO-GEMMs or mice harboring syngeneic subcutaneous or ip tumors generated by transplantation of explanted cells. Of note, the ip context mimics the clinically relevant context of disseminated disease after surgical resection of the primary tumor.

In line with recent findings showing HGSOC patients receive little, if any, clinical benefit from ICB monotherapy (Liu et al. 2020), neither MP nor MPB1 tumors showed appreciable responses to anti-PD-1 therapy. In contrast, MPB1 tumors responded more effectively to cisplatin and anti-PD-1 combination therapy compared to MP tumors in all three tumor settings (**Fig. 6A-B**, **6.1C-F**). This increased responsiveness was associated with an increase in the number of tumor-infiltrating $CD8^+$ T-cells that expressed the activation marker Granzyme B (**Fig. 6C**). Interestingly, cGas suppression in *Brca1*-deficient tumors curtailed the responsiveness to combination therapy, but not single chemotherapy treatment,

resulting in reduced clearance of senescent cells after combination therapy (**Fig. 6D-E**). These data demonstrate that chemo- and immunotherapy uniquely synergize in *Brca1*-deficient tumors, whereas cGas/STING activation plays an important role in immune cell recruitment and clearance of senescent cells but is not necessarily required for primary chemotherapy response.

While many ovarian cancer patients initially respond to treatment, most patients eventually develop resistance. To study the process of disease relapse in previously responding tumors, we generated a cell line from a *Brca1*-mutant EPO-GEMM tumor that progressed following treatment with cisplatin and anti-PD-1 antibody and tested responsiveness to cisplatin therapy *in vitro* and to cisplatin and anti-PD-1 combination therapy *in vivo* following subcutaneous injection into syngeneic recipients. Interestingly, tumors formed by these cells did not respond to the combination of cisplatin and ICB *in vivo* (**Fig. 6F**), an effect that correlated with a reduced propensity to undergo senescence (**Fig. 6G**) and induce SASP (**Fig. 6H**). While loss of 53BP1 can restore error-free DNA repair in *Brca1*-mutant cells (Bunting et al. 2010), this mechanism is not responsible for the observed therapy resistance in our system, as 53BP1 foci could be still detected upon cisplatin treatment (**Fig. 6.1G**). Together, these data underscore the role of therapy-induced senescence as a crucial mediator of response and resistance to platinum-based chemotherapy in HR-deficient ovarian cancer and its ability to sensitize these tumors to ICB.

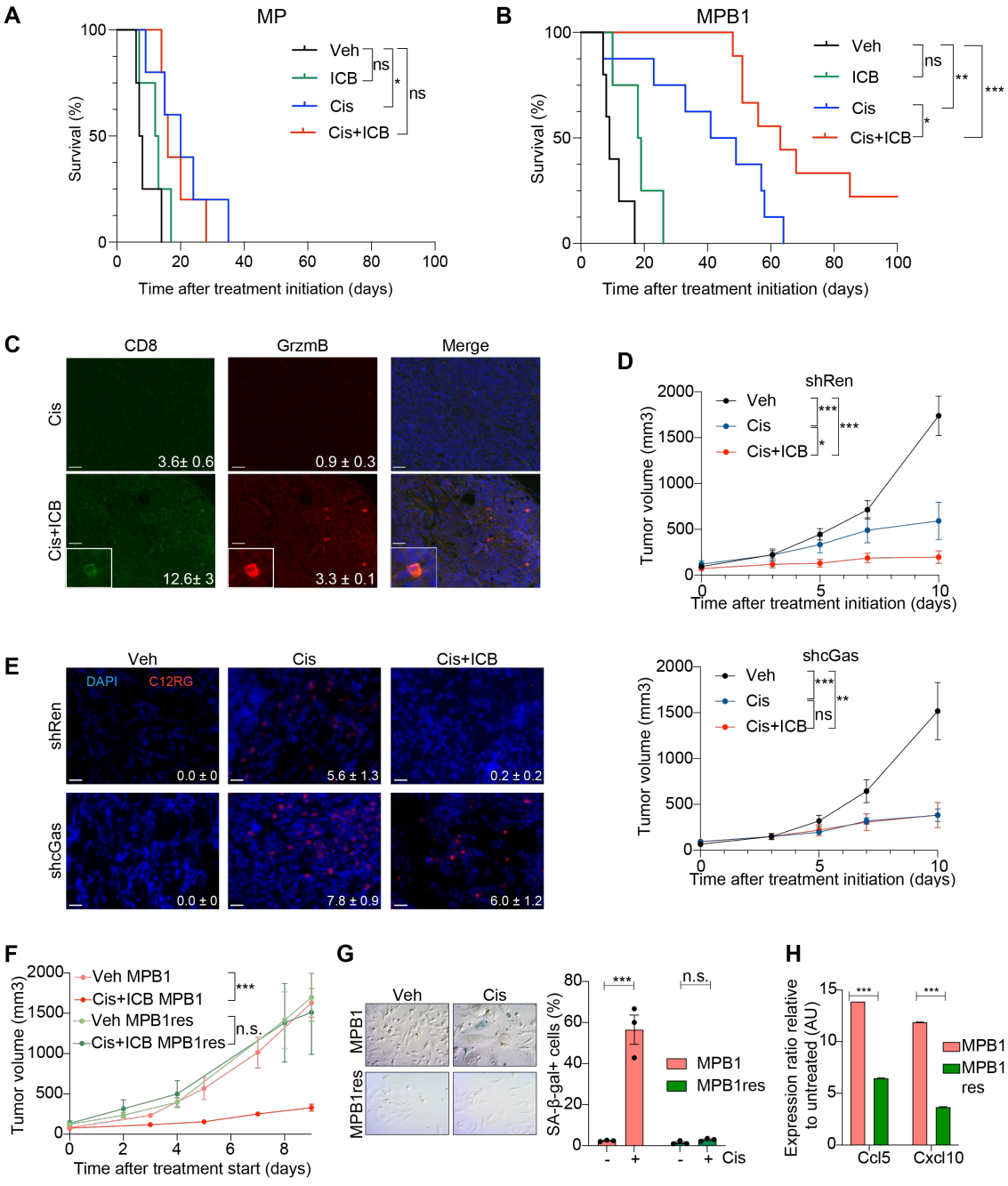
A
MP
Survival (%)
Time after treatment initiation (days)
Veh
ICB
Cis
Cis+ICB
ns
*
ns
B
MPB1
Survival (%)
Time after treatment initiation (days)
Veh
ICB
Cis
Cis+ICB
ns
**
***
*
C
CD8
GrzmB
Merge
Cis
Cis+ICB
3.6± 0.6
0.9 ± 0.3
12.6± 3
3.3 ± 0.1
D
shRen
Tumor volume (mm3)
Time after treatment initiation (days)
Veh
Cis
Cis+ICB
***
*
***
shcGas
Tumor volume (mm3)
Time after treatment initiation (days)
Veh
Cis
Cis+ICB
***
ns
**
E
Veh
Cis
Cis+ICB
DAPI
C12RG
shRen
shcGas
0.0 ± 0
5.6 ± 1.3
0.2 ± 0.2
0.0 ± 0
7.8 ± 0.9
6.0 ± 1.2
F
Tumor volume (mm3)
Time after treatment start (days)
Veh MPB1
Cis+ICB MPB1
Veh MPB1res
Cis+ICB MPB1res
***
n.s.
G
Veh
Cis
MPB1
MPB1res
SA-β-gal+ cells (%)
***
n.s.
MPB1
MPB1res
Cis
H
Expression ratio relative to untreated (AU)
***
***
MPB1
MPB1 res
Ccl5
Cxcl10

Figure 6. *Brca1* loss sensitizes tumors to chemo and ICB combination therapy.

(A+B) Kaplan-Meier survival curve of MP **(A)** or MPB1 **(B)** EPO-GEMM mice treated with the indicated drugs. Treatment was initiated after tumors were detected by abdominal palpation (n = 4-9 mice per group). **(C)** Representative IF staining and quantification (mean number of cells per field ± SEM, $p \leq 0.05$) of subcutaneously transplanted MPB1 ovarian tumors treated with indicated treatments (n = 5 fields for two independent tumors). Scale bar 20 μm. **(D)** Tumor growth over time of transplanted MPB1 cell lines containing control Renilla (shRen, top) or cGas shRNAs (shcGas, bottom) with vehicle, cisplatin or cisplatin + ICB (n = 5-6 mice per group). **(E)** Staining and quantification of C12RG, a fluorogenic substrate for SA-ß-gal activity, in tumors treated as in (D) (n = 3). Scale bar 20 μm. **(F)** Tumor growth of transplanted MPB1 or resistant MPB1 (MPB1_res) cell lines treated with vehicle or cisplatin + ICB (n = 5-6 mice per group). **(G)** SA-ß-gal staining (left) and quantification (right) of MPB1 or MPB1_res cell lines treated with vehicle or cisplatin for 6 days. (n = 3). **(H)** RT-qPCR analysis of *Ccl5* and *Cxcl10* in MPB1 or MPB1_res cell lines (n = 3). Expression ratio of cisplatin-treated relative to vehicle-treated is shown. $^{*}p \leq 0.05$, $^{**}p \leq 0.01$, $^{***}p \leq 0.001$; Mean ± SEM; Analyses performed using log-rank test (A, B), unpaired t-test (C, E-H) and one-way ANOVA (D).

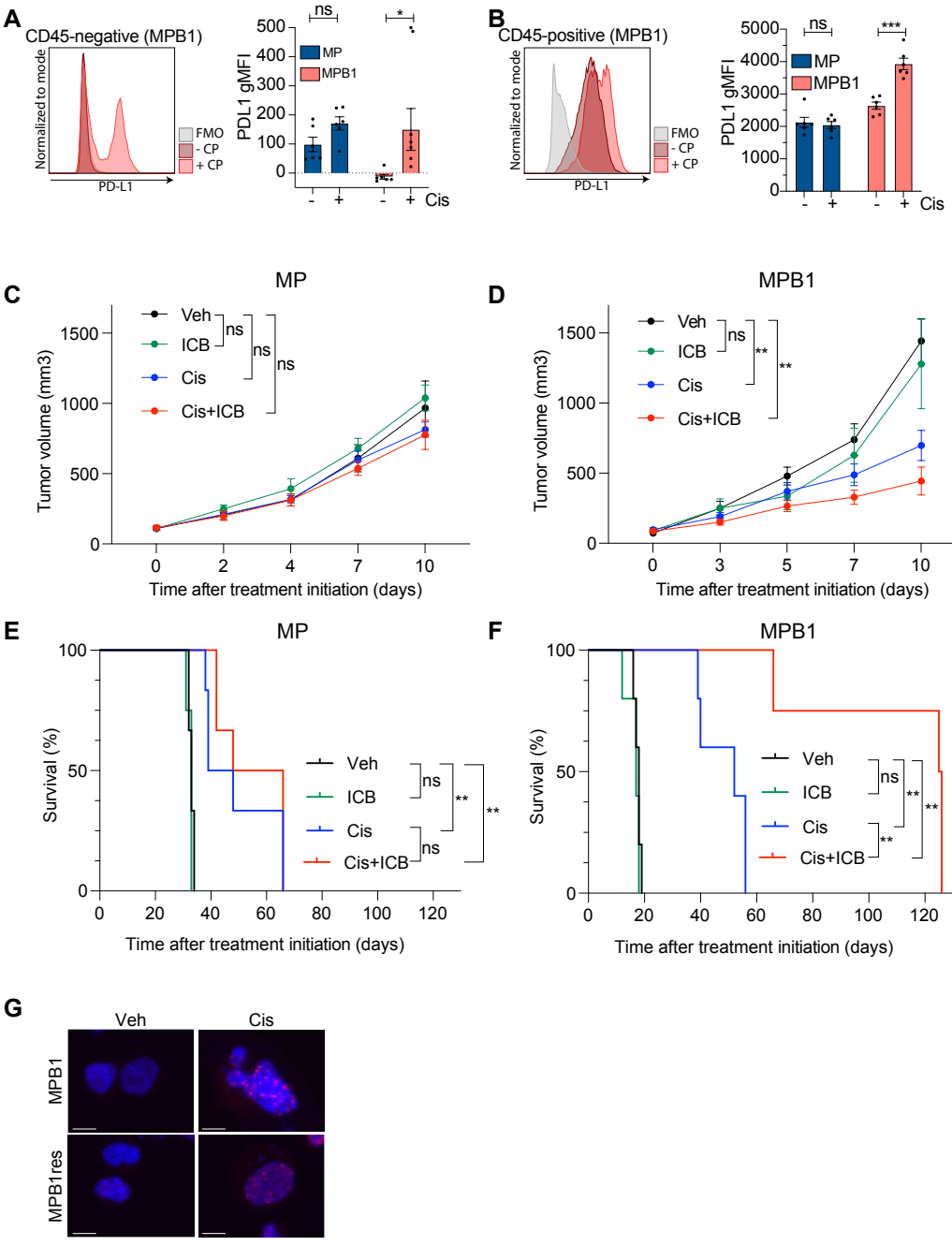
A
CD45-negative (MPB1)
Normalized to mode
PD-L1
FMO
- CP
+ CP
PDL1 gMFI
MP
MPB1
ns
*
Cis
B
CD45-positive (MPB1)
***
C
MP
Tumor volume (mm3)
Veh
ICB
Cis
Cis+ICB
Time after treatment initiation (days)
D
MPB1
E
Survival (%)
F
G
Veh
Cis
MPB1
MPB1res

Figure 6.1: Treatment response of HR-proficient and -deficient HGSOC after treatment with chemotherapy and ICB.

(A+B) Representative MFI plot (left) and quantification (right) of PD-L1 expression on tumor cells (CD45-negative) **(A)** or immune cells (CD45-positive) **(B)** from subcutaneously transplanted MPB1 ovarian tumors treated with vehicle or cisplatin (n = 5-6 mice per group). **(C+D)** Tumor growth of subcutaneously transplanted MP **(C)** or MPB1 **(D)** tumors treated with vehicle, ICB, cisplatin or cisplatin + ICB (n = 5 mice per group). **(E+F)** Kaplan-Meier survival curve of MP **(E)** or MPB1 **(F)** tumors generated by ip injection (n = 4-6 mice per group). Mice were randomized according to luciferase signal before treatment initiation. **(G)** Immunofluorescence staining of 53BP1 foci in MP and MPB1 cell lines treated with vehicle or cisplatin for 72h. Scale bar 10 µm.

*p ≤ 0.05, **p ≤ 0.01, ***p ≤ 0.001, ns: not significant; Mean ± SEM; Analyses performed using unpaired t-test (A-B), one-way ANOVA (C-D) and log-rank test (E-F).

DISCUSSION

HGSOC is a genetically unique tumor type that almost uniformly develops resistance to conventional, targeted, and immune therapies. In this study, we produced a flexible non-germline-based mouse model that recapitulates the genetic, histological, and molecular features of human HGSOC. We illustrate its use for studying genetic interactions during tumorigenesis and exploring molecular mechanisms that dictate treatment response. Our results add to previous work showing that HR defects can produce distinct tumor phenotypes and vulnerabilities (Farmer et al. 2005; Chapman and Verma 1996), and link a chemotherapy-induced senescence program to therapeutic outcome (**Fig. 7**).

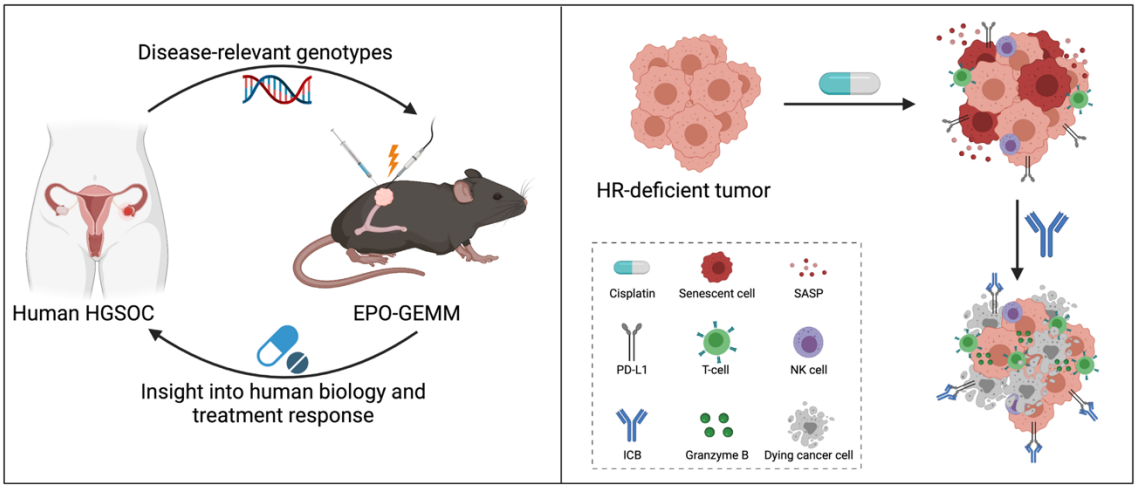

Figure 7: EPO-GEMMs recapitulate genetic features of human HGSOC and provide insights into human biology and treatment response

Until recently, the study of HGSOC has been limited by the paucity of model systems that reflect hallmark genetic or physiological features of the human disease. We believe that the EPO-GEMM platform will revolutionize preclinical HGSOC research. While traditional germline models offer similar capabilities to the EPO-GEMM models described herein, they are simply too time consuming and asynchronous to be a workhorse system. By contrast, the EPO-GEMM approach enables the production of autochthonous tumors in immunocompetent mice that naturally disseminate, enabling the relatively synchronous production of cohorts of tumor-bearing mice simply from a set of plasmids and readily available immunocompetent wild-type mice. While the use of lineage-specific Cas9 or CRE transgenes can be used to control the cell of origin, electroporation of the ovary and fallopian tube of wild-type mice produces epithelial tumors that resemble human HGSOC, similar to what was observed in cell line studies (Orsulic et al. 2002). As such, the approach can be applied to any strain of recipient mice, making it straightforward to study how host factors influence tumor trajectories.

The cell of origin of HGSOC remains controversial. The EPO-GEMM approach offers an opportunity to compare the role of different cell of origins in a living animal. While our study demonstrated that the tumors likely originate from the Cytokeratin-8 positive epithelial compartment, one could imagine similar studies to delineate the role of the OSE compared to the FTE. These results might enable the choice of optimal treatment strategies, as the cell of origin has been described to impact response patterns to cytotoxic drugs (Shuang Zhang et al. 2019).

Our study is complementary to a recent report that also used tissue electroporation to generate immune competent ovarian cancer models (Teng et al. 2021). While the methods used in both settings are conceptually similar, they differ in the choice of oncogenic lesions, latency, and spontaneous metastatic spread in wild-type hosts. Furthermore, we implement transgene vectors for oncogene expression, confirm the epithelial origin of the resulting tumors and the human relevance of the disease. By incorporating *MYC* overexpression and *Brca1* disruption into the platform, we substantially accelerate tumor onset and enable modeling of clinically important HR-deficient tumors. Collectively, these approaches provide a powerful orthogonal system to ovarian cancer models produced from tumor-derived cell or organoid lines (Lõhmussaar et al. 2020; Shuang Zhang et al. 2020; Iyer et al. 2020; Walton et al. 2016; Kopper et al. 2019; Hill et al. 2018; Maru et al. 2019; Xing and Orsulic 2006). Other recent reports to model prostate (Leibold et al. 2020; Choi et al. 2018) and pancreatic cancer (Maresch et al. 2016; J.-S. Park et al. 2014) using tissue electroporation support the broad utility of the approach. In theory, the approach is expandable to any organ of interest that is amenable to a survival surgery. Choosing which genetic alterations to model should be informed by human genomic sequencing data to ensure that the models are relevant to study the human disease.

Our results implicate a cellular senescence program as an important component of response and resistance in HGSOC. Previous work suggests that senescence-inducing therapeutics can stimulate a SASP-dependent remodeling of the tumor

microenvironment that, in some instances, leads to senescent cell clearance or sensitizes tumor cells to immune recognition following checkpoint blockade (Ruscetti et al. 2018; Ruscetti et al. 2020). By contrast, in other settings, treatment-associated SASP programs can stimulate tumor relapse and dissemination (Demaria et al. 2017). Herein, we show that the ability of cisplatin to induce senescence in ovarian cancer cells depends on tumor genotype, being substantially more pronounced following treatment of *Brca1*-deficient (compared to *Brca1*-proficient) ovarian tumors. The genotype-specific induction of senescence has been observed previously: For example, by screening of panel of cancer cell lines that carry different cancer-relevant mutations, it was demonstrated that senescence phenotypes can be induced in a context-dependent manner that varies among different genetic backgrounds (Cairney et al. 2017). In our context one could hypothesize that the increased genomic instability caused by the mutation of Brca1 leads in turn to an increase in micronuclei and a cGas-Sting mediated SASP. The SASP alters immune cell infiltrates and sensitizes the Brca1-deficient tumors to ICB. Consistent with the importance of the senescence program in therapy response, senescence signatures can be detected in post treatment samples from HGSOC patients. Moreover, tumors derived from a *Brca1*-deficient cancer that progressed on treatment lost their ability to induce senescence and SASP upon cisplatin treatment, leading to resistance to cisplatin in combination with ICB.

Interestingly, the increased propensity of *Brca1*-deficient tumors to undergo senescence and/or activate the cGas/STING pathway appears to extend to other agents beyond cisplatin treatment. In our experiments, similar observations were made after treating ovarian cancer cell lines with taxol. *Brca1*-deficient models of breast and ovarian cancer treated with PARP inhibitors show similar behaviors (Ding et al. 2018; Grabosch et al. 2019; Pantelidou et al. 2019; Bruand et al. 2021; Fleury et al. 2019). As such, senescence induction may underlie the improved response of HR-deficient tumors to genome destabilizing therapies in the clinic.

In contrast to other settings of therapy-induced senescence examined to date (Glück et al. 2017; Dou et al. 2017; H. Yang et al. 2017), the SASP program triggered by cisplatin therapy in *Brca1*-deficient ovarian tumors was limited to *Ccl5*, *Cxcl10*, and *Il6* of the factors examined. It has been previously observed that the outcomes of senescence-inducing therapies are context-dependent, complex, and often unpredictable. The unpredictability is accounted to the effect of the SASP that is highly dependent on cell type, context and differs between different stages of tumor progression (Faget, Ren, and Stewart 2019; Coppé et al. 2010; Jochems et al. 2021). How *Brca1* deficiency results in the secretion of the defined set of SASP factors remains to be further studied, but it is likely that the increased genomic instability and micronuclei formation play a driving force. These are then sensed by the cGas/STING machinery. cGas suppression efficiently suppressed SASP induction and sensitization to ICB following cisplatin treatment yet had no effect on treatment outcomes following cisplatin monotherapy. This implies that

SASP is sufficient to sensitize tumor cells to ICB and, in agreement, injection of SASP activated tumor cells sensitizes an immunologically cold murine ovarian models to ICB (X. Hao et al. 2021) whereas CCL5 suppression in another model attenuates T-cell inflammation (Bruand et al. 2021). While it remains possible that senescence and cGas/STING-dependent cytokine induction are parallel processes, they imply that potent anti-tumor responses require both cell-intrinsic senescence induction and TME modulation. Deeper analysis of senescence biomarkers in the context of cGas deficiency could help to delineate whether senescence and cGas/STING-dependent cytokine induction are parallel or linear processes.

Although HR deficiency can increase tumor immunogenicity (Dai et al. 2018), *BRCA1/2* mutations have no effect on the response to ICB monotherapy in HGSOC patients (Liu et al. 2020; Disis et al. 2016; Matulonis et al. 2019). Our model recapitulates these findings: *Brca1*-deficient tumors display an increase in immune infiltration pre-treatment yet are non-responsive to ICB. Our results imply that frontline chemotherapy or PARP inhibitors should sensitize HR-deficient tumors to checkpoint blockade, yet clinical trials to date suggest that these mechanisms are not universally operative in patients (Moore et al. 2020; Pujade-Lauraine et al. 2021; Konstantinopoulos et al. 2015; Ledermann et al. 2020). Instead, these trials identify tumor positivity for PD-L1 and CD8 expression – features of the *Brca1*-deficient tumors studied herein – as biomarkers of a combinatorial response (Färkkilä et al. 2020). It seems likely that the disparate

outcomes between the human and animal studies reflect the longer course of tumor evolution in patients, which may inactivate components of the senescence machinery. Accordingly, we see that *Brca1*-deficient tumor cells that acquire senescence defects are non-responsive to the chemotherapy/ICB combination. To better mimic the longer course tumor evolution that occurs in patients in a murine model system, approaches like serial transplantation of EPO-GEMM tumor cells could be used. Every passage into a new host with a competent immune system would require the tumor cells to find new ways to evade immunity.

In sum, future studies incorporating the flexible features of the EPO-GEMM approach will enable the further dissection of mechanisms that dictate ovarian cancer response and resistance and, more broadly, expediate investigation of other clinically relevant aspects of this disease.

APPENDIX

CHOLESTEROL METABOLISM AS A THERAPEUTIC VULNERABILITY IN PI3K HYPER-ACTIVATED HGSOC TUMORS

Here, I will briefly discuss the ongoing work evaluating therapeutic vulnerabilities in HGSOC tumors with hyper-activated PI3K signaling. As alterations of the PI3K/AKT pathway are common events in HGSOC and have been linked to poor prognosis (Network et al. 2017; Martins et al. 2014), we leveraged the flexibility of the EPO-GEMM approach to evaluate loss of the tumor suppressor Pten (**Fig. 8A**). This approach led to hyperactivation of the PI3K pathways in the resulting tumors, as measured by phosphorylated Akt (**Fig. 8B**). Mice carrying Myc;p53;Pten (MPPt) tumors had vastly accelerated onset of disease compared to MP tumors (**Fig. 8C**) and all MPPt mice presented with metastasis (**Fig. 8D**). We validated this phenotype in an isogenic system by transducing a Pten-WT EPO-GEMM derived cell line with an shRNA targeting Pten or Renilla as a control (**Fig. 8E-F**). While downregulation of Pten did not affect in vitro cell proliferation (**Fig. 8G**), the mice succumbed earlier to their disease if Pten was downregulated in the transplanted tumor cells (**Fig. 8H**). These results suggest that a hyperactivated PI3K pathway provides tumor cells with a survival advantage *in vivo*.

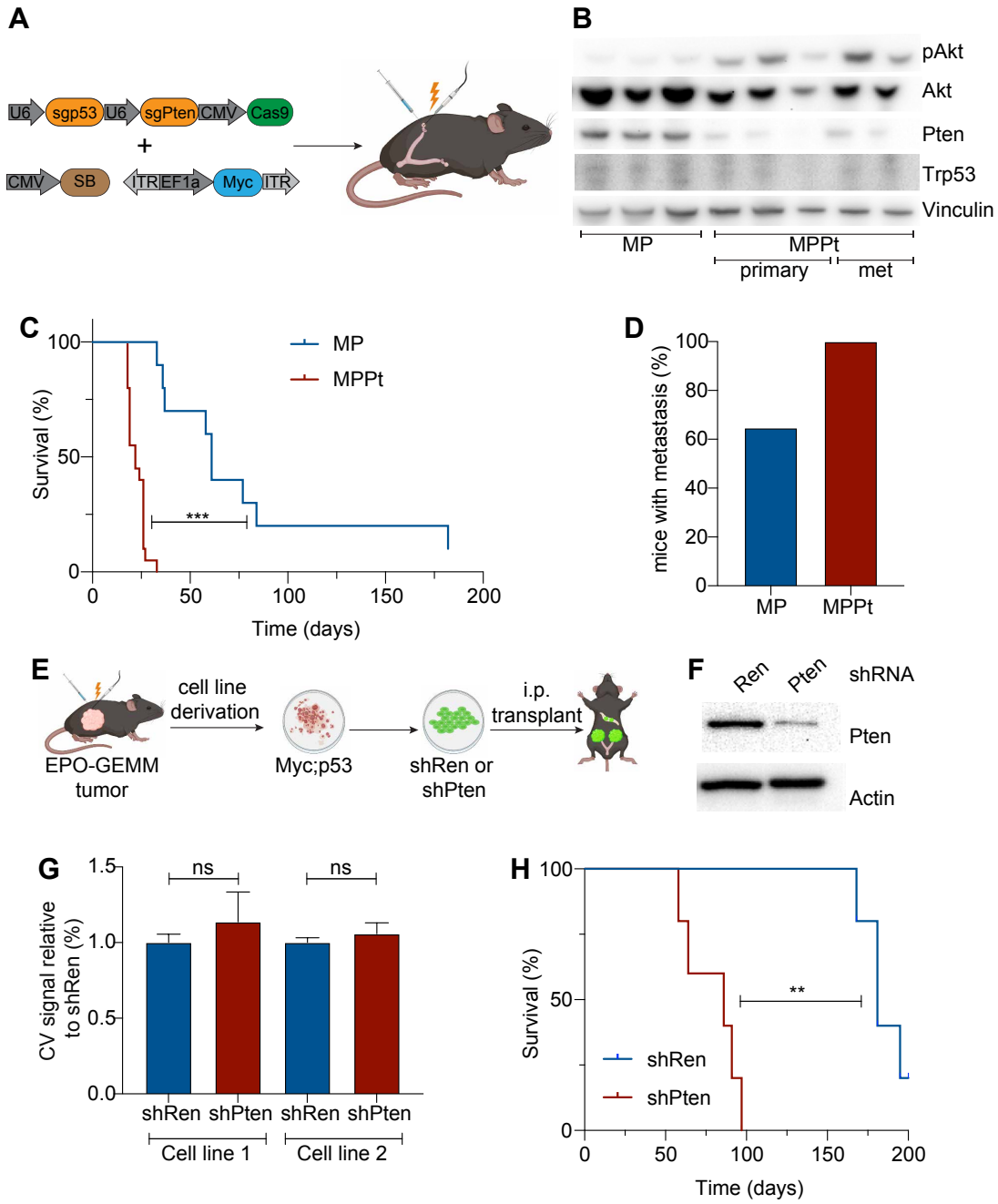
A
U6
sgp53
U6
sgPten
CMV
Cas9
+
CMV
SB
ITR
EF1a
Myc
ITR
B
pAkt
Akt
Pten
Trp53
Vinculin
MP
MPPt
primary
met
C
Survival (%)
MP
MPPt
***
Time (days)
D
mice with metastasis (%)
MP
MPPt
E
cell line derivation
EPO-GEMM tumor
Myc;p53
shRen or shPten
i.p. transplant
F
Ren
Pten
shRNA
Pten
Actin
G
CV signal relative to shRen (%)
ns
ns
shRen
shPten
shRen
shPten
Cell line 1
Cell line 2
H
Survival (%)
**
shRen
shPten
Time (days)

Figure 8. Pten loss in EPO-GEMM tumors accelerates onset and severity of disease

(A) Vector combination used to generate EPO-GEMM tumors with loss of Pten. **(B)** Western Blot analyzing members of the PI3K pathway in MP and MPPten tumors. **(C)** Kaplan-Meier survival curve of C57BL/6 mice electroporated with the indicated combinations of plasmid (n=10 for MP, n=20 for MPPt) **(D)** Percentage of mice presenting with metastasis at end-stage of disease (n=17 for MP, n=8 for MPPt) **(E)** Schematic of the system to evaluate loss of Pten in an isogenic system. **(F)** Western Blot evaluating knockdown of Pten in cell lines that were transduced with shRNAs targeting Renilla or Pten. **(G)** Clonogenic crystal violet (CV) assay of EPO-GEMM derived MP cell lines transduced with the indicated shRNA (n=3 technical replicates per independent cell line). **(H)** Kaplan-Meier survival curve of C57BL/6 mice transplanted with EPO-GEMM derived MP cell lines transduced with the indicated shRNA (n=5 per cell line).

To elucidate the mechanisms by which hyperactivation of the PI3K pathway drives disease aggressiveness, we performed RNA-seq on MP and MPPt EPO-GEMM tumors. In contrast to MP tumors, MPPt tumors showed transcriptional upregulation of the cholesterol biosynthesis pathway (**Fig. 9A**). Cholesterol metabolism has been previously described to contribute to cancer progression, including cell proliferation, migration and invasion (Huang, Song, and Xu 2020) and the cholesterol biosynthesis pathway can be activated by PI3K-AKT signaling (Mullen et al. 2016). To determine, if our results are relevant in human patients, we assessed the expression of the cholesterol biosynthesis pathway in TCGA HGSOC patients. Tumors with a PI3K or PTEN alteration showed higher expression of the cholesterol biosynthesis pathway than WT patients (**Fig. 9B**). In the EPO-GEMM model, up-regulation of the cholesterol biosynthesis pathway led to increased cholesterol production, as we observed more cholesterol in the ascites of mice with MP than MPPt tumors (**Fig. 9C**). Cholesterol has been previously described to dampen anti-tumor immunity by causing dysfunction of cytotoxic T-cells (Ma et al. 2019; S. Xu et al. 2021) and dendritic cells (F. Xu et al. 2021; Villablanca et al. 2009) in the tumor microenvironment. In the future, we plan to explore the effect of the increased cholesterol levels on the tumor microenvironment by performing flow cytometry and co-culture assays.

To assess the functional role of increased cholesterol biosynthesis in tumor cells, EPO-GEMM derived cell lines were grown in delipidated medium. While MP cell lines were unable to grow in medium that does not contain cholesterol and lipids, MPPt cell lines were able to expand (**Fig. 9D**). Genetic screening for factors that

prevent growth of MPPt cells in delipidated medium can provide mechanistic insights in the future.

Clinically, cholesterol levels can be lowered using statins, inhibitors of the rate-limiting enzyme of the cholesterol biosynthesis pathway HMG-CoA reductase (HMGCR). Statin use is associated with lower risk of PTEN-null, but not PTEN intact prostate cancer (Allott et al. 2020). However, statin treatment of mice carrying PTEN-mutant EPO-GEMM tumors did not prolong survival (**Fig. 9E**). While statin treatment reduced cholesterol level in the serum, it did not result in decreased cholesterol level in the ascites (**Fig. 9F**) indicating that the drug might not be delivered to the tumor cells effectively or that the tumor finds compensatory pathways to upregulate cholesterol production. To overcome drug delivery hurdles, we performed tumor-cell specific knockdown of *Hmgcr* in EPO-GEMM derived cell lines using 2 independent shRNAs (**Fig. 9G**), which significantly increased survival after re-transplantation of *Hgmcr* shRNA-carrying cell lines compared to control shRNAs.

Given the urgent need for better treatment options for HGSOC, we will keep exploring the role of cholesterol metabolism in genotype-specific ovarian cancer aggressiveness and different ways to target the pathway.

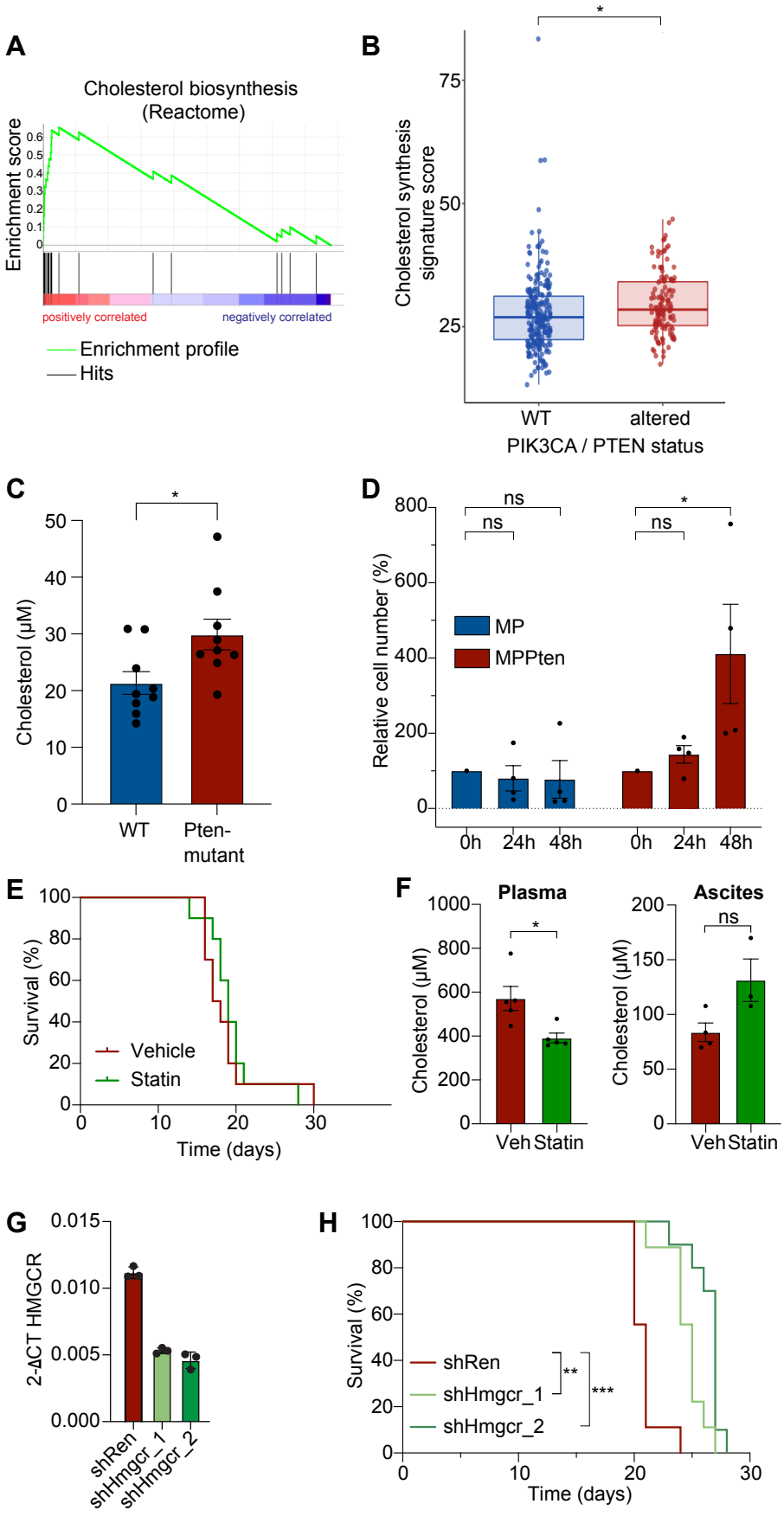
A
Cholesterol biosynthesis
(Reactome)
Enrichment score
positively correlated
negatively correlated
Enrichment profile
Hits
B
Cholesterol synthesis signature score
WT
altered
PIK3CA / PTEN status
C
Cholesterol (µM)
WT
Pten-mutant
D
Relative cell number (%)
MP
MPPten
0h
24h
48h
ns
E
Survival (%)
Vehicle
Statin
Time (days)
F
Plasma
Ascites
Cholesterol (µM)
Veh
Statin
G
2-ΔCT HMGCR
shRen
shHmgcr_1
shHmgcr_2
H
Survival (%)
shRen
shHmgcr_1
shHmgcr_2
Time (days)

Figure 9. Loss of Pten promotes upregulation of cholesterol biosynthesis. **(A)** GSEA of MPPt vs MP EPO-GEMM tumors reveals an enrichment for cholesterol biosynthesis in MPPt tumors. **(B)** Expression of cholesterol signature in patients with HGSOC with WT or altered PIK3CA or PTEN status from the TCGA dataset. **(C)** Measurement of free cholesterol in the ascites of EPO-GEMM bearing mice (n = 9-10 mice per group). **(D)** Growth of MP or MPPten EPO-GEMM derived cell lines in de-lipidated culture medium over 48 hours (n=4 independent cell lines per genotype). **(E)** Kaplan-Meier survival curve of C57BL/6 mice with MPPt EPO-GEMM tumors treated with either vehicle or Statin (n=10 mice per group). **(F)** Measurement of free cholesterol in the plasma (left) or ascites (right) of mice as in E (n=5 mice per group). **(G)** RT-qPCR analysis of *Hmgcr* expression in MPPt cell lines transduced with control *Renilla* (shRen) or 2 independent *Hmgcr* shRNAs (n = 3). **(H)** Kaplan-Meier survival curve of mice transplanted with MPPt cell lines containing Renilla or Hmgcr shRNAs (n=9-10 mice per group).

TREATMENT OF OVARIAN CANCER WITH CELLULAR IMMUNOTHERAPIES

Here, I will briefly discuss the ongoing efforts to evaluate the treatment of ovarian cancer with cellular immunotherapies. Being notoriously hard to treat, there is an urgent need to evaluate innovative treatment modalities for HGSOC. Chimeric antigen receptor (CAR) T cells have recently emerged as a potentially curative cancer treatment. CARs are synthetic receptors that redirect T cell effector potential, specificity and additional functions (Sadelain, Rivière, and Riddell 2017). CD19-directed CAR T cells have demonstrated remarkable efficacy for treatment of refractory B cell malignancies (J. H. Park et al. 2018). One hurdle for CAR T cell therapy is the identification of a target protein that is uniformly expressed on cancer but not normal tissue (Srivastava and Riddell 2018). Here, we explore the use of CAR T cells targeting urokinase plasminogen activator receptor (uPAR) for the treatment of ovarian cancer. uPAR is a multifunctional receptor that has previously been described to be involved in tumor cell processes, including metastasis (Blasi and Carmeliet 2002; Mazar 2008). It is widely expressed in ovarian carcinomas (Kenny et al. 2011; L. Wang et al. 2009) and correlates with a more aggressive phenotype (Borgfeldt et al. 2001). Previous approaches to target uPAR in ovarian cancer with either antisense (Kook et al. 1994) or cellular therapies (L. Wang et al. 2019) indicate that uPAR plays a functional role in ovarian cancer metastasis. Our lab has recently described uPAR-targeting CAR T for the elimination of senescent cells (Amor et al. 2020).

uPAR is highly expressed on EPO-GEMM derived ovarian cancer cell lines (**Fig. 10A**) and primary tumor tissue (**Fig. 10B**). We performed cytotoxicity assays by

co-culturing uPAR CAR T cells with EPO-GEMM derived ovarian cancer cell lines of the MP or MPB genotype. Well-characterized CAR T cells directed against CD19 were used as a negative control (Brentjens et al. 2003). uPAR but not CD19 targeting CAR T cells efficiently eliminated ovarian cancer cells of either genotype (**Fig. 10C**). To study whether uPAR CAR T cells can eliminate ovarian cancer cells in vivo, we intraperitoneally transplanted EPO-GEMM derived cell lines into WT C57BL/6 mice and after tumor establishment 1.5 million uPAR CAR T cells or untransduced (UT) T cells as controls were administered. As regional ip infusion of CAR T cells has shown superior protection against peritoneal tumors compared to systemically infused CAR T cells (Katz et al. 2019), we compared intravenous (iv) and ip application of uPAR CAR T cells. While iv infusion did not translate to a survival advantage, mice receiving uPAR CAR T cells ip lived significantly longer than those receiving UT CAR T cells (**Fig. 10D**). This result was repeated in a larger cohort of mice that were injected ip with either UT or uPAR CAR T cells (**Fig. 10E**). The treated mice remained highly active and did not display any toxicities as evaluated by changes in temperature or weight (**Fig. 10F**). A part of uPAR is proteolytically cleaved upon ligand binding, which generates soluble uPAR (suPAR) that can be detected in the blood. Mice receiving uPAR CAR T treatment showed reduced levels of suPAR in their blood (**Fig. 10G**) and end-stage tumors expressed lower levels of uPAR (**Fig. 10H**).

In the future, we plan to further characterize the response of ovarian cancer to uPAR CAR T cells and explore synergistic approaches with established chemotherapies.

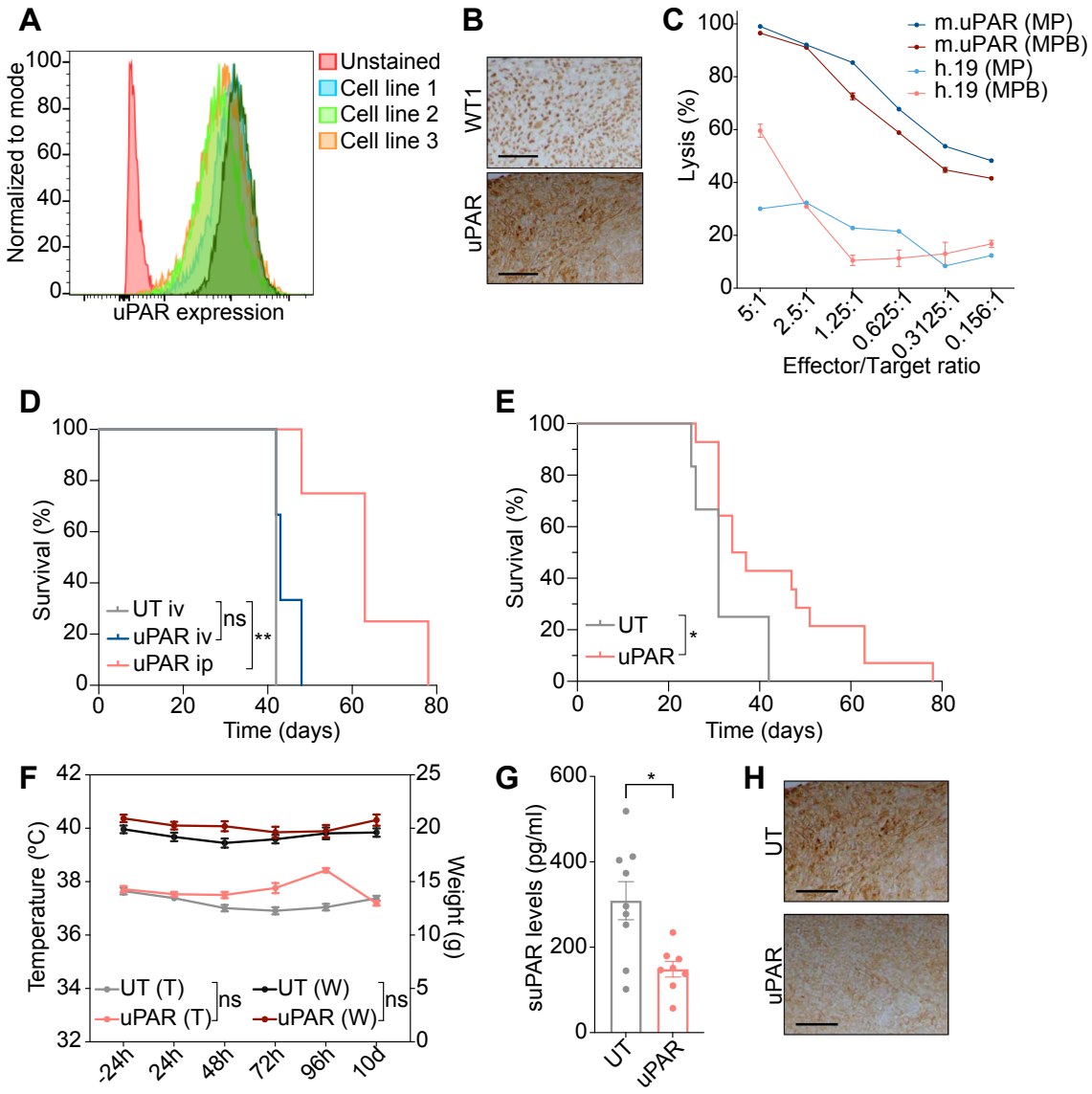
A
Normalized to mode
uPAR expression
Unstained
Cell line 1
Cell line 2
Cell line 3
B
WT1
uPAR
C
Lysis (%)
Effector/Target ratio
m.uPAR (MP)
m.uPAR (MPB)
h.19 (MP)
h.19 (MPB)
D
Survival (%)
Time (days)
UT iv
uPAR iv
uPAR ip
ns
**
E
Survival (%)
Time (days)
UT
uPAR
*
F
Temperature (°C)
Weight (g)
UT (T)
uPAR (T)
UT (W)
uPAR (W)
ns
ns
-24h
24h
48h
72h
96h
10d
G
suPAR levels (pg/ml)
*
UT
uPAR
H
UT
uPAR

Figure 10. Targeting of murine ovarian cancer with uPAR CAR-T cells.
(A) Representative MFI plot of uPAR expression on EPO-GEMM derived ovarian cancer cell lines. **(B)** Representative immunohistochemical staining of a *MPB* EPO-GEMM ovarian tumor for the HGSOC marker WT1 and murine uPAR. Scale bar 200 µm. **(C)** Cytotoxic T cell activity as determined by an 18-h bioluminescence assay using luciferase-expressing MP or MPB ovarian cancer cells as targets that were co-culture with CAR-T cells targeting murine uPAR (mUPAR) or human CD19 (h19) as a control. Experiment was performed in triplicates. **(D)** Kaplan-Meier survival curve of C57BL/6 mice transplanted with a MPB cell line and treated with untransduced (UT) or uPAR CAR-T cells. CAR-T cell injection was performed 7 days after tumor cell transplantation and either intraveneously (iv) or intraperitoneally (ip) (n=3-4 mice per group). **(E)** Kaplan-Meier survival curve of C57BL/6 mice transplanted with a MPB cell line and treated with untransduced (UT) or uPAR CAR-T cells. CAR-T cell injection was performed ip 7 days after tumor cell transplantation (n=12-14 mice per group). **(F)** Temperature (T) and weight (W) measured 24 h before and at different time points after CAR T cell infusion. P values (ns, not significant) refer to the comparison between untransduced (UT) and mouse uPAR (uPAR) CAR-T injected mice at 10 d (n=10 mice per group). **(G)** Soluble uPAR (suPAR) in the blood of mice treated as in (E). Blood was taken 16 days after CAR-T cell injection (n=8-9 mice per group). **(H)** Representative immunohistochemical uPAR staining of tumor sections treated as in (E). Scale bar 200 µm.

BIBLIOGRAPHY

Ahmed, A. A., Etemadmoghadam, D., Temple, J., Lynch, A. G., Riad, M., Sharma, R., et al. (2010). Driver mutations in TP53 are ubiquitous in high grade serous carcinoma of the ovary. *The Journal of Pathology*, *221*(1), 49–56. http://doi.org/10.1002/path.2696

Ahmed, A. A., Mills, A. D., Ibrahim, A. E. K., Temple, J., Blenkiron, C., Vias, M., et al. (2007). The extracellular matrix protein TGFBI induces microtubule stabilization and sensitizes ovarian cancers to paclitaxel. *Cancer Cell*, *12*(6), 514–527. http://doi.org/10.1016/j.ccr.2007.11.014

Allott, E. H., Ebot, E. M., Stopsack, K. H., Gonzalez-Feliciano, A. G., Markt, S. C., Wilson, K. M., et al. (2020). Statin Use Is Associated with Lower Risk of PTEN-Null and Lethal Prostate Cancer. *Clinical Cancer Research : an Official Journal of the American Association for Cancer Research*, *26*(5), 1086–1093. http://doi.org/10.1158/1078-0432.CCR-19-2853

Amor, C., Feucht, J., Leibold, J., Ho, Y.-J., Zhu, C., Alonso-Curbelo, D., et al. (2020). Senolytic CAR T cells reverse senescence-associated pathologies. *Nature*, *583*(7814), 127–132. http://doi.org/10.1038/s41586-020-2403-9

Anders, S., Pyl, P. T., & Huber, W. (2015). HTSeq--a Python framework to work with high-throughput sequencing data. - PubMed - NCBI. *Bioinformatics*, *31*(2), 166–169. http://doi.org/10.1093/bioinformatics/btu638

Ashworth, A. (2016). A Synthetic Lethal Therapeutic Approach: Poly(ADP) Ribose Polymerase Inhibitors for the Treatment of Cancers Deficient in DNA Double-Strand Break Repair. *Journal of Clinical Oncology*. http://doi.org/10.1200/JCO.2008.16.0812

Baker, D. J., Childs, B. G., Durik, M., Wijers, M. E., Sieben, C. J., Zhong, J., et al. (2016). Naturally occurring p16(Ink4a)-positive cells shorten healthy lifespan. *Nature*, *530*(7589), 184–189. http://doi.org/10.1038/nature16932

Baker, D. J., Wijshake, T., Tchkonia, T., LeBrasseur, N. K., Childs, B. G., van de Sluis, B., et al. (2011). Clearance of p16Ink4a-positive senescent cells delays ageing-associated disorders. *Nature*, *479*(7372), 232–236. http://doi.org/10.1038/nature10600

Baslan, T., Kendall, J., Rodgers, L., Cox, H., Riggs, M., Stepansky, A., et al. (2012). Genome-wide copy number analysis of single cells. *Nature Protocols*, *7*(6), 1024–1041. http://doi.org/10.1038/nprot.2012.039

Baslan, T., Kendall, J., Ward, B., Cox, H., Leotta, A., Rodgers, L., et al. (2015). Optimizing sparse sequencing of single cells for highly multiplex copy number profiling. *Genome Research*, *25*(5), 714–724. http://doi.org/10.1101/gr.188060.114

Binnewies, M., Roberts, E. W., Kersten, K., Chan, V., Fearon, D. F., Merad, M., et al. (2018). Understanding the tumor immune microenvironment (TIME) for effective therapy. *Nature Medicine*, *24*(5), 541–550. http://doi.org/10.1038/s41591-018-0014-x

Blasi, F., & Carmeliet, P. (2002). uPAR: a versatile signalling orchestrator. *Nature Reviews Molecular Cell Biology*, *3*(12), 932–943. http://doi.org/10.1038/nrm977

Bolger, A. M., Lohse, M., & Usadel, B. (2014). Trimmomatic: a flexible trimmer for Illumina sequence data. *Bioinformatics*, *30*(15), 2114–2120. http://doi.org/10.1093/bioinformatics/btu170

Bolton, K. L., Chenevix-Trench, G., Goh, C., Sadetzki, S., Ramus, S. J., Karlan, B. Y., et al. (2012). Association between BRCA1 and BRCA2 mutations and survival in women with invasive epithelial ovarian cancer. *Jama*, *307*(4), 382–390. http://doi.org/10.1001/jama.2012.20

Borgfeldt, C., Hansson, S. R., Gustavsson, B., Måsbäck, A., & Casslén, B. (2001). Dedifferentiation of serous ovarian cancer from cystic to solid tumors is associated with increased expression of mRNA for urokinase plasminogen activator (uPA), its receptor (uPAR) and its inhibitor (PAI-1). *International Journal of Cancer*, *92*(4), 497–502. http://doi.org/10.1002/ijc.1215

Borghaei, H., Paz-Ares, L., Horn, L., Spigel, D. R., Steins, M., Ready, N. E., et al. (2015). Nivolumab versus Docetaxel in Advanced Nonsquamous Non-Small-Cell Lung Cancer. *New England Journal of Medicine*, *373*(17), 1627–1639. http://doi.org/10.1056/NEJMoa1507643

Bowtell, D. D., Böhm, S., Ahmed, A. A., Aspuria, P.-J., Bast, R. C., Beral, V., et al. (2015). Rethinking ovarian cancer II: reducing mortality from high-grade serous ovarian cancer. *Nature Reviews Cancer*, *15*(11), 668–679. http://doi.org/10.1038/nrc4019

Brahmer, J., Reckamp, K. L., Baas, P., Crinò, L., Eberhardt, W. E. E., Poddubskaya, E., et al. (2015). Nivolumab versus Docetaxel in Advanced Squamous-Cell Non-Small-Cell Lung Cancer. *New England Journal of Medicine*, *373*(2), 123–135. http://doi.org/10.1056/NEJMoa1504627

Brentjens, R. J., Latouche, J.-B., Santos, E., Marti, F., Gong, M. C., Lyddane, C., et al. (2003). Eradication of systemic B-cell tumors by genetically targeted human T lymphocytes co-stimulated by CD80 and interleukin-15. *Nature Medicine*, *9*(3), 279–286. http://doi.org/10.1038/nm827

Brosh, R., & Rotter, V. (2009). When mutants gain new powers: news from the mutant p53 field. *Nature Reviews Cancer*, *9*(10), 701–713. http://doi.org/10.1038/nrc2693

Bruand, M., Barras, D., Mina, M., Ghisoni, E., Morotti, M., Lanitis, E., et al. (2021). Cell-autonomous inflammation of BRCA1-deficient ovarian cancers drives both tumor-intrinsic immunoreactivity and immune resistance via STING. *Cell Reports*, *36*(3), 109412. http://doi.org/10.1016/j.celrep.2021.109412

Bunting, S. F., Callén, E., Wong, N., Chen, H.-T., Polato, F., Gunn, A., et al. (2010). 53BP1 inhibits homologous recombination in Brca1-deficient cells by blocking resection of DNA breaks. *Cell*, *141*(2), 243–254. http://doi.org/10.1016/j.cell.2010.03.012

Cairney, C. J., Godwin, L. S., Bilsland, A. E., Burns, S., Stevenson, K. H., McGarry, L., et al. (2017). A “synthetic-sickness” screen for senescence re-engagement targets in mutant cancer backgrounds. *PLoS Genetics*, *13*(8), e1006942. http://doi.org/10.1371/journal.pgen.1006942

Cancer Genome Atlas Research Network. (2011). Integrated genomic analyses of ovarian carcinoma. *Nature*, *474*(7353), 609–615. http://doi.org/10.1038/nature10166

Carroll, B., Nelson, G., Rabanal-Ruiz, Y., Kucheryavenko, O., Dunhill-Turner, N. A., Chesterman, C. C., et al. (2017). Persistent mTORC1 signaling in cell senescence results from defects in amino acid and growth factor sensing. *The Journal of Cell Biology*, *216*(7), 1949–1957. http://doi.org/10.1083/jcb.201610113

Chang, B. D., Broude, E. V., Dokmanovic, M., Zhu, H., Ruth, A., Xuan, Y., et al. (1999). A senescence-like phenotype distinguishes tumor cells that undergo terminal proliferation arrest after exposure to anticancer agents. *Cancer Research*, *59*(15), 3761–3767.

Chapman, M. S., & Verma, I. M. (1996). Transcriptional activation by BRCA1. *Nature*, *382*(6593), 678–679. http://doi.org/10.1038/382678a0

Chicas, A., Wang, X., Zhang, C., McCurrach, M., Zhao, Z., Mert, O., et al. (2010). Dissecting the Unique Role of the Retinoblastoma Tumor Suppressor during Cellular Senescence. *Cancer Cell*, *17*(4), 376–387. http://doi.org/10.1016/j.ccr.2010.01.023

Chien, Y., Scuoppo, C., Wang, X., Fang, X., Balgley, B., Bolden, J. E., et al. (2011). Control of the senescence-associated secretory phenotype by NF-κB promotes senescence and enhances chemosensitivity. *Genes & Development*, *25*(20), 2125–2136. http://doi.org/10.1101/gad.17276711

Childs, B. G., Durik, M., Baker, D. J., & van Deursen, J. M. (2015). Cellular senescence in aging and age-related disease: from mechanisms to therapy. *Nature Medicine*, *21*(12), 1424–1435. http://doi.org/10.1038/nm.4000

Choi, H.-J., Lee, H.-B., Jung, S., Park, H.-K., Jo, W., Cho, S.-M., et al. (2018). Development of a Mouse Model of Prostate Cancer Using the Sleeping Beauty Transposon and Electroporation. *Molecules (Basel, Switzerland)*, *23*(6), 1360. http://doi.org/10.3390/molecules23061360

Connolly, D. C., Bao, R., Nikitin, A. Y., Stephens, K. C., Poole, T. W., Hua, X., et al. (2003). Female mice chimeric for expression of the simian virus 40 TAg under control of the MISIIR promoter develop epithelial ovarian cancer. *Cancer Research*, *63*(6), 1389–1397.

Coppé, J.-P., Desprez, P.-Y., Krtolica, A., & Campisi, J. (2010). The senescence-associated secretory phenotype: the dark side of tumor suppression. *Annual Review of Pathology*, *5*, 99–118. http://doi.org/10.1146/annurev-pathol-121808-102144

Coppé, J.-P., Patil, C. K., Rodier, F., Sun, Y., Muñoz, D. P., Goldstein, J., et al. (2008). Senescence-Associated Secretory Phenotypes Reveal Cell-Nonautonomous Functions of Oncogenic RAS and the p53 Tumor Suppressor. *PLOS Biology*, *6*(12), e301. http://doi.org/10.1371/journal.pbio.0060301

Coppé, J.-P., Rodier, F., Patil, C. K., Freund, A., Desprez, P.-Y., & Campisi, J. (2011). Tumor suppressor and aging biomarker p16(INK4a) induces cellular senescence without the associated inflammatory secretory phenotype.

Journal of Biological Chemistry, *286*(42), 36396–36403. http://doi.org/10.1074/jbc.M111.257071
Dai, Y., Sun, C., Feng, Y., Jia, Q., & Zhu, B. (2018). Potent immunogenicity in BRCA1-mutated patients with high-grade serous ovarian carcinoma. *Journal of Cellular and Molecular Medicine*, *22*(8), 3979–3986. http://doi.org/10.1111/jcmm.13678
Dasari, S., & Tchounwou, P. B. (2014). Cisplatin in cancer therapy: molecular mechanisms of action. *European Journal of Pharmacology*, *740*, 364–378. http://doi.org/10.1016/j.ejphar.2014.07.025
Debacq-Chainiaux, F., Erusalimsky, J. D., Campisi, J., & Toussaint, O. (2009). Protocols to detect senescence-associated beta-galactosidase (SA-βgal) activity, a biomarker of senescent cells in culture and in vivo. *Nature Protocols*, *4*(12), 1798–1806. http://doi.org/10.1038/nprot.2009.191
DelloRusso, C., Welcsh, P. L., Wang, W., Garcia, R. L., King, M.-C., & Swisher, E. M. (2007). Functional characterization of a novel BRCA1-null ovarian cancer cell line in response to ionizing radiation. *Molecular Cancer Research*, *5*(1), 35–45. http://doi.org/10.1158/1541-7786.MCR-06-0234
Demaria, M., O'Leary, M. N., Chang, J., Shao, L., Liu, S., Alimirah, F., et al. (2017). Cellular Senescence Promotes Adverse Effects of Chemotherapy and Cancer Relapse. *Cancer Discovery*, *7*(2), 165–176. http://doi.org/10.1158/2159-8290.CD-16-0241
Di Mitri, D., & Alimonti, A. (2016). Non-Cell-Autonomous Regulation of Cellular Senescence in Cancer. *Trends in Cell Biology*, *26*(3), 215–226. http://doi.org/10.1016/j.tcb.2015.10.005
Di Mitri, D., Toso, A., Chen, J. J., Sarti, M., Pinton, S., Jost, T. R., et al. (2014). Tumour-infiltrating Gr-1+ myeloid cells antagonize senescence in cancer. *Nature*, *515*(7525), 134–137. http://doi.org/10.1038/nature13638
Ding, L., Kim, H.-J., Wang, Q., Kearns, M., Jiang, T., Ohlson, C. E., et al. (2018). PARP Inhibition Elicits STING-Dependent Antitumor Immunity in Brca1-Deficient Ovarian Cancer. *Cell Reports*, *25*(11), 2972–2980.e5. http://doi.org/10.1016/j.celrep.2018.11.054
Disis, M. L., Patel, M. R., Pant, S., Hamilton, E. P., Lockhart, A. C., Kelly, K., et al. (2016). Avelumab (MSB0010718C; anti-PD-L1) in patients with recurrent/refractory ovarian cancer from the JAVELIN Solid Tumor phase Ib trial: Safety and clinical activity. *Journal of Clinical Oncology*, *34*(15_suppl), 5533–5533. http://doi.org/10.1200/JCO.2016.34.15_suppl.5533
Disis, M. L., Taylor, M. H., Kelly, K., Beck, J. T., Gordon, M., Moore, K. M., et al. (2019). Efficacy and Safety of Avelumab for Patients With Recurrent or Refractory Ovarian Cancer. *JAMA Oncology*, *5*(3), 393–9. http://doi.org/10.1001/jamaoncol.2018.6258
Dobin, A., Davis, C. A., Schlesinger, F., Drenkow, J., Zaleski, C., Jha, S., et al. (2012). STAR: ultrafast universal RNA-seq aligner. *Bioinformatics*, *29*(1), 15–21. http://doi.org/10.1093/bioinformatics/bts635
Dou, Z., Ghosh, K., Vizioli, M. G., Zhu, J., Sen, P., Wangensteen, K. J., et al. (2017). Cytoplasmic chromatin triggers inflammation in senescence and

cancer. *Nature Reviews Cancer*, *166*, 1–21. http://doi.org/10.1038/nature24050

Elloul, S., Elstrand, M. B., Nesland, J. M., Tropé, C. G., Kvalheim, G., Goldberg, I., et al. (2005). Snail, Slug, and Smad-interacting protein 1 as novel parameters of disease aggressiveness in metastatic ovarian and breast carcinoma. *Cancer*, *103*(8), 1631–1643. http://doi.org/10.1002/cncr.20946

Elstrodt, F., Hollestelle, A., Nagel, J. H. A., Gorin, M., Wasielewski, M., van den Ouweland, A., et al. (2006). BRCA1 mutation analysis of 41 human breast cancer cell lines reveals three new deleterious mutants. *Cancer Research*, *66*(1), 41–45. http://doi.org/10.1158/0008-5472.CAN-05-2853

Ewald, J. A., Desotelle, J. A., Wilding, G., & Jarrard, D. F. (2010). Therapy-induced senescence in cancer. *Journal of the National Cancer Institute*, *102*(20), 1536–1546. http://doi.org/10.1093/jnci/djq364

Faget, D. V., Ren, Q., & Stewart, S. A. (2019). Unmasking senescence: context-dependent effects of SASP in cancer. *Nature Reviews Cancer*, *19*(8), 439–453. http://doi.org/10.1038/s41568-019-0156-2

Farmer, H., McCabe, N., Lord, C. J., Tutt, A. N. J., Johnson, D. A., Richardson, T. B., et al. (2005). Targeting the DNA repair defect in BRCA mutant cells as a therapeutic strategy. *Nature*, *434*(7035), 917–921. http://doi.org/10.1038/nature03445

Färkkilä, A., Gulhan, D. C., Casado, J., Jacobson, C. A., Nguyen, H., Kochupurakkal, B., et al. (2020). Immunogenomic profiling determines responses to combined PARP and PD-1 inhibition in ovarian cancer. *Nature Communications*, *11*(1), 1459–13. http://doi.org/10.1038/s41467-020-15315-8

Flesken-Nikitin, A., Choi, K.-C., Eng, J. P., Shmidt, E. N., & Nikitin, A. Y. (2003). Induction of carcinogenesis by concurrent inactivation of p53 and Rb1 in the mouse ovarian surface epithelium. *Cancer Research*, *63*(13), 3459–3463.

Fleury, H., Malaquin, N., Tu, V., Gilbert, S., Martinez, A., Olivier, M.-A., et al. (2019). Exploiting interconnected synthetic lethal interactions between PARP inhibition and cancer cell reversible senescence. *Nature Communications*, 1–15. http://doi.org/10.1038/s41467-019-10460-1

Fournel, L., Wu, Z., Stadler, N., Damotte, D., Lococo, F., Boulle, G., et al. (2019). Cisplatin increases PD-L1 expression and optimizes immune check-point blockade in non-small cell lung cancer. *Cancer Letters*, *464*, 5–14. http://doi.org/10.1016/j.canlet.2019.08.005

Fumagalli, M., Rossiello, F., Clerici, M., Barozzi, S., Cittaro, D., Kaplunov, J. M., et al. (2012). Telomeric DNA damage is irreparable and causes persistent DNA-damage-response activation. *Nature Cell Biology*, *14*(4), 355–365. http://doi.org/10.1038/ncb2466

Gewirtz, D. A., Holt, S. E., & Elmore, L. W. (2008). Accelerated senescence: an emerging role in tumor cell response to chemotherapy and radiation. *Biochemical Pharmacology*, *76*(8), 947–957. http://doi.org/10.1016/j.bcp.2008.06.024

Glück, S., Guey, B., Gulen, M. F., Wolter, K., Kang, T.-W., Schmacke, N. A., et al. (2017). Innate immune sensing of cytosolic chromatin fragments through

cGAS promotes senescence. *Nature Cell Biology*, *19*(9), 1061–1070. http://doi.org/10.1038/ncb3586
Gorgoulis, V., Adams, P. D., Alimonti, A., Bennett, D. C., Bischof, O., Bishop, C., et al. (2019). Cellular Senescence: Defining a Path Forward. *Cell*, *179*(4), 813–827. http://doi.org/10.1016/j.cell.2019.10.005
Grabosch, S., Bulatovic, M., Zeng, F., Ma, T., Zhang, L., Ross, M., et al. (2019). Cisplatin-induced immune modulation in ovarian cancer mouse models with distinct inflammation profiles. *Oncogene*, 1–14. http://doi.org/10.1038/s41388-018-0581-9
Greenaway, J., Moorehead, R., Shaw, P., & Petrik, J. (2008). Epithelial-stromal interaction increases cell proliferation, survival and tumorigenicity in a mouse model of human epithelial ovarian cancer. *Gynecologic Oncology*, *108*(2), 385–394. http://doi.org/10.1016/j.ygyno.2007.10.035
Hall, B. M., Balan, V., Gleiberman, A. S., Strom, E., Krasnov, P., Virtuoso, L. P., et al. (2016). Aging of mice is associated with p16(Ink4a)- and β-galactosidase-positive macrophage accumulation that can be induced in young mice by senescent cells. *Aging*, *8*(7), 1294–1315. http://doi.org/10.18632/aging.100991
Hamanishi, J., Mandai, M., Ikeda, T., Minami, M., Kawaguchi, A., Murayama, T., et al. (2015). Safety and Antitumor Activity of Anti-PD-1 Antibody, Nivolumab, in Patients With Platinum-Resistant Ovarian Cancer. - PubMed - NCBI. *Journal of Clinical Oncology*, *33*(34), 4015–4022.
Hao, D., Li, J., Jia, S., Meng, Y., Zhang, C., Wang, L., & Di, L.-J. (2017). Integrated Analysis Reveals Tubal- and Ovarian-Originated Serous Ovarian Cancer and Predicts Differential Therapeutic Responses. *Clinical Cancer Research : an Official Journal of the American Association for Cancer Research*, *23*(23), 7400–7411. http://doi.org/10.1158/1078-0432.CCR-17-0638
Hao, X., Zhao, B., Zhou, W., Liu, H., Fukumoto, T., Gabrilovich, D., & Zhang, R. (2021). Sensitization of ovarian tumor to immune checkpoint blockade by boosting senescence- associated secretory phenotype. *iScience*, *24*(1), 102016. http://doi.org/10.1016/j.isci.2020.102016
Hayflick, L., & Moorhead, P. S. (1961). The serial cultivation of human diploid cell strains. *Experimental Cell Research*, *25*, 585–621. http://doi.org/10.1016/0014-4827(61)90192-6
Heijink, A. M., Talens, F., Jae, L. T., van Gijn, S. E., Fehrmann, R. S. N., Brummelkamp, T. R., & van Vugt, M. A. T. M. (2019). BRCA2 deficiency instigates cGAS-mediated inflammatory signaling and confers sensitivity to tumor necrosis factor-alpha-mediated cytotoxicity. *Nature Communications*, *10*(1), 100–14. http://doi.org/10.1038/s41467-018-07927-y
Herbst, R. S., Soria, J.-C., Kowanetz, M., Fine, G. D., Hamid, O., Gordon, M. S., et al. (2014). Predictive correlates of response to the anti-PD-L1 antibody MPDL3280A in cancer patients. *Nature*, *515*(7528), 563–567. http://doi.org/10.1038/nature14011
Hernandez-Segura, A., de Jong, T. V., Melov, S., Guryev, V., Campisi, J., & Demaria, M. (2017). Unmasking Transcriptional Heterogeneity in Senescent

Cells. *Current Biology*, *27*(17), 2652–2660.e4. http://doi.org/10.1016/j.cub.2017.07.033
Hernandez-Segura, A., Nehme, J., & Demaria, M. (2018). Hallmarks of Cellular Senescence. *Trends in Cell Biology*, *28*(6), 436–453. http://doi.org/10.1016/j.tcb.2018.02.001
Hill, S. J., Decker, B., Roberts, E. A., Horowitz, N. S., Muto, M. G., Worley, M. J., et al. (2018). Prediction of DNA Repair Inhibitor Response in Short-Term Patient-Derived Ovarian Cancer Organoids. *Cancer Discovery*, *8*(11), 1404–1421. http://doi.org/10.1158/2159-8290.CD-18-0474
Hoare, M., Ito, Y., Kang, T.-W., Weekes, M. P., Matheson, N. J., Patten, D. A., et al. (2016). NOTCH1 mediates a switch between two distinct secretomes during senescence. *Nature Cell Biology*, *18*(9), 979–992. http://doi.org/10.1038/ncb3397
Huang, B., Song, B.-L., & Xu, C. (2020). Cholesterol metabolism in cancer: mechanisms and therapeutic opportunities. *Nature Metabolism*, *2*(2), 132–141. http://doi.org/10.1038/s42255-020-0174-0
Hwang, W.-T., Adams, S. F., Tahirovic, E., Hagemann, I. S., & Coukos, G. (2012). Prognostic significance of tumor-infiltrating T cells in ovarian cancer: A meta-analysis. *Gynecologic Oncology*, *124*(2), 192–198. http://doi.org/10.1016/j.ygyno.2011.09.039
Ingemarsdotter, C. K., Tookman, L. A., Browne, A., Pirlo, K., Cutts, R., Chelela, C., et al. (2015). Paclitaxel resistance increases oncolytic adenovirus efficacy via upregulated CAR expression and dysfunctional cell cycle control. *Molecular Oncology*, *9*(4), 791–805. http://doi.org/10.1016/j.molonc.2014.12.007
Iyer, S., Zhang, S., Yucel, S., Horn, H., Smith, S. G., Reinhardt, F., et al. (2020). Genetically defined syngeneic mouse models of ovarian cancer as tools for the discovery of combination immunotherapy. *Cancer Discovery*, CD–20–0818–53. http://doi.org/10.1158/2159-8290.CD-20-0818
Jarboe, E., Folkins, A., Nucci, M. R., Kindelberger, D., Drapkin, R., Miron, A., et al. (2008). Serous carcinogenesis in the fallopian tube: a descriptive classification. *International Journal of Gynecological Pathology : Official Journal of the International Society of Gynecological Pathologists*, *27*(1), 1–9. http://doi.org/10.1097/pgp.0b013e31814b191f
Jemal, A., Bray, F., Center, M. M., Ferlay, J., Ward, E., & Forman, D. (2011). Global cancer statistics. *CA: a Cancer Journal for Clinicians*, *61*(2), 69–90. http://doi.org/10.3322/caac.20107
Jiménez-Sanchez, A., Cybulska, P., Mager, K. L., Koplev, S., Cast, O., Couturier, D.-L., et al. (2020). Unraveling tumor–immune heterogeneity in advanced ovarian cancer uncovers immunogenic effect of chemotherapy. *Nature Genetics*, 1–21. http://doi.org/10.1038/s41588-020-0630-5
Jochems, F., Thijssen, B., De Conti, G., Jansen, R., Pogacar, Z., Groot, K., et al. (2021). The Cancer SENESCopedia: A delineation of cancer cell senescence. *Cell Reports*, *36*(4), 109441. http://doi.org/10.1016/j.celrep.2021.109441

Kang, T.-W., Yevsa, T., Woller, N., Hoenicke, L., Wuestefeld, T., Dauch, D., et al. (2011). Senescence surveillance of pre-malignant hepatocytes limits liver cancer development. *Nature*, *479*(7374), 547–551. http://doi.org/10.1038/nature10599

Karnezis, A. N., Cho, K. R., Gilks, C. B., Pearce, C. L., & Huntsman, D. G. (2017). The disparate origins of ovarian cancers: pathogenesis and prevention strategies. *Nature Reviews Cancer*, *17*(1), 65–74. http://doi.org/10.1038/nrc.2016.113

Karst, A. M., Levanon, K., & Drapkin, R. (2011). Modeling high-grade serous ovarian carcinogenesis from the fallopian tube. *Proceedings of the National Academy of Sciences*, *108*(18), 7547–7552. http://doi.org/10.1073/pnas.1017300108

Katz, S. C., Point, G. R., Cunetta, M., Thorn, M., Guha, P., Espat, N. J., et al. (2019). Regional CAR-T cell infusions for peritoneal carcinomatosis are superior to systemic delivery, 1–7. http://doi.org/10.1038/cgt.2016.14

Keenan, T. E., Burke, K. P., & Van Allen, E. M. (2019). Genomic correlates of response to immune checkpoint blockade. *Nature Medicine*, *25*(3), 389–402. http://doi.org/10.1038/s41591-019-0382-x

Kenny, H. A., Leonhardt, P., Ladanyi, A., Yamada, S. D., Montag, A., Im, H. K., et al. (2011). Targeting the urokinase plasminogen activator receptor inhibits ovarian cancer metastasis. *Clinical Cancer Research : an Official Journal of the American Association for Cancer Research*, *17*(3), 459–471. http://doi.org/10.1158/1078-0432.CCR-10-2258

Klotz, D. M., & Wimberger, P. (2017). Cells of origin of ovarian cancer: ovarian surface epithelium or fallopian tube? *Archives of Gynecology and Obstetrics*, *296*(6), 1055–1062. http://doi.org/10.1007/s00404-017-4529-z

Konstantinopoulos, P. A., Ceccaldi, R., Shapiro, G. I., & D'Andrea, A. D. (2015). Homologous Recombination Deficiency: Exploiting the Fundamental Vulnerability of Ovarian Cancer. *Cancer Discovery*, *5*(11), 1137–1154. http://doi.org/10.1158/2159-8290.CD-15-0714

Kook, Y. H., Adamski, J., Zelent, A., & Ossowski, L. (1994). The effect of antisense inhibition of urokinase receptor in human squamous cell carcinoma on malignancy. *The EMBO Journal*, *13*(17), 3983–3991. http://doi.org/10.1002/j.1460-2075.1994.tb06714.x

Kopper, O., de Witte, C. J., Lõhmussaar, K., Valle-Inclan, J. E., Hami, N., Kester, L., et al. (2019). An organoid platform for ovarian cancer captures intra- and interpatient heterogeneity. *Nature Medicine*, 1–27. http://doi.org/10.1038/s41591-019-0422-6

Krizhanovsky, V., Yon, M., Dickins, R. A., Hearn, S., Simon, J., Miething, C., et al. (2008). Senescence of activated stellate cells limits liver fibrosis. *Cell*, *134*(4), 657–667. http://doi.org/10.1016/j.cell.2008.06.049

Kuilman, T., Michaloglou, C., Mooi, W. J., & Peeper, D. S. (2010). The essence of senescence. *Genes & Development*, *24*(22), 2463–2479. http://doi.org/10.1101/gad.1971610

Kuilman, T., Michaloglou, C., Vredeveld, L. C. W., Douma, S., van Doorn, R., Desmet, C. J., et al. (2008). Oncogene-induced senescence relayed by an

interleukin-dependent inflammatory network. *Cell*, *133*(6), 1019–1031. http://doi.org/10.1016/j.cell.2008.03.039
Kurman, R. J., Carcangiu, M. L., Herrington, C. S., & Young, R. H. (2014). WHO Classification of Tumours of Female Reproductive Organs. Fourth Edition. Retrieved April 24, 2020, from https://apps.who.int/bookorders/anglais/detart1.jsp?codlan=1&codcol=70&codcch=4006
Labidi-Galy, S. I., Papp, E., Hallberg, D., Niknafs, N., Adleff, V., Noe, M., et al. (2017). High grade serous ovarian carcinomas originate in the fallopian tube. *Nature Communications*, *8*(1), 1093. http://doi.org/10.1038/s41467-017-00962-1
Lane, D., & Levine, A. (2010). p53 Research: the past thirty years and the next thirty years. *Cold Spring Harbor Perspectives in Biology*, *2*(12), a000893–a000893. http://doi.org/10.1101/cshperspect.a000893
Lawrenson, K., Fonseca, M. A. S., Liu, A. Y., Dezem, F. S., Lee, J. M., Lin, X., et al. (2019). A Study of High-Grade Serous Ovarian Cancer Origins Implicates the SOX18 Transcription Factor in Tumor Development. *Cell Reports*, *29*(11), 3726–3735.e4. http://doi.org/10.1016/j.celrep.2019.10.122
Ledermann, J. A., Colombo, N., Oza, A. M., Fujiwara, K., Birrer, M. J., Randall, L. M., et al. (2020). Avelumab in combination with and/or following chemotherapy vs chemotherapy alone in patients with previously untreated epithelial ovarian cancer: Results from the phase 3 javelin ovarian 100 trial. *Gynecologic Oncology*, *159*, 13–14. http://doi.org/10.1016/j.ygyno.2020.06.025
Lee, S., Yu, Y., Trimpert, J., Benthani, F., Mairhofer, M., Richter-Pechanska, P., et al. (2021). Virus-induced senescence is a driver and therapeutic target in COVID-19. *Nature*, *599*(7884), 283–289. http://doi.org/10.1038/s41586-021-03995-1
Leibold, J., Ruscetti, M., Cao, Z., Ho, Y.-J., Baslan, T., Zou, M., et al. (2020). Somatic Tissue Engineering in Mouse Models Reveals an Actionable Role for WNT Pathway Alterations in Prostate Cancer Metastasis. *Cancer Discovery*, *10*(7), 1038–1057. http://doi.org/10.1158/2159-8290.CD-19-1242
Lengyel, E. (2010). Ovarian Cancer Development and Metastasis. *The American Journal of Pathology*, *177*(3), 1053–1064. http://doi.org/10.2353/ajpath.2010.100105
Li, T., & Chen, Z. J. (2018). The cGAS-cGAMP-STING pathway connects DNA damage to inflammation, senescence, and cancer. *The Journal of Experimental Medicine*, *215*(5), 1287–1299. http://doi.org/10.1084/jem.20180139
Liu, Y. L., & Zamarin, D. (2018). Combination Immune Checkpoint Blockade Strategies to Maximize Immune Response in Gynecological Cancers. *Current Oncology Reports*, *20*(12), 94–11. http://doi.org/10.1007/s11912-018-0740-8
Liu, Y. L., Selenica, P., Zhou, Q., Iasonos, A., Callahan, M., Feit, N. Z., et al. (2020). BRCAMutations, Homologous DNA Repair Deficiency, Tumor Mutational Burden, and Response to Immune Checkpoint Inhibition in

Recurrent Ovarian Cancer. *JCO Precision Oncology*, (4), 665–679. http://doi.org/10.1200/PO.20.00069
Love, M. I., Huber, W., & Anders, S. (2014). Moderated estimation of fold change and dispersion for RNA-seq data with DESeq2. *Genome Biology*, *15*(12), 1–21. http://doi.org/10.1186/s13059-014-0550-8
Lõhmussaar, K., Kopper, O., Korving, J., Begthel, H., Vreuls, C. P. H., Es, J. H., & Clevers, H. (2020). Assessing the origin of high-grade serous ovarian cancer using CRISPR-modification of mouse organoids. *Nature Communications*, 1–14. http://doi.org/10.1038/s41467-020-16432-0
Lujambio, A., Akkari, L., Simon, J., Grace, D., Tschaharganeh, D. F., Bolden, J. E., et al. (2013). Non-Cell-Autonomous Tumor Suppression by p53. *Cell*, *153*(2), 449–460. http://doi.org/10.1016/j.cell.2013.03.020
Ma, X., Bi, E., Lu, Y., Su, P., Huang, C., Liu, L., et al. (2019). Cholesterol Induces CD8+ T Cell Exhaustion in the Tumor Microenvironment. *Cell Metabolism*, *30*(1), 143–156.e5. http://doi.org/10.1016/j.cmet.2019.04.002
Macintyre, G., Goranova, T. E., De Silva, D., Ennis, D., Piskorz, A. M., Eldridge, M., et al. (2018). Copy number signatures and mutational processes in ovarian carcinoma. *Nature Genetics*, *50*(9), 1262–1270. http://doi.org/10.1038/s41588-018-0179-8
Mackenzie, K. J., Carroll, P., Martin, C.-A., Murina, O., Fluteau, A., Simpson, D. J., et al. (2017). cGAS surveillance of micronuclei links genome instability to innate immunity. *Nature*, *548*(7668), 461–465. http://doi.org/10.1038/nature23449
Maniati, E., Berlato, C., Gopinathan, G., Heath, O., Kotantaki, P., Lakhani, A., et al. (2020). Mouse Ovarian Cancer Models Recapitulate the Human Tumor Microenvironment and Patient Response to Treatment. *Cell Reports*, *30*(2), 525–540.e7. http://doi.org/10.1016/j.celrep.2019.12.034
Maresch, R., Mueller, S., Veltkamp, C., Öllinger, R., Friedrich, M., Heid, I., et al. (2016). Multiplexed pancreatic genome engineering and cancer induction by transfection-based CRISPR/Cas9 delivery in mice. *Nature Communications*, *7*, 10770. http://doi.org/10.1038/ncomms10770
Martins, F. C., de Santiago, I., Trinh, A., Xian, J., Guo, A., Sayal, K., et al. (2014). Combined image and genomic analysis of high-grade serous ovarian cancer reveals PTEN loss as a common driver event and prognostic classifier. *Genome Biology*, *15*(12), 1–15. http://doi.org/10.1186/s13059-014-0526-8
Maru, Y., Tanaka, N., Itami, M., & Hippo, Y. (2019). Efficient use of patient-derived organoids as a preclinical model for gynecologic tumors. *Gynecologic Oncology*, *154*(1), 189–198. http://doi.org/10.1016/j.ygyno.2019.05.005
Matulonis, U. A. (2018). Ovarian Cancer. *Hematology/Oncology Clinics of North America*, *32*(6), xiii–xiv. http://doi.org/10.1016/j.hoc.2018.09.006
Matulonis, U. A., Shapira-Frommer, R., Santin, A. D., Lisyanskaya, A. S., Pignata, S., Vergote, I., et al. (2019). Antitumor activity and safety of pembrolizumab in patients with advanced recurrent ovarian cancer: results from the phase II KEYNOTE-100 study. *Annals of Oncology*, *30*(7), 1080–1087. http://doi.org/10.1093/annonc/mdz135

Mazar, A. P. (2008). Urokinase plasminogen activator receptor choreographs multiple ligand interactions: implications for tumor progression and therapy. *Clinical Cancer Research : an Official Journal of the American Association for Cancer Research*, *14*(18), 5649–5655. http://doi.org/10.1158/1078-0432.CCR-07-4863

McCool, K. W., Freeman, Z. T., Zhai, Y., Wu, R., Hu, K., Liu, C.-J., et al. (2020). Murine Oviductal High-Grade Serous Carcinomas Mirror the Genomic Alterations, Gene Expression Profiles, and Immune Microenvironment of Their Human Counterparts. *Cancer Research*, *80*(4), 877–889. http://doi.org/10.1158/0008-5472.CAN-19-2558

Moiseeva, O., Bourdeau, V., Roux, A., Deschênes-Simard, X., & Ferbeyre, G. (2009). Mitochondrial dysfunction contributes to oncogene-induced senescence. *Molecular and Cellular Biology*, *29*(16), 4495–4507. http://doi.org/10.1128/MCB.01868-08

Moore, K. N., Bookman, M., Sehouli, J., Miller, A., Anderson, C., Scambia, G., et al. (2020). LBA31 Primary results from IMagyn050/GOG 3015/ENGOT-OV39, a double-blind placebo (pbo)-controlled randomised phase III trial of bevacizumab (bev)-containing therapy +/- atezolizumab (atezo) for newly diagnosed stage III/IV ovarian cancer (OC). *Annals of Oncology*, *31*, S1161–S1162. http://doi.org/10.1016/j.annonc.2020.08.2261

Morin, P. J., & Weeraratna, A. T. (2015). Genetically-defined ovarian cancer mouse models. *The Journal of Pathology*, *238*(2), 180–184. http://doi.org/10.1002/path.4663

Motohara, T., Masuko, S., Ishimoto, T., Yae, T., Onishi, N., Muraguchi, T., et al. (2011). Transient depletion of p53 followed by transduction of c-Myc and K-Ras converts ovarian stem-like cells into tumor-initiating cells. *Carcinogenesis*, *32*(11), 1597–1606. http://doi.org/10.1093/carcin/bgr183

Mullen, P. J., Yu, R., Longo, J., Archer, M. C., & Penn, L. Z. (2016). The interplay between cell signalling and the mevalonate pathway in cancer. *Nature Reviews Cancer*, *16*(11), 718–731. http://doi.org/10.1038/nrc.2016.76

Naumann, R. W., Morris, J. C., Tait, D. L., Higgins, R. V., Crane, E. K., Drury, L. K., et al. (2018). Patients with BRCA mutations have superior outcomes after intraperitoneal chemotherapy in optimally resected high grade ovarian cancer. *Gynecologic Oncology*, *151*(3), 477–480. http://doi.org/10.1016/j.ygyno.2018.10.003

Network, T. C. G. A. R., Raphael, B. J., Hruban, R. H., Aguirre, A. J., Moffitt, R. A., Yeh, J. J., et al. (2017). Integrated Genomic Characterization of Pancreatic Ductal Adenocarcinoma. *Cancer Cell*, *32*(2), 185–203.e13. http://doi.org/10.1016/j.ccell.2017.07.007

O'Donovan, P. J., & Livingston, D. M. (2010). BRCA1 and BRCA2: breast/ovarian cancer susceptibility gene products and participants in DNA double-strand break repair. *Carcinogenesis*, *31*(6), 961–967. http://doi.org/10.1093/carcin/bgq069

Odunsi, K. (2017). Immunotherapy in ovarian cancer. *Annals of Oncology*, *28*(suppl_8), viii1–viii7. http://doi.org/10.1093/annonc/mdx444

Orsulic, S., Li, Y., Soslow, R. A., Vitale-Cross, L. A., Gutkind, J. S., & Varmus, H. E. (2002). Induction of ovarian cancer by defined multiple genetic changes in a mouse model system. *Cancer Cell*, *1*(1), 53–62.

Ovarian Tumor Tissue Analysis (OTTA) Consortium, Goode, E. L., Block, M. S., Kalli, K. R., Vierkant, R. A., Chen, W., et al. (2017). Dose-Response Association of CD8+ Tumor-Infiltrating Lymphocytes and Survival Time in High-Grade Serous Ovarian Cancer. *JAMA Oncology*, *3*(12), e173290–e173290. http://doi.org/10.1001/jamaoncol.2017.3290

Pantelidou, C., Sonzogni, O., De Oliveria Taveira, M., Mehta, A. K., Kothari, A., Wang, D., et al. (2019). PARP Inhibitor Efficacy Depends on CD8+ T-cell Recruitment via Intratumoral STING Pathway Activation in BRCA-Deficient Models of Triple-Negative Breast Cancer. *Cancer Discovery*, *9*(6), 722–737. http://doi.org/10.1158/2159-8290.CD-18-1218

Park, J. H., Rivière, I., Gönen, M., Wang, X., Sénéchal, B., Curran, K. J., et al. (2018). Long-Term Follow-up of CD19 CAR Therapy in Acute Lymphoblastic Leukemia. *New England Journal of Medicine*, *378*(5), 449–459. http://doi.org/10.1056/NEJMoa1709919

Park, J.-S., Lim, K.-M., Park, S. G., Jung, S. Y., Choi, H.-J., Lee, D. H., et al. (2014). Pancreatic cancer induced by in vivo electroporation-enhanced sleeping beauty transposon gene delivery system in mouse. *Pancreas*, *43*(4), 614–618. http://doi.org/10.1097/MPA.0000000000000102

Parkes, E. E., Walker, S. M., Taggart, L. E., McCabe, N., Knight, L. A., Wilkinson, R., et al. (2017). Activation of STING-Dependent Innate Immune Signaling By S-Phase-Specific DNA Damage in Breast Cancer. *Journal of the National Cancer Institute*, *109*(1), djw199. http://doi.org/10.1093/jnci/djw199

Patch, A.-M., Christie, E. L., Etemadmoghadam, D., Garsed, D. W., George, J., Fereday, S., et al. (2015). Whole-genome characterization of chemoresistant ovarian cancer. *Nature*, *521*(7553), 489–494. http://doi.org/10.1038/nature14410

Pearce, O. M. T., Delaine-Smith, R. M., Maniati, E., Nichols, S., Wang, J., Böhm, S., et al. (2018). Deconstruction of a Metastatic Tumor Microenvironment Reveals a Common Matrix Response in Human Cancers. *Cancer Discovery*, *8*(3), 304–319. http://doi.org/10.1158/2159-8290.CD-17-0284

Peres, L. C., Cushing-Haugen, K. L., Köbel, M., Harris, H. R., Berchuck, A., Rossing, M. A., et al. (2019). Invasive Epithelial Ovarian Cancer Survival by Histotype and Disease Stage. *Journal of the National Cancer Institute*, *111*(1), 60–68. http://doi.org/10.1093/jnci/djy071

Perets, R., Wyant, G. A., Muto, K. W., Bijron, J. G., Poole, B. B., Chin, K. T., et al. (2013). Transformation of the Fallopian Tube Secretory Epithelium Leads to High-Grade Serous Ovarian Cancer in Brca;Tp53;Pten Models. *Cancer Cell*, *24*(6), 751–765. http://doi.org/10.1016/j.ccr.2013.10.013

Pluquet, O., Pourtier, A., & Abbadie, C. (2015). The unfolded protein response and cellular senescence. A review in the theme: cellular mechanisms of endoplasmic reticulum stress signaling in health and disease. *American Journal of Physiology. Cell Physiology*, *308*(6), C415–25. http://doi.org/10.1152/ajpcell.00334.2014

Pujade-Lauraine, E., Fujiwara, K., Ledermann, J. A., Oza, A. M., Kristeleit, R., Ray-Coquard, I.-L., et al. (2021). Avelumab alone or in combination with chemotherapy versus chemotherapy alone in platinum-resistant or platinum-refractory ovarian cancer (JAVELIN Ovarian 200): an open-label, three-arm, randomised, phase 3 study. *The Lancet. Oncology*, *22*(7), 1034–1046. http://doi.org/10.1016/S1470-2045(21)00216-3

Ritschka, B., Storer, M., Mas, A., Heinzmann, F., Ortells, M. C., Morton, J. P., et al. (2017). The senescence-associated secretory phenotype induces cellular plasticity and tissue regeneration. *Genes & Development*, *31*(2), 172–183. http://doi.org/10.1101/gad.290635.116

Roby, K. F., Taylor, C. C., Sweetwood, J. P., Cheng, Y., Pace, J. L., Tawfik, O., et al. (2000). Development of a syngeneic mouse model for events related to ovarian cancer. *Carcinogenesis*, *21*(4), 585–591. http://doi.org/10.1093/carcin/21.4.585

Rodier, F., Coppé, J.-P., Patil, C. K., Hoeijmakers, W. A. M., Muñoz, D. P., Raza, S. R., et al. (2009). Persistent DNA damage signalling triggers senescence-associated inflammatory cytokine secretion. *Nature Cell Biology*, *11*(8), 973–979. http://doi.org/10.1038/ncb1909

Rottenberg, S., Disler, C., & Perego, P. (2021). The rediscovery of platinum-based cancer therapy. *Nature Reviews Cancer*, *21*(1), 37–50. http://doi.org/10.1038/s41568-020-00308-y

Ruhland, M. K., Loza, A. J., Capietto, A.-H., Luo, X., Knolhoff, B. L., Flanagan, K. C., et al. (2016). Stromal senescence establishes an immunosuppressive microenvironment that drives tumorigenesis. *Nature Communications*, *7*(1), 11762–18. http://doi.org/10.1038/ncomms11762

Ruscetti, M., Leibold, J., Bott, M. J., Fennell, M., Kulick, A., Salgado, N. R., et al. (2018). NK cell–mediated cytotoxicity contributes to tumor control by a cytostatic drug combination. *Science*, *362*(6421), 1416–1422. http://doi.org/10.1126/science.aas9090

Ruscetti, M., Morris, J. P., Mezzadra, R., Russell, J., Leibold, J., Romesser, P. B., et al. (2020). Senescence-Induced Vascular Remodeling Creates Therapeutic Vulnerabilities in Pancreas Cancer. *Cell*, *181*(2), 424–441.e21. http://doi.org/10.1016/j.cell.2020.03.008

Saborowski, M., Saborowski, A., Morris, J. P., Bosbach, B., Dow, L. E., Pelletier, J., et al. (2014). A modular and flexible ESC-based mouse model of pancreatic cancer. *Genes & Development*, *28*(1), 85–97. http://doi.org/10.1101/gad.232082.113

Sadelain, M., Rivière, I., & Riddell, S. (2017). Therapeutic T cell engineering. *Nature*, *545*(7655), 423–431. http://doi.org/10.1038/nature22395

Schlienger, K., Chu, C. S., Woo, E. Y., Rivers, P. M., Toll, A. J., Hudson, B., et al. (2003). TRANCE- and CD40 ligand-matured dendritic cells reveal MHC class I-restricted T cells specific for autologous tumor in late-stage ovarian cancer patients. *Clinical Cancer Research : an Official Journal of the American Association for Cancer Research*, *9*(4), 1517–1527.

Schmitt, C. A., Fridman, J. S., Yang, M., Lee, S., Baranov, E., Hoffman, R. M., & Lowe, S. W. (2002). A senescence program controlled by p53 and p16INK4a

contributes to the outcome of cancer therapy. *Cell*, *109*(3), 335–346. http://doi.org/10.1016/s0092-8674(02)00734-1
Scully, R. E. (1995). Pathology of ovarian cancer precursors. *Journal of Cellular Biochemistry. Supplement*, *23*(S23), 208–218. http://doi.org/10.1002/jcb.240590928
Serrano, M., Lin, A. W., McCurrach, M. E., Beach, D., & Lowe, S. W. (1997). Oncogenic ras provokes premature cell senescence associated with accumulation of p53 and p16INK4a. *Cell*, *88*(5), 593–602.
Sharpless, N. E., & Sherr, C. J. (2015). Forging a signature of in vivo senescence. *Nature Reviews Cancer*, *15*(7), 397–408. http://doi.org/10.1038/nrc3960
Sherman-Baust, C. A., Kuhn, E., Valle, B. L., Shih, I.-M., Kurman, R. J., Wang, T.-L., et al. (2014). A genetically engineered ovarian cancer mouse model based on fallopian tube transformation mimics human high-grade serous carcinoma development. *The Journal of Pathology*, *233*(3), 228–237. http://doi.org/10.1002/path.4353
Siegel, R. L., Miller, K. D., & Jemal, A. (2020). Cancer statistics, 2020. *CA: a Cancer Journal for Clinicians*, *70*(1), 7–30. http://doi.org/10.3322/caac.21590
Srivastava, S., & Riddell, S. R. (2018). Chimeric Antigen Receptor T Cell Therapy: Challenges to Bench-to-Bedside Efficacy. *Journal of Immunology (Baltimore, Md. : 1950)*, *200*(2), 459–468. http://doi.org/10.4049/jimmunol.1701155
Strickland, K. C., Howitt, B. E., Shukla, S. A., Rodig, S., Ritterhouse, L. L., Liu, J. F., et al. (2016). Association and prognostic significance of BRCA1/2-mutation status with neoantigen load, number of tumor-infiltrating lymphocytes and expression of PD-1/PD-L1 in high grade serous ovarian cancer. *Oncotarget*, *7*(12), 13587–13598. http://doi.org/10.18632/oncotarget.7277
Szabova, L., Yin, C., Bupp, S., Guerin, T. M., Schlomer, J. J., Householder, D. B., et al. (2012). Perturbation of Rb, p53, and Brca1 or Brca2 Cooperate in Inducing Metastatic Serous Epithelial Ovarian Cancer. *Cancer Research*, *72*(16), 4141–4153. http://doi.org/10.1158/0008-5472.CAN-11-3834
Tasdemir, N., Banito, A., Roe, J. S., Alonso-Curbelo, D., Camiolo, M., Tschaharganeh, D. F., et al. (2016). BRD4 Connects Enhancer Remodeling to Senescence Immune Surveillance. *Cancer Discovery*, *6*(6), 612–629. http://doi.org/10.1158/2159-8290.CD-16-0217
Teng, K., Ford, M. J., Harwalkar, K., Li, Y., Pacis, A. S., Farnell, D., et al. (2021). Modeling High-grade serous ovarian carcinoma using a combination of in vivo fallopian tube electroporation and CRISPR-Cas9-mediated genome editing. *Cancer Research*. http://doi.org/10.1158/0008-5472.CAN-20-1518
Tran, L., Allen, C. T., Xiao, R., Moore, E., Davis, R., Park, S.-J., et al. (2017). Cisplatin Alters Antitumor Immunity and Synergizes with PD-1/PD-L1 Inhibition in Head and Neck Squamous Cell Carcinoma. *Cancer Immunology Research*, *5*(12), 1141–1151. http://doi.org/10.1158/2326-6066.CIR-17-0235
van Deursen, J. M. (2014). The role of senescent cells in ageing. *Nature*, *509*(7501), 439–446. http://doi.org/10.1038/nature13193

Van Keymeulen, A., Rocha, A. S., Ousset, M., Beck, B., Bouvencourt, G., Rock, J., et al. (2011). Distinct stem cells contribute to mammary gland development and maintenance. *Nature*, *479*(7372), 189–193. http://doi.org/10.1038/nature10573

Verhaak, R. G. W., Tamayo, P., Yang, J.-Y., Hubbard, D., Zhang, H., Creighton, C. J., et al. (2013). Prognostically relevant gene signatures of high-grade serous ovarian carcinoma. *The Journal of Clinical Investigation*, *123*(1), 517–525. http://doi.org/10.1172/JCI65833

Villablanca, E. J., Raccosta, L., Zhou, D., Fontana, R., Maggioni, D., Negro, A., et al. (2009). Tumor-mediated liver X receptor-α activation inhibits CC chemokine receptor-7 expression on dendritic cells and dampens antitumor responses. *Nature Medicine*, 1–9. http://doi.org/10.1038/nm.2074

Walton, J., Blagih, J., Ennis, D., Leung, E., Dowson, S., Farquharson, M., et al. (2016). CRISPR/Cas9-Mediated Trp53 and Brca2 Knockout to Generate Improved Murine Models of Ovarian High-Grade Serous Carcinoma. *Cancer Research*, *76*(20), 6118–6129. http://doi.org/10.1158/0008-5472.CAN-16-1272

Wang, L., Madigan, M. C., Chen, H., Liu, F., Patterson, K. I., Beretov, J., et al. (2009). Expression of urokinase plasminogen activator and its receptor in advanced epithelial ovarian cancer patients. *Gynecologic Oncology*, *114*(2), 265–272. http://doi.org/10.1016/j.ygyno.2009.04.031

Wang, L., Yang, R., Zhao, L., Zhang, X., Xu, T., & Cui, M. (2019). Basing on uPAR-binding fragment to design chimeric antigen receptors triggers antitumor efficacy against uPAR expressing ovarian cancer cells. *Biomedicine & Pharmacotherapy*, *117*, 109173. http://doi.org/10.1016/j.biopha.2019.109173

Wang, Y. K., Bashashati, A., Anglesio, M. S., Cochrane, D. R., Grewal, D. S., Ha, G., et al. (2017). Genomic consequences of aberrant DNA repair mechanisms stratify ovarian cancer histotypes. *Nature Genetics*, *49*(6), 856–865. http://doi.org/10.1038/ng.3849

Wellenstein, M. D., & de Visser, K. E. (2018). Cancer-Cell-Intrinsic Mechanisms Shaping the Tumor Immune Landscape. *Immunity*, *48*(3), 399–416. http://doi.org/10.1016/j.immuni.2018.03.004

Wieser, V., Gaugg, I., Fleischer, M., Shivalingaiah, G., Wenzel, S., Sprung, S., et al. (2018). BRCA1/2 and TP53 mutation status associates with PD-1 and PD-L1 expression in ovarian cancer. *Oncotarget*, *9*(25), 17501–17511. http://doi.org/10.18632/oncotarget.24770

Wolchok, J. D., Chiarion-Sileni, V., Gonzalez, R., Rutkowski, P., Grob, J.-J., Cowey, C. L., et al. (2017). Overall Survival with Combined Nivolumab and Ipilimumab in Advanced Melanoma. *New England Journal of Medicine*, *377*(14), 1345–1356. http://doi.org/10.1056/NEJMoa1709684

Wolchok, J. D., Kluger, H., Callahan, M. K., Postow, M. A., Rizvi, N. A., Lesokhin, A. M., et al. (2013). Nivolumab plus ipilimumab in advanced melanoma. *New England Journal of Medicine*, *369*(2), 122–133. http://doi.org/10.1056/NEJMoa1302369

Wu, J., & Chen, Z. J. (2014). Innate immune sensing and signaling of cytosolic nucleic acids. *Annual Review of Immunology*, *32*, 461–488. http://doi.org/10.1146/annurev-immunol-032713-120156

Wyld, L., Bellantuono, I., Tchkonia, T., Morgan, J., Turner, O., Foss, F., et al. (2020). Senescence and Cancer: A Review of Clinical Implications of Senescence and Senotherapies. *Cancers*, *12*(8), 2134. http://doi.org/10.3390/cancers12082134

Xing, D., & Orsulic, S. (2006). A mouse model for the molecular characterization of brca1-associated ovarian carcinoma. *Cancer Research*, *66*(18), 8949–8953. http://doi.org/10.1158/0008-5472.CAN-06-1495

Xu, F., Wang, Z., Zhang, H., Chen, J., Wang, X., Cui, L., et al. (2021a). Mevalonate Blockade in Cancer Cells Triggers CLEC9A+ Dendritic Cell-Mediated Antitumor Immunity. *Cancer Research*, *81*(17), 4514–4528. http://doi.org/10.1158/0008-5472.CAN-20-3977

Xu, S., Chaudhary, O., Rodríguez-Morales, P., Sun, X., Chen, D., Zappasodi, R., et al. (2021b). Uptake of oxidized lipids by the scavenger receptor CD36 promotes lipid peroxidation and dysfunction in CD8+ T cells in tumors. *Immunity*, *54*(7), 1561–1577.e7. http://doi.org/10.1016/j.immuni.2021.05.003

Xue, W., Zender, L., Miething, C., Dickins, R. A., Hernando, E., Krizhanovsky, V., et al. (2007). Senescence and tumour clearance is triggered by p53 restoration in murine liver carcinomas. *Nature*, *445*(7128), 656–660. http://doi.org/10.1038/nature05529

Yang, H., Wang, H., Ren, J., Chen, Q., & Chen, Z. J. (2017a). cGAS is essential for cellular senescence. *Proceedings of the National Academy of Sciences*, *114*(23), E4612–E4620. http://doi.org/10.1073/pnas.1705499114

Yang, L., Fang, J., & Chen, J. (2017b). Tumor cell senescence response produces aggressive variants. *Cell Death Discovery*, *3*, 17049. http://doi.org/10.1038/cddiscovery.2017.49

Yang, X., Shen, F., Hu, W., Coleman, R. L., & Sood, A. K. (2015). New ways to successfully target tumor vasculature in ovarian cancer. *Current Opinion in Obstetrics & Gynecology*, *27*(1), 58–65. http://doi.org/10.1097/GCO.0000000000000136

Zhai, Y., Wu, R., Kuick, R., Sessine, M. S., Schulman, S., Green, M., et al. (2017). High-grade serous carcinomas arise in the mouse oviduct via defects linked to the human disease. *The Journal of Pathology*, *243*(1), 16–25. http://doi.org/10.1002/path.4927

Zhang, Lin, Conejo-Garcia, J. R., Katsaros, D., Gimotty, P. A., Massobrio, M., Regnani, G., et al. (2003). Intratumoral T Cells, Recurrence, and Survival in Epithelial Ovarian Cancer. *New England Journal of Medicine*, *348*(3), 203–213. http://doi.org/10.1056/NEJMoa020177

Zhang, Shiyu, Royer, R., Li, S., McLaughlin, J. R., Rosen, B., Risch, H. A., et al. (2011). Frequencies of BRCA1 and BRCA2 mutations among 1,342 unselected patients with invasive ovarian cancer. *Gynecologic Oncology*, *121*(2), 353–357. http://doi.org/10.1016/j.ygyno.2011.01.020

Zhang, Shuang, Dolgalev, I., Zhang, T., Ran, H., Levine, D. A., & Neel, B. G. (2019). Both fallopian tube and ovarian surface epithelium are cells-of-origin for high-grade serous ovarian carcinoma. *Nature Communications*, *10*(1), 1–16. http://doi.org/10.1038/s41467-019-13116-2

Zhang, Shuang, Iyer, S., Ran, H., Dolgalev, I., Gu, S., wei, W., et al. (2020). Genetically Defined, Syngeneic Organoid Platform for Developing Combination Therapies for Ovarian Cancer. *Cancer Discovery*, CD–20–0455–46. http://doi.org/10.1158/2159-8290.CD-20-0455

Zsiros, E., Tanyi, J., Balint, K., & Kandalaft, L. E. (2014). Immunotherapy for ovarian cancer: recent advances and perspectives. *Current Opinion in Oncology*, *26*(5), 492–500. http://doi.org/10.1097/CCO.0000000000000111

PUBLICATION

Parts of the work presented here are based on the attached publication published in Proceedings of the National Academy of Sciences of the United States of America (PNAS) on January 26, 2022.

Senescence induction dictates response to chemo- and immunotherapy in preclinical models of ovarian cancer

Stella V. Paffenholz[a,b], Camilla Salvagno[c,d], Yu-Jui Ho[a], Matthew Limjoco[a], Timour Baslan[a], Sha Tian[a], Amanda Kulick[e], Elisa de Stanchina[e], John E. Wilkinson[f], Francisco M. Barriga[a], Dmitriy Zamarin[g], Juan R. Cubillos-Ruiz[c,d,h], Josef Leibold[a,i,j,1], and Scott W. Lowe[a,k,1]

[a]Cancer Biology and Genetics Program, Sloan Kettering Institute, Memorial Sloan Kettering Cancer Center, New York, NY 10065; [b]Louis V. Gerstner Jr. Graduate School of Biomedical Sciences, Memorial Sloan Kettering Cancer Center, New York, NY 10065; [c]Department of Obstetrics and Gynecology, Weill Cornell Medicine, New York, NY 10065; [d]Sandra and Edward Meyer Cancer Center, Weill Cornell Medicine, New York, NY 10065; [e]Department of Molecular Pharmacology, Memorial Sloan Kettering Cancer Center, New York, NY 10065; [f]Department of Pathology, University of Michigan School of Medicine, Ann Arbor, MI 48109; [g]Department of Medicine, Gynecologic Medical Oncology Service, Memorial Sloan Kettering Cancer Center, New York, NY 10065; [h]Weill Cornell Graduate School of Biomedical Sciences, Cornell University, New York, NY 10065; [i]Department of Medical Oncology & Pneumology (Internal Medicine VIII), University Hospital Tuebingen, Tuebingen 72076, Germany; [j]DFG Cluster of Excellence 2180 "Image-Guided and Functional Instructed Tumor Therapy" (iFIT), University of Tuebingen, 72076 Tuebingen, Germany; and [k]Howard Hughes Medical Institute (HHMI), Memorial Sloan Kettering Cancer Center, New York, NY 10065

Contributed by Scott W. Lowe; received October 1, 2021; accepted November 22, 2021; reviewed by Tak Mak and Sandra Orsulic

High-grade serous ovarian carcinoma (HGSOC) is a cancer with dismal prognosis due to the limited effectiveness of existing chemo- and immunotherapies. To elucidate mechanisms mediating sensitivity or resistance to these therapies, we developed a fast and flexible autochthonous mouse model based on somatic introduction of HGSOC-associated genetic alterations into the ovary of immunocompetent mice using tissue electroporation. Tumors arising in these mice recapitulate the metastatic patterns and histological, molecular, and treatment response features of the human disease. By leveraging these models, we show that the ability to undergo senescence underlies the clinically observed increase in sensitivity of homologous recombination (HR)–deficient HGSOC tumors to platinum-based chemotherapy. Further, cGas/STING-mediated activation of a restricted senescence-associated secretory phenotype (SASP) was sufficient to induce immune infiltration and sensitize HR-deficient tumors to immune checkpoint blockade. In sum, our study identifies senescence propensity as a predictor of therapy response and defines a limited SASP profile that appears sufficient to confer added vulnerability to concurrent immunotherapy and, more broadly, provides a blueprint for the implementation of electroporation-based mouse models to reveal mechanisms of oncogenesis and therapy response in HGSOC.

mouse models | ovarian cancer | cancer immunotherapy | senescence

Over 70% of women diagnosed with high-grade serous ovarian carcinoma (HGSOC) succumb to their disease, making it the deadliest gynecological cancer (1). The standard of care for most patients consists of surgical debulking and platinum/taxane-based chemotherapy, though responses are typically transient, and resistance invariably emerges. Despite recent advances in targeted therapies such as poly (adenosine diphosphate [ADP]-ribose) polymerase (PARP) inhibitors and antiangiogenic therapies, survival has only marginally improved in the past 30 y (1). Moreover, immune checkpoint blockade (ICB), which has revolutionized the treatment of several cancer types (2–4), shows only modest results in HGSOC (5–7). Yet, little is known about molecular mechanisms that dictate response or resistance to any of these modalities.

HGSOC can be divided into specific subtypes that exhibit distinct clinical behaviors (8). The disease is characterized by an almost universal appearance of *TP53* mutations and an unusually high rate of copy number alterations (CNAs) (9) that target a range of known oncogenic events such as gains of the oncogene *MYC*. Moreover, tumors also harbor inactivating mutations in genes important for homologous recombination (HR) DNA repair, most commonly in *BRCA1* and *BRCA2* (9), which display an even greater degree of genomic rearrangements than HR-proficient tumors (10). HR deficiency sensitizes ovarian tumors to platinum-based therapies and PARP inhibitors (11) and, in other cancers, appears to sensitize tumors to

Significance

Efforts to understand and find new treatment options for high-grade serous ovarian cancer (HGSOC) have been confounded by a paucity of immune-competent models that accurately reflect the genetics and biology of the disease. Here, we leverage somatic tissue engineering to develop a fast and flexible immune-competent mouse model of HGSOC and reveal mechanistic insights into factors that dictate the response of ovarian tumors to conventional chemotherapy and immune checkpoint blockade. Our results identify a genotype-dependent therapy-induced senescence program that mediates sensitivity and resistance to first line chemotherapy and point to strategies to harness the senescence program to sensitize ovarian tumors to immune checkpoint blockade.

Author contributions: S.V.P., C.S., E.d.S., F.M.B., D.Z., J.R.C.-R., J.L., and S.W.L. designed research; S.V.P., C.S., S.T., A.K., J.E.W., and J.L. performed research; S.V.P., Y.-J.H., M.L., and T.B. analyzed data; and S.V.P., J.L., and S.W.L. wrote the paper.

Reviewers: T.M., Princess Margaret Cancer Centre; and S.O., University of California, Los Angeles.

Competing interest statement: T.B. holds equity in Roche, Genenetech, and Novartis and has received consulting fees from Illumina, Oxford Nanopore, and Pacific Biosciences. D.Z. reports research funding to Memorial Sloan Kettering Cancer Center from AstraZeneca, Genentech, and Plexxikon; personal fees from Synlogic Therapeutics, Hookipa Biotech, Agenus, Synthekine, Memgen, Mana Therapeutics, Tessa Therapeutics, and Xencor; stock options from Accurius, Calidi Biotherapeutics, and ImmunOs, and is an inventor on a patent concerning the use of Newcastle disease virus as a cancer therapeutic, licensed to Merck. J.R.C.-R. is a member of the scientific advisory board of NextRNA Therapeutics, Inc. S.W.L. is a founder and member of the scientific advisory board of Blueprint Medicines, Mirimus, Inc., ORIC Pharmaceuticals, Geras Bio, and Faeth Therapeutics, and is on the scientific advisory board of PMV Pharmaceuticals. None of these affiliations represent a conflict of interest with respect to the design or execution of this study or interpretation of data presented in this report.

[1]To whom correspondence may be addressed. Email: lowes@mskcc.org or Josef.Leibold@med.uni-tuebingen.de.

This article contains supporting information online at http://www.pnas.org/lookup/suppl/doi:10.1073/pnas.2117754119/-/DCSupplemental.

Published January 26, 2022.

immune-modulating agents, but it is unclear to what extent this process plays a role in HGSOC (12, 13). Clearly, a better understanding of the biological and molecular mechanisms responsible for genotype-response patterns would enable existing therapies to be used more effectively and facilitate development of novel strategies to overcome resistance.

Relating clinical observations to mechanisms requires the availability of accurate model systems. However, until recently, models that faithfully recapitulate the heterogeneity of human HGSOC have been limited. Genetically engineered mouse models (GEMMs), which are generated by intercrossing a series of tissue-specific and/or conditional alleles and result in production of autochthonous tumors, have helped elucidate the consequences of cancer-associated mutations on HGSOC tumorigenesis (14). While such autochthonous models are powerful, they are time consuming, expensive, and the specific requirement for female mice leads to substantial animal waste. Consequently, it is impractical to develop animal cohorts of sufficient size and genotypic diversity for rapid and rigorous mechanistic and preclinical studies. Recently, both patient and murine HGSOC organoid models covering a range of genomic configurations have been developed, which enable perturbations in vitro or following orthotopic transplantation in vivo (15–19). However, these systems also have limitations: the human models cannot be studied in the presence of the intact immune system and the murine models that employ in vitro transformed cells do not undergo immunoediting and lack other microenvironmental factors that shape tumor development in vivo (20, 21).

Considering the need for more accurate and facile autochthonous models, we combined CRISPR genome engineering approaches with transposon/transposase-based systems and in vivo organ electroporation (EPO-GEMM) to model HGSOC in mice. The EPO-GEMM approach allows the study of autochthonous tumors in an immune-competent background while overcoming the logistical disadvantages of traditional GEMMs. Using this approach, we developed genetically and histopathologically accurate models of HGSOC and use them to gain mechanistic insights into genotype-dependent therapy responses to chemo- and immunotherapies.

Results

Somatic Introduction of Oncogenic Lesions Generates High-Grade Serous Ovarian Carcinoma. To develop murine genotypically diverse models of HGSOC, we optimized methods to introduce genetic elements into the ovary by direct tissue electroporation. Briefly, the ovary is surgically exposed and injected with plasmid DNA encoding CRISPR-Cas9 constructs and/or a transposon vector and a Sleeping Beauty transposase, followed by electroporation of the surrounding ovarian and fallopian tube tissue (Fig. 1*A*). Since more than 95% of HGSOC patients harbor tumors with mutations in the *TP53* tumor suppressor gene (9), all genotypic configurations included vectors coexpressing Cas9 and a single-guide RNA (sgRNA) targeting *Trp53* that was previously validated in vivo (22). In addition, various combinations of oncogene-expressing transposon vectors or sgRNAs targeting additional tumor suppressor genes that co-occur in human patients were included (Fig. 1*B*). Following electroporation, mice were monitored for tumor onset and progression by ultrasound imaging and abdominal palpation. To determine the extent to which our model recapitulates human HGSOC, murine tumor material was analyzed histologically for clinically relevant HGSOC biomarkers and molecularly for CRISPR-Cas9–engineered somatic mutations, acquired CNAs, and transcriptional profiles.

Disruption of *Trp53* alone did not produce tumors over the time course of these experiments. Focal tumors arose following electroporation of sgRNAs targeting *Trp53* and *Pten*, or *Trp53*, *Pten*, and *Rb1* with 40% and 90% penetrance, respectively, with the latter configuration displaying a median survival of 214 d. Traditional GEMMs with analogous genetic configurations develop tumors with similar penetrance and latency (23–26). Since *MYC* gain or amplification often co-occurs with *TP53* mutations in human HGSOC and can be oncogenic in transplantation models (27, 28), we also combined *Trp53* sgRNAs together with a transposon vector overexpressing *MYC*. The combination of *MYC* overexpression with CRISPR-Cas9–induced loss of *Trp53* was particularly potent to produce tumors in 100% of the recipients and vastly accelerate the disease (Fig. 1*C*, median survival 61 d).

Most mice developed metastatic disease to the omentum and peritoneum, which are the most common sites of metastatic spread in patients (29). While tumors arising through the disruption of tumor suppressors only generated micrometastatic nodules in the omentum (Fig. 1*D*), the addition of *MYC* resulted in macrometastatic disease and ascites formation (Fig. 1*E*). As occurs in human HGSOC tumors (30), EPO-GEMM tumors exhibited a solid architecture with some glandular areas, necrosis in solid areas, large hyperchromatic nuclei, and abundant, often atypical, mitotic figures (Fig. 1 *D* and *E*). Histologically, we never observed sarcomas or lymphomas arising in electroporated animals and, accordingly, all tumors analyzed expressed molecular hallmarks of human HGSOC, including Cytokeratin-7 (CK7), Wilms Tumor 1 (WT1), Cancer Antigen 125 (CA-125), Paired box 8 (Pax-8), and high Ki67 (Fig. 1*F* and *SI Appendix*, Fig. S1*A*). These markers were retained in metastases (*SI Appendix*, Fig. S1*B*), with the exception of CK7 whose reduced expression at metastatic sites correlates with poor prognosis in patients (31). As expected, *MYC*-driven tumors showed high levels of MYC protein expression (Fig. 1*F*).

At the molecular level, Sanger sequencing analysis of the resulting tumors at terminal stage confirmed the presence of insertion and deletion mutations (indels) at the *Trp53*, *Pten*, and *Rb1* loci, consistent with their disruption through CRISPR-Cas9 (*SI Appendix*, Fig. S1*C*). Deep sequencing of the CRISPR-Cas9–induced *Trp53* scar revealed that tumors were oligoclonal and that the dominant clones were shared between ovarian tumors and paired omentum metastases, confirming that the disseminated cells arose from the primary tumor site (*SI Appendix*, Fig. S1*D*). Analysis of CNAs using sparse whole-genome sequencing (32) of primary EPO-GEMM tumors revealed widespread aneuploidies as occurs in human disease (33). Recurrent changes included loss of mouse chromosomes 10 and 12 and gains of chromosomes 1 and 2. As occurs in a traditional GEMM with *Brca1;Trp53;Rb1;Nf1* genotype (23), some tumors generated by tumor suppressor gene inactivation without *MYC* overexpression showed gain or amplification of the *Myc* locus on mouse chromosome 15 (*SI Appendix*, Fig. S1*E*) together with MYC protein expression (*SI Appendix*, Fig. S1*F*). These data underscore the importance of *MYC* in driving HGSOC and support the rationale for using *MYC* as a driver in our EPO-GEMM platform.

Analysis of RNA-sequencing (RNA-seq) data derived from tumors demonstrated that the *MYC;Trp53* (MP) EPO-GEMM system faithfully recapitulates the transcriptional states characteristic of human disease (Fig. 1*G*). When compared to normal tissue, the top up-regulated pathways in both the Hallmark and Kyoto Encyclopedia of Genes and Genomes (KEGG) databases were related to proliferation (Hallmark: E2F targets, MYC targets, and G2M checkpoint; KEGG: ribosome, spliceosome, and oxidative phosphorylation) and DNA repair (Hallmark: DNA repair; KEGG: base excision repair) and the top down-regulated pathways were related to an active immune response (Hallmark: TNFa signaling via NF-κB and inflammatory response; KEGG: neuroactive ligand receptor interaction

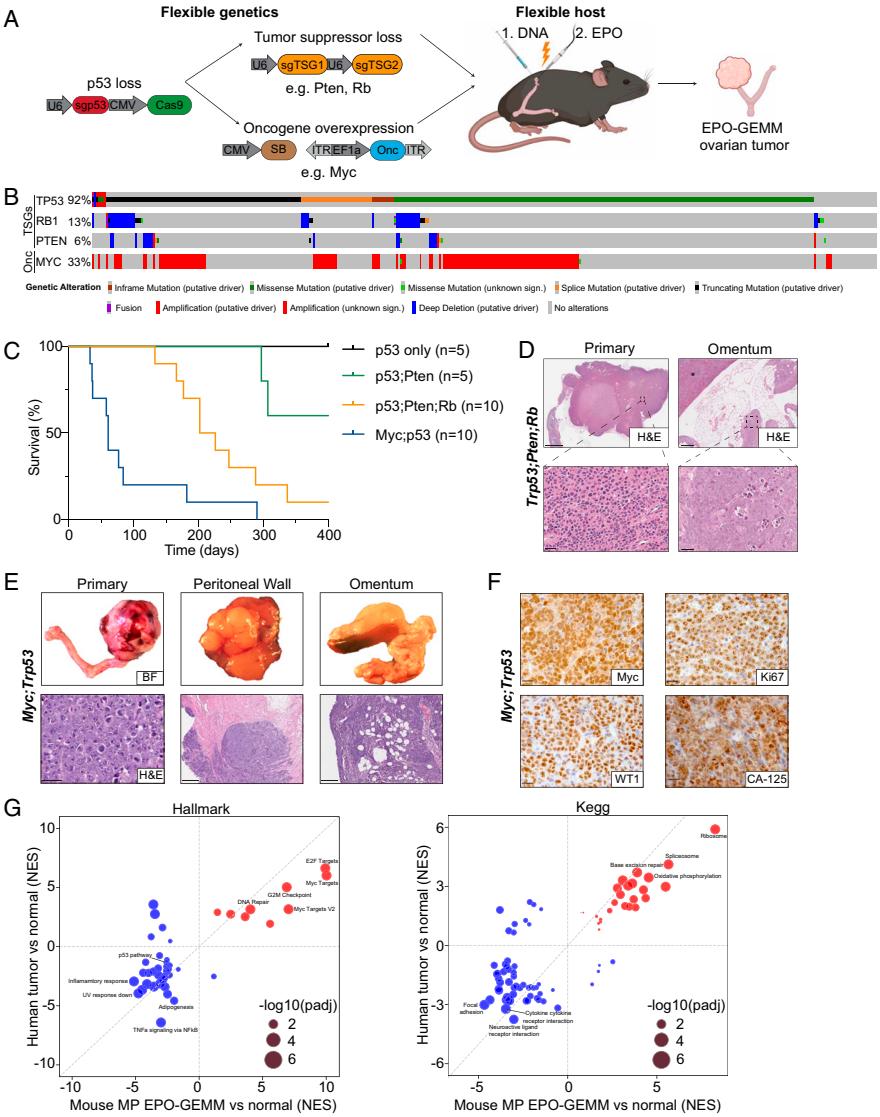

Fig. 1. Somatic introduction of oncogenic lesions generates high-grade serous ovarian carcinoma. (*A*) Schematic of the EPO-GEMM approach to generate ovarian cancer. A CRISPR-Cas9 vector targeting *Trp53* is codelivered with additional sgRNAs targeting tumor suppressor genes (TSGs) or an oncogene (Onc) containing transposon vector in combination with a Sleeping Beauty (SB) transposase into the ovary and fallopian tube by direct in vivo electroporation. (*B*) Oncoprint displaying the genomic status of *TP53*, *RB1*, *PTEN*, and *MYC* in HGSOC (The Cancer Genome Atlas [TCGA], Pan-cancer dataset). (*C*) Kaplan–Meier survival curve of C57BL/6 mice electroporated with the indicated combinations of plasmids. (*D*) Representative hematoxylin and eosin (H&E) staining of a Trp53;Pten;Rb EPO-GEMM primary tumor (*Left*) and omentum with a micrometastasis (*Right*). (Scale bar, 5 mm [*Top Left*], 200 μm [*Top Right*], 50 μm [*Bottom Left*], 25 μm [*Bottom Right*].) The spleen is labeled with an asterisk. (*E*) Macroscopic bright-field (BF) images (*Top*) and H&E sections (*Bottom*) of genital tracts, peritoneum, and omentum of a mouse bearing a MP EPO-GEMM tumor. (Scale bar, 50 μm [*Bottom Left*], 500 μm [*Bottom Middle* and *Right*].) (*F*) Representative immunohistochemical staining of a MP EPO-GEMM ovarian tumor for MYC, the proliferation marker Ki67, and the HGSOC markers Wilms Tumor 1 (WT1) and Cancer Antigen 125 (CA-125) in representative sections. (Scale bar, 20 μm.) (*G*) Correlation of gene set enrichment analysis normalized enrichment scores (NES) derived from RNA-seq data for Hallmark (*Left*) or KEGG (*Right*) pathways enriched in human ovarian cancer samples (*y* axis) and murine EPO-GEMM ovarian cancer (*x* axis) compared to normal tissue. Highlighted are key pathways; circle size represents the adjusted *P* value.

and cytokine receptor interaction). In line with the almost ubiquitous *TP53* inactivation in HGSOC, the p53 pathway was among the top down-regulated pathways in the Hallmark gene sets. These results validate the EPO-GEMM approach as a flexible platform to model HGSOC tumors of varying genotypes that resemble the metastatic, histological, genomic, and transcriptomic properties of the human disease.

The similarity of EPO-GEMM ovarian cancers to human HGSOC was striking, given that our electroporation method does not discriminate between cell types within the targeted tissue. To confirm that the tumors originated from epithelial cells, we harnessed the flexibility of the EPO-GEMM approach to directly mutagenize Cytokeratin-8 (CK8)-expressing epithelial cells, a cell type that can serve as a tumor-initiating cell in the absence of *Trp53* (34), and is also retained in traditional GEMMs arising in *Brca1;Trp53;Pten*-deficient mice (24). Double transgenic mice harboring a CRE-estrogen receptor fusion transgene (CreER) under the control of the CK8 promoter and a Lox-Stop-Lox (LSL) Cas9-IRES-GFP transgene were treated with tamoxifen and electroporated with vectors expressing a *MYC* transposon, a transposase, and a *Trp53* sgRNA. In this setting, only CK8-positive epithelial cells are capable of CRISPR-Cas9–mediated editing upon tamoxifen addition (*SI Appendix*, Fig. S1*G*). Tamoxifen treatment triggered expression of GFP in CK8-positive epithelial cells (*SI Appendix*, Fig. S1*H*) and led to the formation of GFP-positive ovarian tumors with similar histological and transcriptional features as observed in wild-type (WT) mice harboring tumors of the same genotype (*SI Appendix*, Fig. S1 *I*–*K*). These data confirm the epithelial origin of the EPO-GEMM tumors and imply that relevant epithelial populations in the ovary are most sensitive to the genetic alterations that co-occur in the human disease.

HR-Deficient Tumors Have Unique Genomic, Immune, and Therapy Response Features. More than one-third of ovarian cancer patients are classified as HR deficient (9). To model tumors arising in this important tumor subtype, we incorporated sgRNAs targeting *Brca1* into the MP combination described above using a vector that coexpresses *Trp53* and *Brca1* sgRNAs (*MYC;Trp53;Brca1*, MPB1) (*SI Appendix*, Fig. S2*A*). The resulting tumors displayed an onset and histology that was similar to those harboring *MYC* and *Trp53* alterations alone (*SI Appendix*, Fig. S2 *B* and *C*). Despite similar latencies, tumors produced with a plasmid mixture including the *Brca1* sgRNA invariably displayed indels at the *Brca1* sgRNA target site (*SI Appendix*, Fig. S2*D*), implying that *Brca1* inactivation produced a selective advantage during tumorigenesis. Accordingly, as is characteristic of HR-deficient cells (18), MPB1 tumor cells isolated from EPO-GEMM tumors showed reduced induction of Rad51-containing nuclear foci following irradiation compared to MP tumor cells with intact *Brca1* (Fig. 2*A*).

Compared to HR-proficient tumors, HR-deficient human ovarian cancers acquire even more genomic rearrangements (10), display substantial T cell infiltration (35–37), and are more responsive to platinum-based chemotherapy (38, 39). Similarly, murine MPB1 ovarian EPO-GEMM tumors harbored more CNAs (Fig. 2*B*) and a greater proportion of $CD4^+$ and $CD8^+$ T cells expressing both activation and exhaustion markers relative

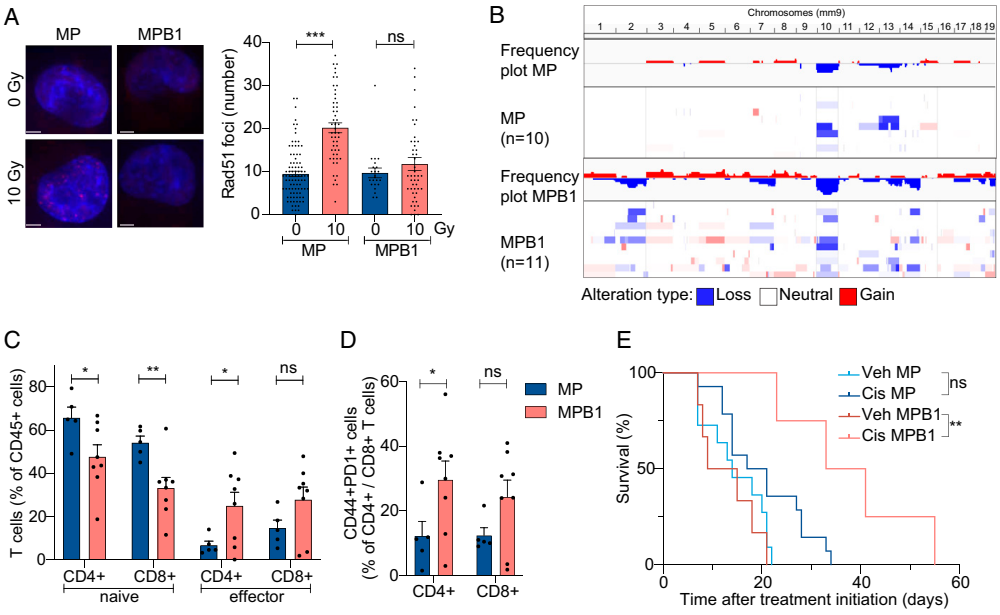

Fig. 2. HR-deficient tumors have unique genomic, immune, and therapy response features. (*A*) Representative images showing IF staining of RAD51 (*Left*) and the quantification of the number of RAD51 foci per nuclei (*Right*). Cell nuclei were stained with DAPI (blue). (Scale bar, 5 μm.) (*B*) Frequency plot of CNA analysis of MP ($n = 10$) and MPB1 ($n = 11$) EPO-GEMM ovarian tumors. (*C* and *D*) Immune cell analysis by flow cytometric analysis of representative EPO-GEMM tumors of the indicated genotypes ($n = 5$ to 8 mice per group). (*E*) Kaplan–Meier survival curve of C57BL/6 mice electroporated with the indicated combinations of plasmids and treated with vehicle (veh) or cisplatin (cis). Treatment was initiated after tumors were palpable ($n = 4$ to 13 mice per group). $^*P \le 0.05$, $^{**}P \le 0.01$, $^{***}P \le 0.001$, ns: not significant; mean ± SEM; analyses performed using unpaired *t* test (*A*, *C*, and *D*) and log-rank test (*E*).

to *Brca1*-proficient counterparts (Fig. 2 *C* and *D* and *SI Appendix*, Fig. S2*E*). Furthermore, mice harboring primary MPB1 tumors showed significantly improved survival following cisplatin therapy (Fig. 2*E*), a result that was recapitulated in mice following subcutaneous or intraperitoneal (i.p.) injection of primary EPO-GEMM tumor-derived cell lines (*SI Appendix*, Fig. S2 *F*–*H*). Therefore, MPB1 EPO-GEMM tumors recapitulate key biological and clinical features of human HR-deficient tumors.

Cisplatin Treatment Preferentially Induces Tumor Cell Senescence and Alters Immune Infiltrates in HR-Deficient HGSOC. As a first step toward assessing mechanisms leading to genotypic differences in intrinsic cisplatin sensitivity, we analyzed the biological responses to cisplatin treatment. Cultured cells established from MP and MPB1 tumors showed similar levels of growth inhibition and apoptosis induction following cisplatin treatment in vitro (*SI Appendix*, Fig. S3 *A* and *B*) and in vivo (*SI Appendix*, Fig. S3*C*). In contrast, *Brca1*-deficient cells showed a much greater proclivity for senescence, displaying an increase in senescence-associated β-galactosidase (SA-β-gal) activity and a decrease in colony-forming potential following cisplatin treatment compared to the *Brca1*-proficient MP counterparts (*SI Appendix*, Fig. S3 *D* and *E*). Similar results were observed in vivo, with MPB1-derived tumors showing more SA-β-gal activity as measured by the fluorogenic substrate C12RG (40), reduced phosphorylated Rb, and a concomitant decrease in

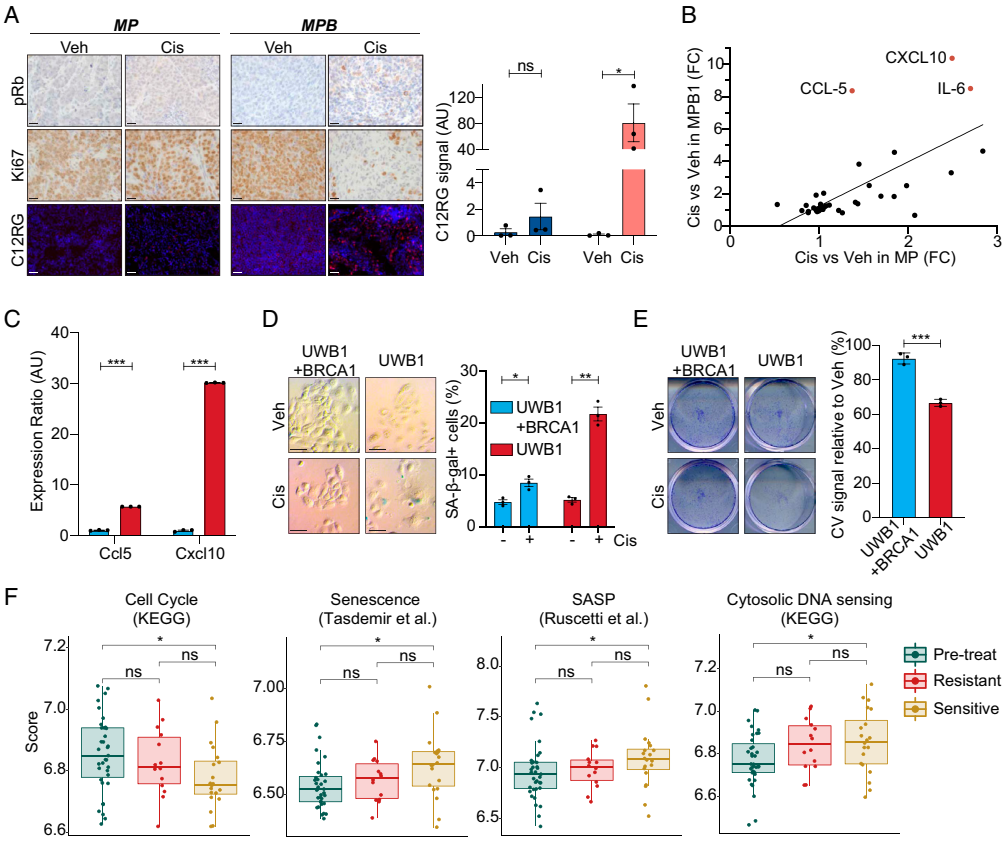

Fig. 3. Cisplatin treatment preferentially induces tumor cell senescence and alters immune infiltrates in HR-deficient HGSOC. (*A*) Immunohistochemical staining of phospho-Rb (pRb) and Ki67 and staining of C12RG, a fluorogenic substrate for SA-β-gal activity, of subcutaneously transplanted tumors treated with vehicle or cisplatin. (Scale bar, 20 μm.) Quantification of SA-β-gal activity is shown on the *Right* ($n = 3$). (*B*) Cytokine expression in MP (*x* axis) or MPB1 (*y* axis) cell lines treated with cisplatin relative to vehicle ($n = 2$ independent cell lines per genotype). (*C*) RT-qPCR analysis of *Ccl5* and *Cxcl10* in cisplatin-treated *BRCA1*-proficient (UWB1 + BRCA1) or -deficient (UWB1) human ovarian cancer cells ($n = 3$ technical replicates). (*D*) SA-β-gal staining (*Left*) and quantification (*Right*) of either *BRCA1*-proficient (UWB1 + BRCA1) or -deficient (UWB1) human ovarian cancer cell lines after treatment with vehicle or 100 nM cisplatin for 6 d ($n = 3$). (Scale bar, 50 μm.) (*E*) Clonogenic crystal violet (CV) assay of human ovarian cancer cells replated in the absence of drugs after 6-d pretreatment as in *D* ($n = 3$). (*F*) Expression of senescence and SASP signatures in patient samples isolated pretreatment and after three cycles of chemotherapy during the Cambridge Translational Cancer Research Ovarian Study 01 (CTCR-OV01) clinical trial (49, 50) (GSE15622). Posttreatment samples are subdivided into resistant and sensitive cases. $*P \leq 0.05$, $**P \leq 0.01$, $***P \leq 0.001$, ns: not significant; mean ± SEM; analyses performed using unpaired *t* test (*A* and *C*–*E*) and Wilcoxon signed-rank test (*F*).

Ki67 staining compared to MP controls after short-term cisplatin treatment (Fig. 3*A*). Apparently, *Brca1* mutations sensitize ovarian tumor cells to cisplatin-induced senescence.

Senescence is a potent tumor suppressive mechanism that involves a stable proliferative arrest coupled to a secretory program known as the senescence-associated secretory phenotype (SASP) (41). The SASP alters the tumor microenvironment (TME), where it can modulate extracellular matrix, tumor vasculature, and the functionality of immune cells (42, 43) that, in some instances, produces an inflammatory TME (44, 45). To examine SASP in our system, we performed cytokine array analysis on a series of cisplatin-treated MP and MPB1 cell lines. Out of the 44 factors assessed in this panel, *Ccl5*, *Cxcl10*, and *Il6* were the most significantly increased in the *Brca1*-deficient cells (Fig. 3*B*) and this correlated with increased mRNA expression in several MPB1 cell lines (*SI Appendix*, Fig. S3*F*) and in an isogenic setting in which *Brca1* was disrupted in MP tumor cells following in vitro establishment (*SI Appendix*, Fig. S3*G*). Taxol, another frontline chemotherapy used for HGSOC treatment, also induced a similar cytokine profile in MPB1 tumor cells (*SI Appendix*, Fig. S3*H*). Interestingly, the SASP profile detected in MPB1 cells following chemotherapy treatment was more restricted than has been observed in other contexts (44, 45), showing predominant secretion of immune modulatory cytokines and no endothelial cell regulatory factors. Accordingly, we did not detect obvious changes in tumor vasculature as assessed by CD31 immunofluorescence (IF) following cisplatin treatment (*SI Appendix*, Fig. S3*I*).

We also examined cisplatin responses in human cancer cells and patients. We analyzed the *BRCA1*-mutant UWB1.289 cell line along with its isogenic counterpart with forced expression of the *BRCA1* WT gene (46). Cisplatin treatment led to induction of *CCL-5* and *CXCL-10* in the *BRCA1*-mutant cells, which was dampened by forced expression of *BRCA1*-WT (Fig. 3*C*). The *BRCA1*-mutant cells showed a more pronounced senescence response, as evaluated by increased SA-β-gal activity and a decreased colony-forming potential following cisplatin treatment (Fig. 3 *D* and *E*). Additionally, a well-characterized *BRCA1*-deficient breast cancer cell line (47) was also more prone to cisplatin-induced senescence than a *BRCA1*-proficient counterpart (*SI Appendix*, Fig. S3 *J* and *K*). In patients, a retrospective analysis of RNA-seq data from matched pre- and posttreatment samples (48) showed an enrichment for gene signatures linked to senescence and SASP posttherapy (*SI Appendix*, Fig. S3*L*) with *CCL-5* and *IL-6* being among the most enriched genes in these signatures. Furthermore, in a dataset where outcomes were known (49, 50) (GSE15622), expression of senescence signatures was higher in the sensitive tumors (Fig. 3*F*). We also observed higher expression of transcripts linked to the cytosolic DNA-sensing pathway in sensitive tumors, which has previously been associated with senescence (51). While this dataset did not allow for classification of patients based on BRCA or HR status, it is consistent with the notion that senescence induction improves outcomes in HGSOC patients. Thus, *Brca1* loss is sufficient to predispose ovarian cancer cells to induction of a chemotherapy-induced senescence program that appears associated with improved outcomes in patients.

Cisplatin Treatment Leads to a cGas/STING-Dependent Infiltration of T and Natural Killer (NK) Cells in HR-Deficient Tumors. *Ccl5*, *Cxcl10*, and *Il6* are immune modulatory cytokines and members of the Interferon Stimulated Genes (ISG) family that act downstream of cGAS/STING signaling (52) and are often associated with the SASP (53, 54). cGAS is an intracellular innate immune sensor of cytosolic double-stranded DNA (55) that can be activated by nucleic acids present in micronuclei and can increase in cells with rampant genome instability (56). Breast and ovarian cancers harboring *BRCA* mutations have been shown to harbor high levels of micronuclei and cGas/STING activity (57, 58). In agreement, cultured MPB1 tumor cells displayed a trend toward more micronuclei than MP tumor cells, a difference that was exacerbated following cisplatin treatment (Fig. 4*A*). A similar increase was seen in DNA damage as evaluated by γH2AX staining (Fig. 4*B*). These effects correlated with a genotype-specific difference in immune infiltrates of transplanted tumors following cisplatin therapy. Specifically, MPB1 tumors showed a substantial increase in T and NK cells (Fig. 4 *C* and *D*) and a marked reduction of M2-like macrophages compared to MP controls (*SI Appendix*, Fig. S4 *A*–*C*).

To test whether the cGas/STING pathway contributed to the observed genotype-specific effects on drug responses, we generated two independent shRNAs capable of suppressing cGas expression (*SI Appendix*, Fig. S4*D*), transduced these into MPB1 tumor cells, and examined their impact on senescence and tumor phenotypes following cisplatin treatment. While cGAS suppression did not prevent drug-induced proliferative arrest or the appearance of senescence markers (*SI Appendix*, Fig. S4 *E*–*G*), it substantially reduced *Ccl5, Cxcl10,* and *Il6* expression (Fig. 4*E* and *SI Appendix*, Fig. S4*H*). In vivo, cGas/STING suppression blunted the therapy-induced accumulation of T and NK cells in transplanted MPB1 tumors (Fig. 4 *F* and *G*), while having no effect on myeloid cell infiltration (*SI Appendix*, Fig. S4 *I*–*K*). These data are consistent with a model whereby preferential induction of cisplatin-induced senescence in *Brca1*-deficient tumor cells contributes to cGas/STING activation and the establishment of a proinflammatory TME.

***Brca1* Loss Sensitizes Tumors to Chemo and ICB Combination Therapy.** Tumors displaying an inflamed microenvironment often up-regulate molecules that blunt antitumor immunity, a phenomenon that can also occur following cisplatin treatment (59, 60). Accordingly, cisplatin treatment induced cell surface expression of the immune checkpoint molecule PD-L1 on immune and tumor cells in MBP1 (but not MP) tumors (*SI Appendix*, Fig. S5 *A* and *B*). In patients and in a range of preclinical models, such a scenario often predicts increased tumor sensitivity to ICB (61). Accordingly, treatment outcomes were examined in MP or MPB1 EPO-GEMMs or mice harboring syngeneic subcutaneous or i.p. tumors generated by transplantation of EPO-GEMM–derived tumor cells. Of note, the i.p. context mimics the clinically relevant context of disseminated disease after surgical resection of the primary tumor.

In line with recent findings showing HGSOC patients receive little if any clinical benefit from ICB monotherapy (12), neither MP nor MPB1 tumors showed appreciable responses to anti–PD-1 therapy. In contrast, MPB1 tumors responded more effectively to cisplatin and anti–PD-1 combination therapy compared to MP tumors, in all three tumor settings (Fig. 5 *A* and *B* and *SI Appendix*, Fig. S5 *C*–*F*). This increased responsiveness was associated with an increase in the number of tumor-infiltrating $CD8^+$ T cells that expressed the activation marker Granzyme B (Fig. 5*C*). Interestingly, cGas suppression in *Brca1*-deficient tumors curtailed the responsiveness to combination therapy, but not single chemotherapy treatment, resulting in reduced clearance of senescent cells (Fig. 5 *D* and *E*). These data demonstrate that chemo- and immunotherapy uniquely synergize in *Brca1*-deficient EPO-GEMM tumors, whereas cGas/STING activation plays an important role in immune cell recruitment and clearance of senescent cells but is not necessarily required for primary chemotherapy response.

While many ovarian cancer patients initially respond to treatment, most patients eventually develop resistance. To study the process of disease relapse in previously responding tumors, we generated a cell line from a *Brca1*-mutant EPO-GEMM tumor that progressed following treatment with cisplatin and anti–PD-1 antibody and tested responsiveness to cisplatin

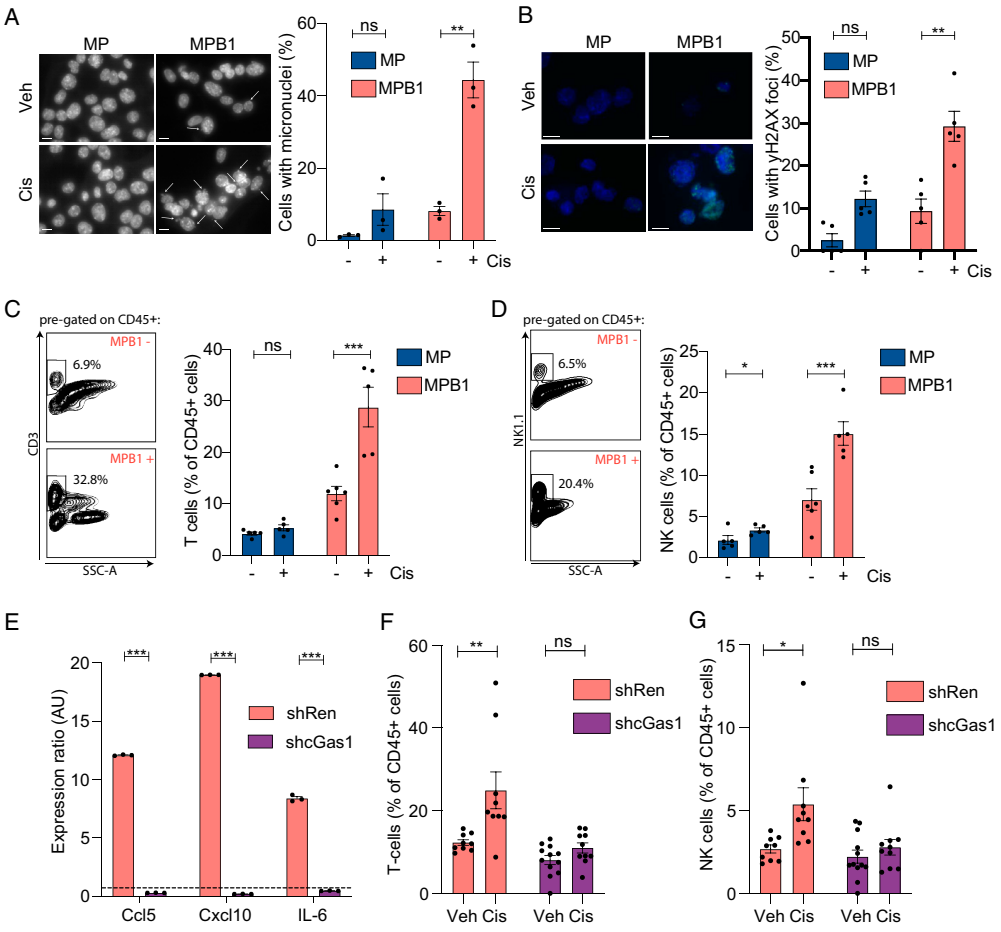

Fig. 4. Cisplatin treatment leads to a cGas/STING-dependent infiltration of T and NK cells in HR-deficient tumors. (*A*) Micronuclei staining of MP or MPB1 cell lines treated with cisplatin. Cell nuclei were stained with DAPI (gray) ($n = 3$ independent cell lines per genotype). (Scale bar, 20 μm.) (*B*) γH2AX staining (green) of MP or MPB1 cell lines treated with cisplatin. Cell nuclei were stained with DAPI (blue) ($n = 5$). (Scale bar, 20 μm.) (*C* and *D*) Representative flow cytometry plots (*Left*) and quantification (*Right*) of T cell (*C*) or NK cell (*D*) infiltration in subcutaneously transplanted ovarian tumors after treatment with two cycles of cisplatin ($n = 5$ to 6 mice per group). (*E*) RT-qPCR analysis of *Ccl5*, *Cxcl10*, and *Il6* in cell lines containing control Renilla (shRen) or cGas shRNAs (shcGas). Expression ratio of cisplatin treated relative to vehicle treated is shown ($n = 3$). (*F* and *G*) Flow cytometry analysis of T (*F*) and NK (*G*) cell infiltration in subcutaneously transplanted MPB1 ovarian tumors containing control Renilla or cGas shRNAs after treatment with two cycles of cisplatin ($n = 8$ to 12 mice per group). $^*P \leq 0.05$, $^{**}P \leq 0.01$, $^{***}P \leq 0.001$, ns: not significant; mean ± SEM; analyses performed using unpaired *t* test (*A*–*G*).

therapy in vitro and to cisplatin and anti–PD-1 combination therapy in vivo following subcutaneous injection into syngeneic recipients. Interestingly, tumors formed by these cells did not respond to the combination of cisplatin and ICB in vivo (Fig. 5*F*), an effect that correlated with a reduced propensity to undergo senescence (Fig. 5*G*) and induce SASP (Fig. 5*H*). While loss of 53BP1 can restore error-free DNA repair in *Brca1*-mutant cells (62), 53BP1 foci were still induced upon cisplatin treatment (*SI Appendix*, Fig. S5*G*) implying that this mechanism is not responsible for therapy resistance in our system. These data underscore the role of therapy-induced senescence as a mediator of response and resistance to platinum-based chemotherapy in HR-deficient ovarian cancer and its potential to sensitize these tumors to ICB.

Discussion

HGSOC is a genetically unique tumor type that almost uniformly develops resistance to conventional, targeted, and immune therapies. In this study, we produced a flexible nongermline-based mouse model that recapitulates the genetic, histological, and molecular features of human HGSOC. We illustrate its use for

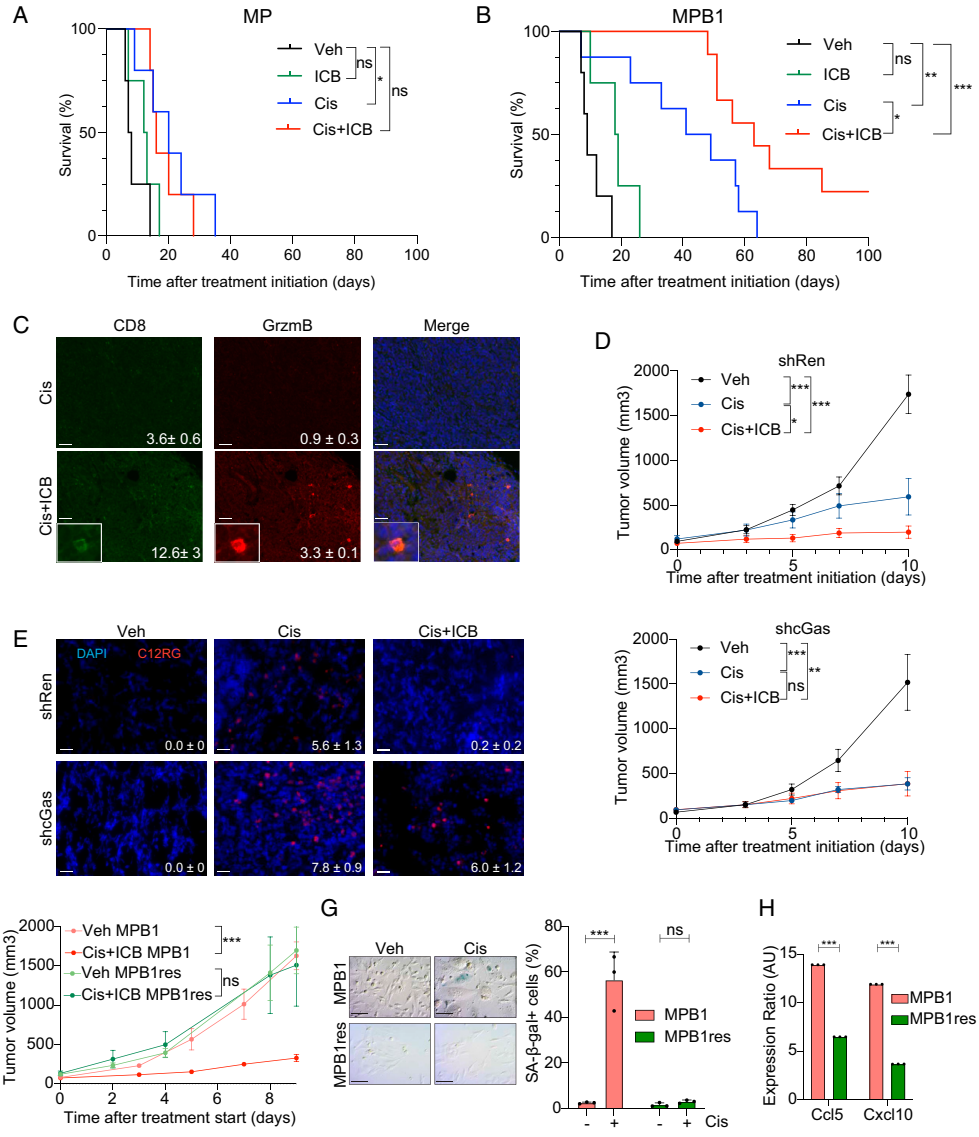

Fig. 5. *Brca1* loss sensitizes tumors to chemo and ICB combination therapy. (*A* and *B*) Kaplan–Meier survival curve of MP (*A*) or MPB1 (*B*) EPO-GEMM mice treated with the indicated drugs. Treatment was initiated after tumors were detected by abdominal palpation ($n = 4$ to 9 mice per group). (*C*) Representative IF staining and quantification (mean number of cells per field ± SEM, $P \leq 0.05$) of subcutaneously transplanted MPB1 ovarian tumors treated with indicated treatments ($n = 5$ fields for two independent tumors). (Scale bar, 20 μm.) (*D*) Tumor growth over time of transplanted MPB1 cell lines containing control Renilla (shRen, *Top*) or cGas shRNAs (shcGas, *Bottom*) with vehicle, cisplatin, or cisplatin + ICB ($n = 5$ to 6 mice per group). (*E*) Staining and quantification of C12RG, a fluorogenic substrate for SA-β-gal activity, in tumors treated as in *D* ($n = 3$). (Scale bar, 20 μm.) (*F*) Tumor growth of transplanted MPB1 or resistant MPB1 (MPB1_res) cell lines treated with vehicle or cisplatin + ICB ($n = 5$ to 6 mice per group). (*G*) SA-β-gal staining (*Left*) and quantification (*Right*) of MPB1 or MPB1_res cell lines treated with vehicle or cisplatin for 6 d ($n = 3$). (Scale bar, 50 μm.) (*H*) RT-qPCR analysis of *Ccl5* and *Cxcl10* in MPB1 or MPB1_res cell lines ($n = 3$ technical replicates). Expression ratio of cisplatin treated relative to vehicle treated is shown. $^*P \leq 0.05$, $^{**}P \leq 0.01$, $^{***}P \leq 0.001$, ns: not significant; mean ± SEM; analyses performed using log-rank test (*A* and *B*), unpaired *t* test (*C* and *E–H*), and one-way ANOVA (*D*).

studying genetic interactions during tumorigenesis and exploring molecular mechanisms that dictate treatment response. Our results add to previous work showing that HR defects can produce distinct tumor phenotypes and vulnerabilities (63, 64), and link a chemotherapy-induced senescence program to therapeutic outcome.

We believe that the EPO-GEMM approach described herein provides a platform that will revolutionize preclinical HGSOC research. While traditional germline models offer similar capabilities, they are simply too time consuming and asynchronous to be a workhorse system. By contrast, the EPO-GEMM approach enables the production of autochthonous tumors in immunocompetent mice that naturally disseminate, enabling the relatively synchronous production of cohorts of tumor-bearing mice simply from a set of plasmids and commercially available immunocompetent WT mice. While the use of lineage-specific Cas9 or CRE transgenes allows for the control of the cell of origin, electroporation of the ovary and fallopian tube of WT mice produces epithelial tumors that resemble human HGSOC, similar to what was observed in cell line studies (28). As such, the approach can be applied to any strain of recipient mice, enabling the study of the influence of host factors on tumor trajectories.

Our study is complementary to a recent report that also used tissue electroporation to generate immune-competent ovarian cancer models (65). While the methods used in both studies are conceptually similar, they differ in the choice of oncogenic lesions, latency, and spontaneous metastatic spread in WT hosts. Furthermore, our study incorporates transgene vectors for oncogene expression and confirms that the resulting tumors are of epithelial origin and display molecular similarities to the human disease. By incorporating *MYC* overexpression and *Brca1* disruption into the platform, we substantially accelerate tumor onset and enable modeling of clinically important HR-deficient tumors. Collectively, these approaches provide a powerful orthogonal system to ovarian cancer models produced from tumor-derived cell or organoid lines (15–19, 66–68).

Our results implicate a cellular senescence program as an important component of response and resistance in HGSOC. Previous work suggests that senescence-inducing therapeutics can stimulate a SASP-dependent remodeling of the TME that, in some instances, leads to senescent cell clearance or sensitizes tumor cells to immune recognition following checkpoint blockade (44, 45). By contrast, in other settings, treatment-associated SASP programs can stimulate tumor relapse and dissemination (69). Herein, we show that the ability of cisplatin or taxol to induce senescence in ovarian cancer cells depends on tumor genotype, being substantially more pronounced following treatment of *Brca1*-deficient (compared to *Brca1*-proficient) ovarian tumors. In turn, this leads to an increase in micronuclei and a cGas/STING-mediated SASP that alters immune cell infiltrates and sensitizes the *Brca1*-deficient tumors to ICB.

Consistent with the importance of the senescence program in therapy response, senescence signatures can be detected in posttreatment samples from HGSOC patients. Moreover, tumors derived from a *Brca1*-deficient cancer that progressed on treatment lose their ability to induce senescence and SASP upon cisplatin treatment, leading to resistance to cisplatin in combination with ICB. Interestingly, the increased propensity of *Brca1*-deficient tumors to undergo senescence and/or activate the cGas/STING pathway appears to extend to other agents, as *Brca1*-deficient models of breast and ovarian cancer treated with PARP inhibitors or, as shown here, taxol show similar behaviors (70–74). As such, senescence induction may underlie the improved response of HR-deficient tumors to genome destabilizing therapies in the clinic.

In our system, the SASP program triggered by cisplatin therapy in *Brca1*-deficient ovarian tumors was limited to *Ccl5*, *Cxcl10*, and *Il6* of the factors examined. cGas suppression efficiently suppressed SASP induction and sensitization to ICB following cisplatin treatment yet had no effect on treatment outcomes following cisplatin monotherapy. This implies that SASP is sufficient to sensitize tumor cells to ICB and, in agreement, injection of SASP-activated tumor cells sensitizes an immunologically cold murine ovarian model to ICB (75), whereas CCL5 suppression in another model attenuates T cell inflammation (73). While it remains possible that senescence and cGas/STING-dependent cytokine induction are parallel processes, they imply that potent antitumor responses require both cell-intrinsic senescence induction and TME modulation.

Although HR deficiency can increase tumor immunogenicity (76), *BRCA1/2* mutations have no effect on the response to ICB monotherapy in HGSOC patients (6, 7, 12). Our model recapitulates these findings: *Brca1*-deficient tumors displayed an increase in immune infiltration pretreatment yet are nonresponsive to ICB. By contrast, our results imply that frontline chemotherapy or PARP inhibitors should sensitize HR-deficient tumors to checkpoint blockade, yet clinical trials to date fail to validate such hypersensitivities as universally operative in patients (77–80). Instead, these trials identify tumor positivity for PD-L1 and CD8 expression—features of the *Brca1*-deficient tumors studied herein—as biomarkers of a combinatorial response (81). It seems likely that the disparate outcomes between the human and animal studies reflect the longer course of tumor evolution in patients, which may further degrade components of the senescence machinery. Accordingly, we see that *Brca1*-deficient tumor cells that acquire senescence defects are nonresponsive to the chemotherapy/ICB combination. Future studies incorporating the flexible features of the EPO-GEMM approach will enable the further dissection of mechanisms that dictate ovarian cancer response and resistance and, more broadly, expedite investigation of other clinically relevant aspects of this disease.

Materials and Methods

Below is an abbreviated summary of the materials and methods used. More details can be found in *SI Appendix, Supplementary Methods*.

Generation of EPO-GEMMs. The 8- to 12-wk-old WT C57BL/6, or transgenic CK8-CreER;LSL-Cas9-IRES-GFP female mice, were anesthetized with isofluorane, and the surgical site was scrubbed with a povidone-iodine scrub (Betadine) and rinsed with 70% alcohol. The target organ was accessed from the left flank, as this allowed for the more readily stabilization of the organ for electroporation than accessing it from the back. After opening the skin and peritoneum, the left ovary and oviduct were exteriorized. A total of 25 μL of a plasmid mix (details in *SI Appendix*, Table S1) was injected under the ovarian bursa using a 30-gauge syringe, which led to the formation of a round, liquid-containing bubble. Tweezer electrodes were tightly placed around this "injection bubble." Two poring pulses of electrical current (50 V) given for 30-ms lengths at 450-ms intervals and five transfer pulses (60 V, 50-ms length, 450-ms intervals) were then applied using an in vivo electroporator (NEPAGENE NEPA21 type II electroporator) (22). After successful electroporation, the peritoneal cavity was rinsed with 500 μL of prewarmed saline. Then, the peritoneal cavity was sutured, and skin staples were used to close the skin. Until they awoke, mice were kept at 37 °C, and postsurgery pain management was done with buprenorphine injections for 3 d. Tumor formation was assessed by abdominal palpation and ultrasound imaging. Tumors were isolated at a humane endpoint.

Characterization of EPO-GEMM Tumors. Histopathological features of EPO-GEMM primary tumors and metastases were assessed by a trained veterinary pathologist (J.E.W.) and their relationship to human HGSOC was determined by immunohistochemistry for relevant markers and through bulk RNA sequencing of tumor tissue. Tumors were shown to harbor intended lesions using Sanger sequencing of the CRISPR-Cas9–induced scar and immunoblotting for MYC. Tumor clonality was analyzed using next-generation DNA sequencing of the *Trp53* amplicon and sparse whole-genome sequencing was used to characterize CNAs (32, 82). Flow cytometry was performed to evaluate tumor immune infiltration.

EPO-GEMM Cell Line Generation. For cell line generation, a tumor piece was minced with a razorblade into small pieces, placed in 5 mL of prewarmed collagenase V buffer (1 μg/mL, Sigma-Aldrich), and incubated at 37 °C for 30 min. Dissociated tissue was washed once with phosphate buffered saline, filtered through a 70-μm cell strainer and centrifuged at 1,500 rpm for 5 min. Cells were plated on 10-cm culture dishes coated with 100 μg/mL collagen (PureCol 5005; Advanced Biomatrix). Primary cultures were passaged at least three times to remove fibroblast contamination. All ovarian cancer cell lines were maintained in a humidified incubator at 37 °C with 5% CO_2 and grown in Dulbecco's modified Eagle's medium supplemented with 10% fetal bovine serum and 100 IU/mL penicillin/streptomycin. All cell lines used in this study tested negative for *Mycoplasma*. Cell lines were validated to carry the correct genotype and to have tumor-initiating capabilities following subcutaneous and i.p. injection. Multiple tumor-derived cell lines were confirmed to produce consistent treatment response patterns in vitro.

Characterization of Cellular Senescence and cGas/STING Response. Assays to evaluate cellular senescence involved SA-β-gal staining (42) and replating assays after drug withdrawal. SASP profiles were assessed using murine cytokine arrays (Eve Technologies) and RT-qPCR. Micronuclei were visualized and quantified by nuclear DAPI staining. The DNA-damage response was determined using IF for 53BP1, γH2AX, and Rad51 (18). The role of the cGas/STING pathway was assessed by transducing cells with two independent cGas shRNAs validated for knockdown and compared to a well-established control shRNA.

Human Cell Line and Tumor Analyses. UWB1.289, UWB.289 + BRCA1, MDA-MB-231, and MDA-MB-436 cell lines were purchased from American Type Culture Collection and cultured according to instructions. CBioPortal.org was used to plot the frequency of mutations, amplifications, and/or deletions in genes of interest in HGSOC patients from various datasets. To evaluate senescence signatures in human tumor samples, senescence signatures were derived from KEGG and previously published works (44, 83). TPMs (transcripts per million) normalized expression data were used to calculate geometric mean score as the senescence signature scores.

Statistics. Statistical analyses were performed using Prism 6 software (GraphPad Software) as described in the figure legends. Statistically significant differences ($P < 0.05$) are indicated with asterisks, accompanied by *P* values in the legends. Statistical significance was determined by Student's *t* test, one-way ANOVA, log-rank test, Pearson's correlation, or Wilcoxon signed-rank test. Survival was measured using the Kaplan–Meier method. Error bars indicate SEM. Unless otherwise stated, the indicated sample size (*n*) represents biological replicates. All samples that met proper experimental conditions were included in the analysis.

Data Availability. RNA-sequencing data have been deposited in Gene Expression Omnibus (GSE181651).

ACKNOWLEDGMENTS. We thank J. Simon and A. Wuest for technical assistance; D. Alonso Curbelo for help with setting up flow cytometry panels; F. J. Sánchez-Rivera, Y. Soto-Feliciano, and B. Ngo for helpful comments on the manuscript; and other members of the S.W.L. laboratory for insightful discussion. This work was supported by the following grants: P30 CA008748-55 (C. Thompson), R01CA233944-02 (S.W.L.), R01NS114653 (J.R.C.-R.), and R21CA248106 (J.R.C.-R.) from the NIH; GC240950 (S.W.L.) from Ludwig Center for Basic and Translational Immunology; OC200166 (J.R.C.-R.), and OC200224 (J.R.C.-R.) from the US Department of Defense; a Mark Foundation for Cancer Research ASPIRE Award (to J.R.C.-R.); an Ovarian Cancer Research Alliance Liz Tilberis Award (D.Z.); and the German Research Foundation (DFG) under Germany's excellence strategy (EXC 2180 – 390900677, J.L.). We also acknowledge fellowship support from the German Academic Scholarship Foundation (S.V.P.), a Thermo Fisher Scientific Antibody Scholarship Award (S.V.P.); a Cancer Research Institute Irvington Fellowship (C.S.), support from the William C. and Joyce C. O'Neil Charitable Trust and the Memorial Sloan Kettering (MSK) Single Cell Sequencing Initiative (T.B.), and an Edward P. Evans Foundation Young Investigator Award (F.M.B.). S.W.L. is the Geoffrey Beene Chair for Cancer Biology and an Investigator in the Howard Hughes Medical Institute (HHMI).

1. D. D. Bowtell *et al.*, Rethinking ovarian cancer II: Reducing mortality from high-grade serous ovarian cancer. *Nat. Rev. Cancer* **15**, 668–679 (2015).
2. J. Brahmer *et al.*, Nivolumab versus docetaxel in advanced squamous-cell non-small-cell lung cancer. *N. Engl. J. Med.* **373**, 123–135 (2015).
3. J. D. Wolchok *et al.*, Overall survival with combined nivolumab and ipilimumab in advanced melanoma. *N. Engl. J. Med.* **377**, 1345–1356 (2017).
4. H. Borghaei *et al.*, Nivolumab versus docetaxel in advanced nonsquamous non-small-cell lung cancer. *N. Engl. J. Med.* **373**, 1627–1639 (2015).
5. Y. L. Liu, D. Zamarin, Combination immune checkpoint blockade strategies to maximize immune response in gynecological cancers. *Curr. Oncol. Rep.* **20**, 94 (2018).
6. M. L. Disis *et al.*, Avelumab (MSB0010718C; anti-PD-L1) in patients with recurrent/refractory ovarian cancer from the JAVELIN solid tumor phase Ib trial: Safety and clinical activity. *J. Clin. Oncol.* **34**, 5533 (2016).
7. U. A. Matulonis *et al.*, Antitumor activity and safety of pembrolizumab in patients with advanced recurrent ovarian cancer: Results from the phase II KEYNOTE-100 study. *Ann. Oncol.* **30**, 1080–1087 (2019).
8. S. I. Kim *et al.*, Effect of BRCA mutational status on survival outcome in advanced-stage high-grade serous ovarian cancer. *J. Ovarian Res.* **12**, 40 (2019).
9. Cancer Genome Atlas Research Network, Integrated genomic analyses of ovarian carcinoma. *Nature* **474**, 609–615 (2011).
10. Y. K. Wang *et al.*, Genomic consequences of aberrant DNA repair mechanisms stratify ovarian cancer histotypes. *Nat. Genet.* **49**, 856–865 (2017).
11. A. Ashworth, A synthetic lethal therapeutic approach: Poly(ADP) ribose polymerase inhibitors for the treatment of cancers deficient in DNA double-strand break repair. *J. Clin. Oncol.* **26**, 3785–3790 (2008).
12. Y. L. Liu *et al.*, BRCA mutations, homologous DNA repair deficiency, tumor mutational burden, and response to immune checkpoint inhibition in recurrent ovarian cancer. *JCO Precis. Oncol.* **4**, 665–679 (2020).
13. T. E. Keenan, K. P. Burke, E. M. Van Allen, Genomic correlates of response to immune checkpoint blockade. *Nat. Med.* **25**, 389–402 (2019).
14. P. J. Morin, A. T. Weeraratna, Genetically-defined ovarian cancer mouse models. *J. Pathol.* **238**, 180–184 (2016).
15. S. Zhang *et al.*, Genetically defined, syngeneic organoid platform for developing combination therapies for ovarian cancer. *Cancer Discov.* **11**, 362–383 (2021).
16. K. Löhmussaar *et al.*, Assessing the origin of high-grade serous ovarian cancer using CRISPR-modification of mouse organoids. *Nat. Commun.* **11**, 2660 (2020).
17. O. Kopper *et al.*, An organoid platform for ovarian cancer captures intra- and interpatient heterogeneity. *Nat. Med.* **25**, 838–849 (2019).
18. S. J. Hill *et al.*, Prediction of DNA repair inhibitor response in short-term patient-derived ovarian cancer organoids. *Cancer Discov.* **8**, 1404–1421 (2018).
19. Y. Maru, N. Tanaka, M. Itami, Y. Hippo, Efficient use of patient-derived organoids as a preclinical model for gynecologic tumors. *Gynecol. Oncol.* **154**, 189–198 (2019).
20. M. Binnewies *et al.*, Understanding the tumor immune microenvironment (TIME) for effective therapy. *Nat. Med.* **24**, 541–550 (2018).
21. M. D. Wellenstein, K. E. de Visser, Cancer-cell-intrinsic mechanisms shaping the tumor immune landscape. *Immunity* **48**, 399–416 (2018).
22. J. Leibold *et al.*, Somatic tissue engineering in mouse models reveals an actionable role for WNT pathway alterations in prostate cancer metastasis. *Cancer Discov.* **10**, 1038–1057 (2020).
23. K. W. McCool *et al.*, Murine oviductal high-grade serous carcinomas mirror the genomic alterations, gene expression profiles, and immune microenvironment of their human counterparts. *Cancer Res.* **80**, 877–889 (2020).
24. R. Perets *et al.*, Transformation of the fallopian tube secretory epithelium leads to high-grade serous ovarian cancer in Brca;Tp53;Pten models. *Cancer Cell* **24**, 751–765 (2013).
25. Y. Zhai *et al.*, High-grade serous carcinomas arise in the mouse oviduct via defects linked to the human disease. *J. Pathol.* **243**, 16–25 (2017).
26. E. Maniati *et al.*, Mouse ovarian cancer models recapitulate the human tumor microenvironment and patient response to treatment. *Cell Rep.* **30**, 525–540.e7 (2020).
27. A. M. Karst, K. Levanon, R. Drapkin, Modeling high-grade serous ovarian carcinogenesis from the fallopian tube. *Proc. Natl. Acad. Sci. U.S.A.* **108**, 7547–7552 (2011).
28. S. Orsulic *et al.*, Induction of ovarian cancer by defined multiple genetic changes in a mouse model system. *Cancer Cell* **1**, 53–62 (2002).
29. E. Lengyel, Ovarian cancer development and metastasis. *Am. J. Pathol.* **177**, 1053–1064 (2010).
30. R. J. Kurman, M. L. Carcangiu, C. S. Herrington, R. H. Young, *WHO Classification of Tumours of Female Reproductive Organs* (International Agency for Research on Cancer, ed. 4, 2014), https://apps.who.int.
31. S. Elloul *et al.*, Snail, slug, and smad-interacting protein 1 as novel parameters of disease aggressiveness in metastatic ovarian and breast carcinoma. *Cancer* **103**, 1631–1643 (2005).
32. T. Baslan *et al.*, Optimizing sparse sequencing of single cells for highly multiplex copy number profiling. *Genome Res.* **25**, 714–724 (2015).
33. G. Macintyre *et al.*, Copy number signatures and mutational processes in ovarian carcinoma. *Nat. Genet.* **50**, 1262–1270 (2018).
34. T. Motohara *et al.*, Transient depletion of p53 followed by transduction of c-Myc and K-Ras converts ovarian stem-like cells into tumor-initiating cells. *Carcinogenesis* **32**, 1597–1606 (2011).
35. K. C. Strickland *et al.*, Association and prognostic significance of BRCA1/2-mutation status with neoantigen load, number of tumor-infiltrating lymphocytes and expression of PD-1/PD-L1 in high grade serous ovarian cancer. *Oncotarget* **7**, 13587–13598 (2016).
36. V. Wieser *et al.*, *BRCA1/2* and *TP53* mutation status associates with *PD-1* and *PD-L1* expression in ovarian cancer. *Oncotarget* **9**, 17501–17511 (2018).
37. E. L. Goode *et al.*; Ovarian Tumor Tissue Analysis (OTTA) Consortium, Dose-response association of CD8+ tumor-infiltrating lymphocytes and survival time in high-grade serous ovarian cancer. *JAMA Oncol.* **3**, e173290 (2017).
38. R. W. Naumann *et al.*, Patients with BRCA mutations have superior outcomes after intraperitoneal chemotherapy in optimally resected high grade ovarian cancer. *Gynecol. Oncol.* **151**, 477–480 (2018).

39. K. L. Bolton *et al.*; EMBRACE; kConFab Investigators; Cancer Genome Atlas Research Network, Association between BRCA1 and BRCA2 mutations and survival in women with invasive epithelial ovarian cancer. *JAMA* **307**, 382–390 (2012).
40. F. Debacq-Chainiaux, J. D. Erusalimsky, J. Campisi, O. Toussaint, Protocols to detect senescence-associated beta-galactosidase (SA-betagal) activity, a biomarker of senescent cells in culture and in vivo. *Nat. Protoc.* **4**, 1798–1806 (2009).
41. N. E. Sharpless, C. J. Sherr, Forging a signature of in vivo senescence. *Nat. Rev. Cancer* **15**, 397–408 (2015).
42. V. Krizhanovsky *et al.*, Senescence of activated stellate cells limits liver fibrosis. *Cell* **134**, 657–667 (2008).
43. T.-W. Kang *et al.*, Senescence surveillance of pre-malignant hepatocytes limits liver cancer development. *Nature* **479**, 547–551 (2011).
44. M. Ruscetti *et al.*, NK cell-mediated cytotoxicity contributes to tumor control by a cytostatic drug combination. *Science* **362**, 1416–1422 (2018).
45. M. Ruscetti *et al.*, Senescence-induced vascular remodeling creates therapeutic vulnerabilities in pancreas cancer. *Cell* **181**, 424–441.e21 (2020).
46. C. DelloRusso *et al.*, Functional characterization of a novel BRCA1-null ovarian cancer cell line in response to ionizing radiation. *Mol. Cancer Res.* **5**, 35–45 (2007).
47. F. Elstrodt *et al.*, BRCA1 mutation analysis of 41 human breast cancer cell lines reveals three new deleterious mutants. *Cancer Res.* **66**, 41–45 (2006).
48. A. Jiménez-Sánchez *et al.*, Unraveling tumor-immune heterogeneity in advanced ovarian cancer uncovers immunogenic effect of chemotherapy. *Nat. Genet.* **52**, 582–593 (2020).
49. A. A. Ahmed *et al.*, The extracellular matrix protein TGFBI induces microtubule stabilization and sensitizes ovarian cancers to paclitaxel. *Cancer Cell* **12**, 514–527 (2007).
50. C. K. Ingemarsdotter *et al.*, Paclitaxel resistance increases oncolytic adenovirus efficacy via upregulated CAR expression and dysfunctional cell cycle control. *Mol. Oncol.* **9**, 791–805 (2015).
51. Z. Dou *et al.*, Cytoplasmic chromatin triggers inflammation in senescence and cancer. *Nature* **550**, 402–406 (2017).
52. T. Li, Z. J. Chen, The cGAS-cGAMP-STING pathway connects DNA damage to inflammation, senescence, and cancer. *J. Exp. Med.* **215**, 1287–1299 (2018).
53. S. Glück *et al.*, Innate immune sensing of cytosolic chromatin fragments through cGAS promotes senescence. *Nat. Cell Biol.* **19**, 1061–1070 (2017).
54. H. Yang, H. Wang, J. Ren, Q. Chen, Z. J. Chen, cGAS is essential for cellular senescence. *Proc. Natl. Acad. Sci. U.S.A.* **114**, E4612–E4620 (2017).
55. J. Wu, Z. J. Chen, Innate immune sensing and signaling of cytosolic nucleic acids. *Annu. Rev. Immunol.* **32**, 461–488 (2014).
56. K. J. Mackenzie *et al.*, cGAS surveillance of micronuclei links genome instability to innate immunity. *Nature* **548**, 461–465 (2017).
57. E. E. Parkes *et al.*, Activation of STING-dependent innate immune signaling By S-phase-specific DNA damage in breast cancer. *J. Natl. Cancer Inst.* **109**, djw199 (2016).
58. A. M. Heijink *et al.*, BRCA2 deficiency instigates cGAS-mediated inflammatory signaling and confers sensitivity to tumor necrosis factor-alpha-mediated cytotoxicity. *Nat. Commun.* **10**, 100–114 (2019).
59. L. Fournel *et al.*, Cisplatin increases PD-L1 expression and optimizes immune checkpoint blockade in non-small cell lung cancer. *Cancer Lett.* **464**, 5–14 (2019).
60. L. Tran *et al.*, Cisplatin alters antitumor immunity and synergizes with PD-1/PD-L1 inhibition in head and neck squamous cell carcinoma. *Cancer Immunol. Res.* **5**, 1141–1151 (2017).
61. R. S. Herbst *et al.*, Predictive correlates of response to the anti-PD-L1 antibody MPDL3280A in cancer patients. *Nature* **515**, 563–567 (2014).
62. S. F. Bunting *et al.*, 53BP1 inhibits homologous recombination in Brca1-deficient cells by blocking resection of DNA breaks. *Cell* **141**, 243–254 (2010).
63. H. Farmer *et al.*, Targeting the DNA repair defect in BRCA mutant cells as a therapeutic strategy. *Nature* **434**, 917–921 (2005).
64. M. S. Chapman, I. M. Verma, Transcriptional activation by BRCA1. *Nature* **382**, 678–679 (1996).
65. K. Teng *et al.*, Modeling high-grade serous ovarian carcinoma using a combination of in vivo fallopian tube electroporation and CRISPR-Cas9-mediated genome editing. *Cancer Res.* **81**, 5147–5160 (2021).
66. S. Iyer *et al.*, Genetically defined syngeneic mouse models of ovarian cancer as tools for the discovery of combination immunotherapy. *Cancer Discov.* **11**, 384–407 (2021).
67. J. Walton *et al.*, CRISPR/Cas9-mediated Trp53 and Brca2 knockout to generate improved murine models of ovarian high-grade serous carcinoma. *Cancer Res.* **76**, 6118–6129 (2016).
68. D. Xing, S. Orsulic, A mouse model for the molecular characterization of Brca1-associated ovarian carcinoma. *Cancer Res.* **66**, 8949–8953 (2006).
69. M. Demaria *et al.*, Cellular senescence promotes adverse effects of chemotherapy and cancer relapse. *Cancer Discov.* **7**, 165–176 (2017).
70. L. Ding *et al.*, PARP inhibition elicits STING-dependent antitumor immunity in Brca1-deficient ovarian cancer. *Cell Rep.* **25**, 2972–2980.e5 (2018).
71. S. Grabosch *et al.*, Cisplatin-induced immune modulation in ovarian cancer mouse models with distinct inflammation profiles. *Oncogene* **38**, 2380–2393 (2019).
72. C. Pantelidou *et al.*, PARP inhibitor efficacy depends on $CD8^+$ T-cell recruitment via intratumoral STING pathway activation in BRCA-deficient models of triple-negative breast cancer. *Cancer Discov.* **9**, 722–737 (2019).
73. M. Bruand *et al.*, Cell-autonomous inflammation of BRCA1-deficient ovarian cancers drives both tumor-intrinsic immunoreactivity and immune resistance via STING. *Cell Rep.* **36**, 109412 (2021).
74. H. Fleury *et al.*, Exploiting interconnected synthetic lethal interactions between PARP inhibition and cancer cell reversible senescence. *Nat. Commun.* **10**, 2556 (2019).
75. X. Hao *et al.*, Sensitization of ovarian tumor to immune checkpoint blockade by boosting senescence-associated secretory phenotype. *iScience* **24**, 102016 (2020).
76. Y. Dai, C. Sun, Y. Feng, Q. Jia, B. Zhu, Potent immunogenicity in BRCA1-mutated patients with high-grade serous ovarian carcinoma. *J. Cell. Mol. Med.* **22**, 3979–3986 (2018).
77. K. N. Moore *et al.*, LBA31 primary results from IMagyn050/GOG 3015/ENGOT-OV39, a double-blind placebo (pbo)-controlled randomised phase III trial of bevacizumab (bev)-containing therapy +/− atezolizumab (atezo) for newly diagnosed stage III/IV ovarian cancer (OC). *Ann. Oncol.* **31**, S1161–S1162 (2020).
78. E. Pujade-Lauraine *et al.*, Avelumab alone or in combination with chemotherapy versus chemotherapy alone in platinum-resistant or platinum-refractory ovarian cancer (JAVELIN Ovarian 200): An open-label, three-arm, randomised, phase 3 study. *Lancet Oncol.* **22**, 1034–1046 (2021).
79. P. A. Konstantinopoulos, R. Ceccaldi, G. I. Shapiro, A. D. D'Andrea, Homologous recombination deficiency: Exploiting the fundamental vulnerability of ovarian cancer. *Cancer Discov.* **5**, 1137–1154 (2015).
80. J. A. Ledermann *et al.*, Avelumab in combination with and/or following chemotherapy vs chemotherapy alone in patients with previously untreated epithelial ovarian cancer: Results from the phase 3 javelin ovarian 100 trial. *Gynecol. Oncol.* **159**, 13–14 (2020).
81. A. Färkkilä *et al.*, Immunogenomic profiling determines responses to combined PARP and PD-1 inhibition in ovarian cancer. *Nat. Commun.* **11**, 1459 (2020).
82. T. Baslan *et al.*, Genome-wide copy number analysis of single cells. *Nat. Protoc.* **7**, 1024–1041 (2012).
83. N. Tasdemir *et al.*, BRD4 connects enhancer remodeling to senescence immune surveillance. *Cancer Discov.* **6**, 612–629 (2016).

Supplementary Figures

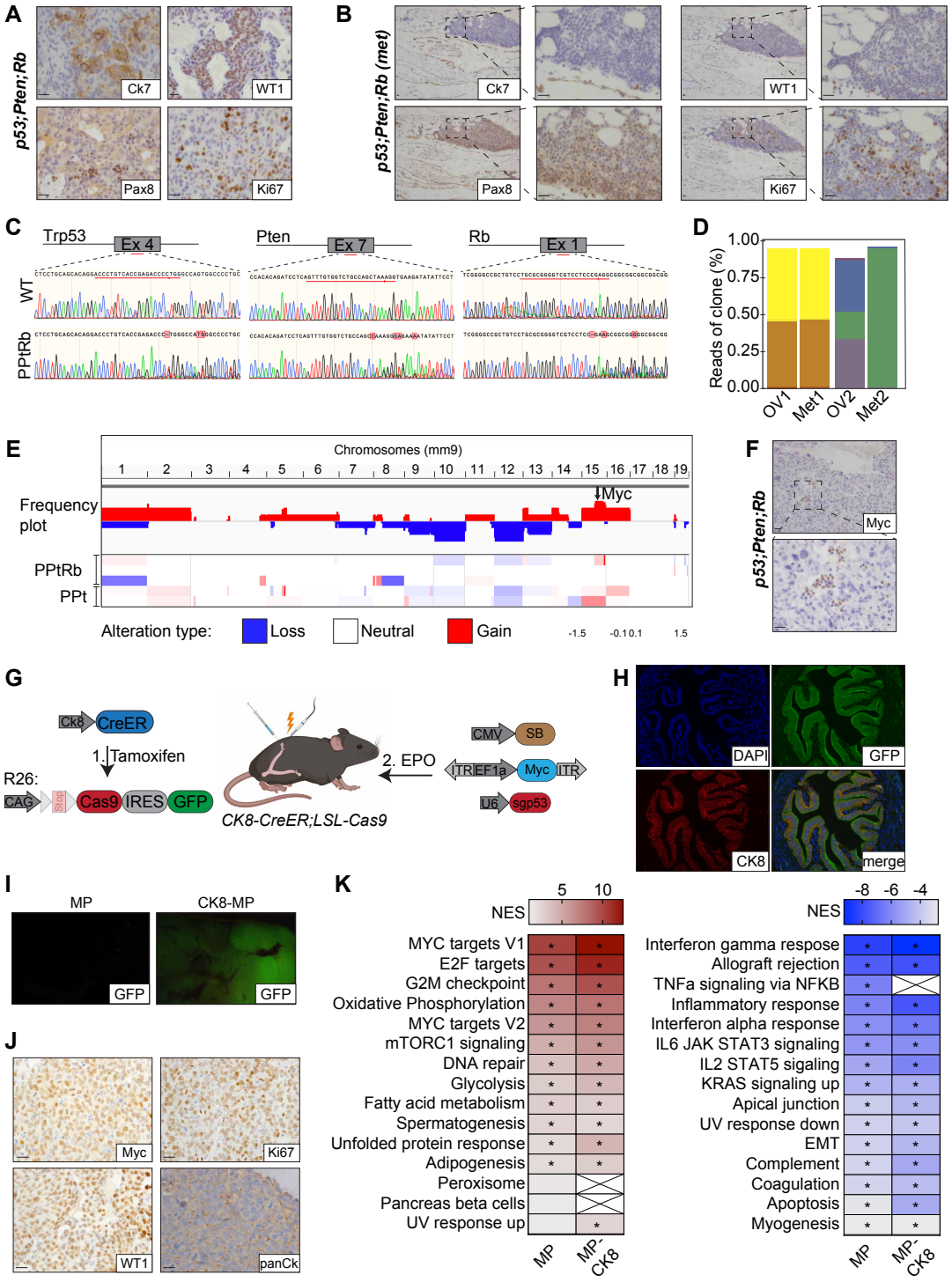

Figure S1: EPO-GEMM approach generates high-grade serous ovarian cancer that is of epithelial origin. (A-B) Representative immunohistochemical staining of a *Trp53;Pten;Rb* EPO-GEMM ovarian tumor **(A)** and a corresponding micrometastasis in the omentum **(B)** for the HGSOC markers CK7, WT1, Pax8 and Ki67. Scale bar 20 µm. **(C)** Sanger sequencing confirming editing of the respective gene loci targeted by the indicated CRISPR-Cas9-sgRNAs in a *Trp53;Pten;Rb* EPO-GEMM ovarian tumor compared to an unmodified wild-type (WT) tissue. **(D)** Clonality analysis of two representative paired primary tumors (OV) and omentum metastasis (Met). Percentage of reads of the dominant clones was derived by deep sequencing of the *Trp53* amplicon. **(E)** Frequency plot of CNA analysis of *Trp53;Pten;Rb* (PPtRb, n=3) and *Trp53;Pten* (PPt, n=2) EPO-GEMM ovarian tumors. **(F)** Representative immunohistochemical staining of a *Trp53;Pten;Rb* EPO-GEMM ovarian tumor for MYC. Scale bar 20 µm. **(G)** Schematic of the EPO-GEMM approach *in CK8-CreER;LSL-Cas9-IRES-GFP* mice. Tamoxifen is given to excise the Stop-cassette to drive Cas9 expression in Ck8-positive cells. A *MYC* transposon vector, a transposon vector harboring a sgRNA targeting *Trp53* (sg*p53*), and a Sleeping Beauty transposase (SB) are delivered into the ovary of *CK8-CreER-Cas9* mice by direct *in vivo* electroporation. **(H)** Representative immunofluorescence staining of the oviduct of a *CK8-CreER;LSL-Cas9-IRES-GFP* mouse one week after Tamoxifen treatment. **(I)** Macroscopic GFP expression in MP tumors generated by *in vivo* tissue electroporation of a WT mouse (left) or a *CK8-CreER;LSL-Cas9-IRES-GFP* mouse (right). **(J)** Representative immunohistochemical staining of MP EPO-GEMM ovarian tumors generated in *CK8-CreER;LSL-Cas9-IRES-GFP* mice. Scale bar 20 µm. **(K)** Comparison of top enriched (left, red) and depleted (right, blue) Hallmark genesets derived from RNA-seq data in MP and CK8-MP EPO-GEMM tumors compared to normal tissue. Star indicates p-value < 0.05.

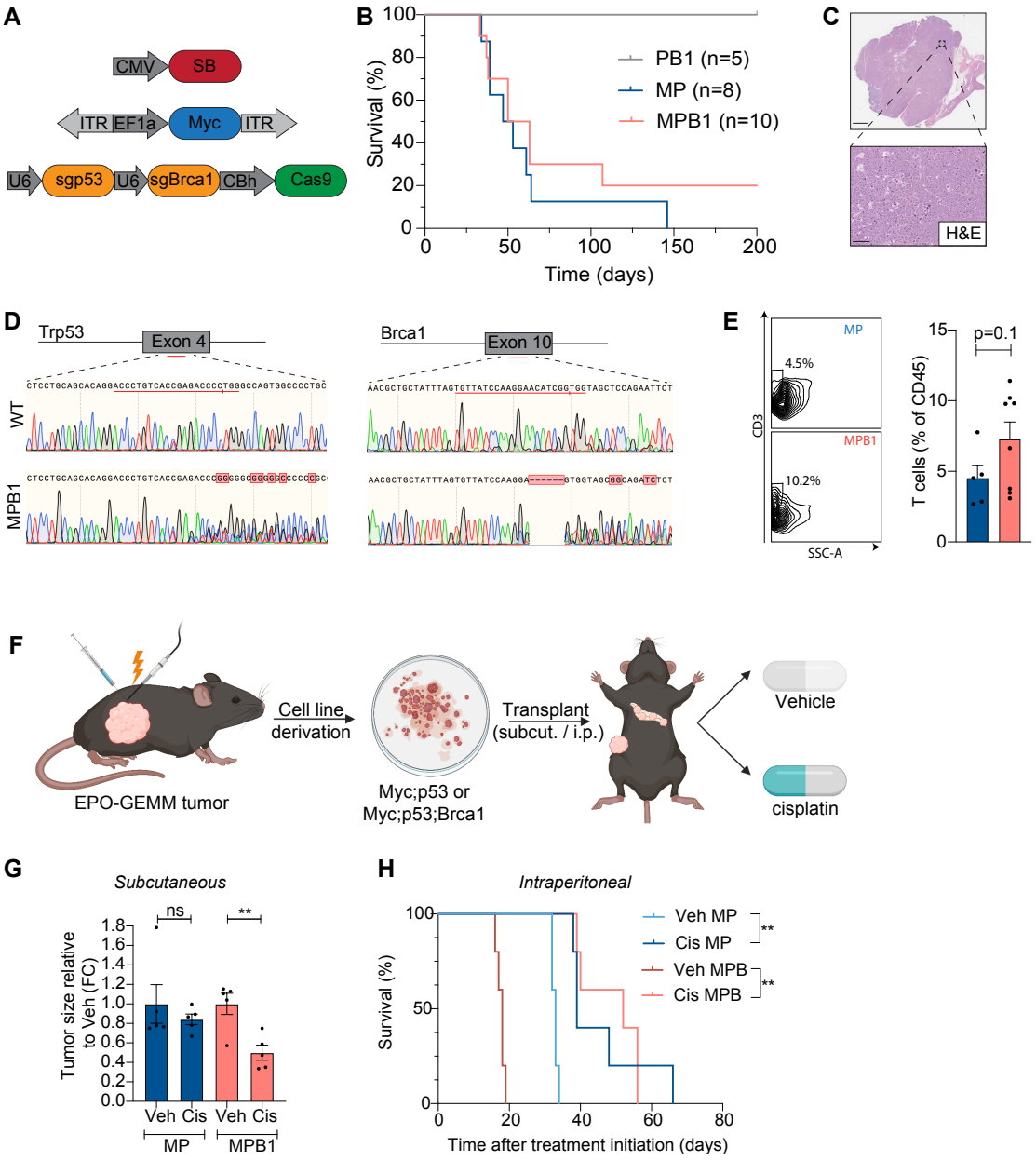
A
CMV
SB
ITR
EF1a
Myc
ITR
U6
sgp53
U6
sgBrca1
CBh
Cas9
B
Survival (%)
Time (days)
PB1 (n=5)
MP (n=8)
MPB1 (n=10)
C
H&E
D
Trp53
Exon 4
Brca1
Exon 10
WT
MPB1
E
MP
MPB1
4.5%
10.2%
CD3
SSC-A
T cells (% of CD45)
p=0.1
F
EPO-GEMM tumor
Cell line derivation
Myc;p53 or Myc;p53;Brca1
Transplant (subcut. / i.p.)
Vehicle
cisplatin
G
Subcutaneous
Tumor size relative to Veh (FC)
ns
**
Veh
Cis
Veh
Cis
MP
MPB1
H
Intraperitoneal
Survival (%)
Time after treatment initiation (days)
Veh MP
Cis MP
Veh MPB
Cis MPB
**
**

Figure S2: HR deficiency drives tumors with increased T-cell infiltration and improved therapy response. (A) Plasmid combination used to induce HR-deficient EPO-GEMM tumors. **(B)** Kaplan-Meier survival curve of C57BL/6 mice electroporated with the indicated combinations of plasmids. **(C)** Representative H&E staining of a MPB1 EPO-GEMM tumor. Scale bar 5000 µm (top), 100 µm (bottom). **(D)** Sanger sequencing confirming editing of the *Trp*53 and *Brca1* gene loci targeted by the indicated CRISPR-Cas9 sgRNAs in a MPB1 EPO-GEMM ovarian tumor. **(E)** Analysis of the T cell infiltrate of representative EPO-GEMM tumors of the indicated genotypes by flow cytometry (n=5-8 mice per group). **(F)** Schematic of transplantation approach of EPO-GEMM derived cell lines. **(G)** Relative tumor size of subcutaneously transplanted MP or MPB1 tumor cell lines treated with vehicle or cisplatin (n=5 mice per group). **(H)** Kaplan-Meier survival curve of mice after i.p. transplantation of MP or MPB1 tumor cell lines and treatment with vehicle or cisplatin (n=5 mice per group). Mice were randomized according to luciferase signal before treatment initiation. *p ≤ 0.05, **p ≤ 0.01, ***p ≤ 0.001, ns: not significant; Mean ± SEM; Analyses performed using unpaired t test (E, G) and log-rank test (H).

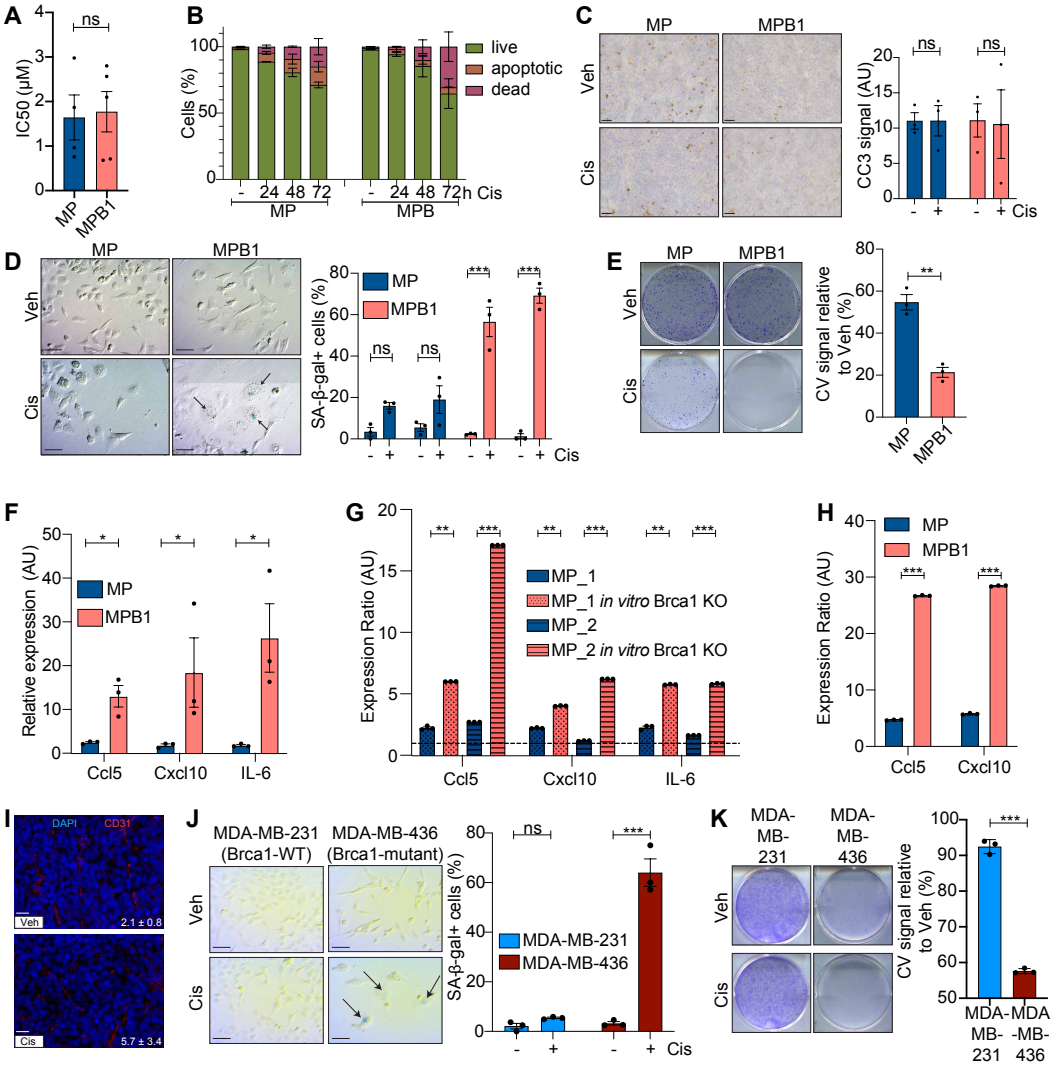
A
IC50 (μM)
ns
MP
MPB1
B
Cells (%)
live
apoptotic
dead
- 24 48 72 - 24 48 72h Cis
MP
MPB
C
MP
MPB1
Veh
Cis
CC3 signal (AU)
ns
ns
- + - + Cis
D
MP
MPB1
Veh
Cis
SA-β-gal+ cells (%)
MP
MPB1
ns
ns
***
***
- + - + - + - + Cis
E
MP
MPB1
Veh
Cis
CV signal relative to Veh (%)
**
MP
MPB1
F
Relative expression (AU)
*
*
*
MP
MPB1
Ccl5
Cxcl10
IL-6
G
Expression Ratio (AU)
**
***
**
***
**
***
MP_1
MP_1 in vitro Brca1 KO
MP_2
MP_2 in vitro Brca1 KO
Ccl5
Cxcl10
IL-6
H
Expression Ratio (AU)
MP
MPB1
***
***
Ccl5
Cxcl10
I
DAPI
CD31
Veh
2.1 ± 0.8
Cis
5.7 ± 3.4
J
MDA-MB-231 (Brca1-WT)
MDA-MB-436 (Brca1-mutant)
Veh
Cis
SA-β-gal+ cells (%)
ns
***
MDA-MB-231
MDA-MB-436
- + - + Cis
K
MDA-MB-231
MDA-MB-436
Veh
Cis
CV signal relative to Veh (%)
***
MDA-MB-231
MDA-MB-436
L
Rb targets senescent (Chicas et al.)
NES = 4.32
FDR q = 0.000
TNFa signaling via NFkB (Hallmark)
NES = 6.04
FDR q = 0.000
Regulation of cytokine production (GO)
NES = 4.64
FDR q = 0.000
Protein secretion (Hallmark)
NES = 4.32
FDR q = 0.000

Figure S3: Chemotherapy treatment induces senescence and SASP in HR-deficient HGSOC. **(A)** IC50 values of MP or MPB1 cell lines treated with cisplatin. Cell viability was calculated relative to vehicle-treated control cells, measured with CellTiter-Glo assay 72h after treatment (n = 4-5). **(B)** Quantification of live (Annexin-V^-, PI^-), apoptotic (Annexin-V^+, PI^-) or dead (Annexin-V^+, PI^+) cells in MP or MPB1 cell lines after 24, 48 or 72 h of cisplatin treatment (n = 3). **(C)** Representative immunohistochemical staining and quantification of cleaved caspase-3 (CC3) signal in subcutaneously transplanted MP or MPB1 ovarian tumors after two cycles of cisplatin treatment (n = 3). Scale bar 40 µm. **(D)** SA-ß-gal staining of cell lines treated with vehicle or 1 µM cisplatin for 6 days (n = 2 independent cell lines per genotype with n = 3 technical replicates). Scale bar 50 µm. **(E)** Clonogenic crystal violet (CV) assay of MP or MPB1 cells replated in the absence of drugs after 6-day pretreatment as in (D) (n = 3 independent cell lines per genotype). **(F)** RT-qPCR analysis of *Ccl5*, *Cxcl10* and *Il6* in MP or MPB1 cell lines. Expression ratio of cisplatin-treated relative to untreated is shown. Each point represents a cell line derived from a different mouse tumor (n = 3). **(G)** RT-qPCR analysis of *Ccl5*, *Cxcl10* and *Il6* in MP cell lines transfected with control or *Brca1*-targeting sgRNA. Expression ratio of cisplatin-treated relative to untreated is shown. The different patterns represent a cell line derived from a different MP mouse tumor, in which *Brca1* was knocked-out after cell line establishment (n = 3 technical replicates per independent line). **(H)** RT-qPCR analysis of *Ccl5* and *Cxcl10* in MP or MPB1 cell lines treated with 50 nM Taxol. Expression ratio of treated relative to untreated is shown (n = 3). **(I)** IF staining and quantification of $CD31^+$ blood vessels of transplanted tumors after two cycles of cisplatin treatment (n = 3). Scale bar 20 µm. **(J)** SA-ß-gal staining (left) and quantification (right) of either *BRCA1* wild-type (WT) (MDA-MB-231) or -mutant (MDA-MB-436) human breast cancer cell lines after treatment with vehicle or cisplatin for 6 days (n = 3). Scale bar 50 µm. **(K)** Clonogenic crystal violet (CV) assay of human BRCA-WT or -mutant breast cancer cells replated in the absence of drugs after 6-day pretreatment as in (J) (n = 3). **(L)** Gene set enrichment analysis (GSEA) comparing expression of senescence and SASP signatures in patients after and before chemotherapy treatment in a human ovarian cancer dataset (Jiménez-Sanchez et al. 2020).

*p ≤ 0.05, **p ≤ 0.01, ***p ≤ 0.001, ns: not significant; Mean ± SEM; Analyses performed using unpaired t-test (A, C, E-K), one-way ANOVA (D) and Wilcoxon signed-rank test (L).

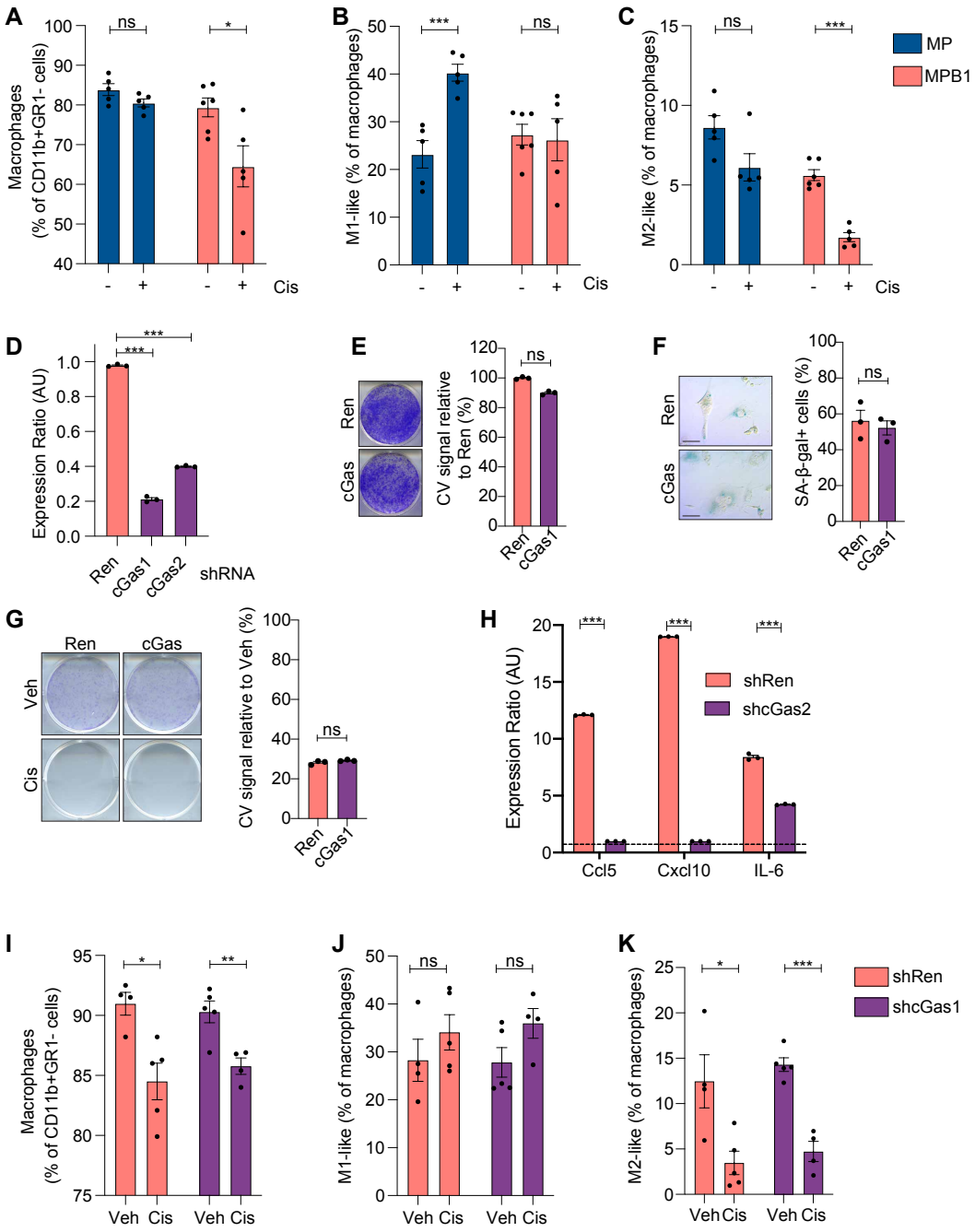
A
Macrophages (% of CD11b+GR1- cells)
ns
*
Cis
B
M1-like (% of macrophages)
***
ns
C
M2-like (% of macrophages)
MP
MPB1
D
Expression Ratio (AU)
Ren
cGas1
cGas2
shRNA
E
Ren
cGas
CV signal relative to Ren (%)
F
SA-β-gal+ cells (%)
G
Veh
Cis
CV signal relative to Veh (%)
H
Expression Ratio (AU)
shRen
shcGas2
Ccl5
Cxcl10
IL-6
I
Veh
J
K
shcGas1

Figure S4: cGas knockdown does not alter the myeloid immune compartment or cell-intrinsic senescence response. (A-C) Infiltration of macrophages (**A**) and percentages of M1-like (CD206-, CD80+) (**B**) and M2-like (CD206+, CD80-) (**C**) macrophages in subcutaneously transplanted MP or MPB1 ovarian tumors after treatment with 2 cycles of cisplatin (n = 5-6 mice per group). **(D)** RT-qPCR analysis of cGas in MPB1 cell lines containing control Renilla (shRen) or cGas shRNAs (shcGas) shRNAs targeting (n = 3). **(E)** Clonogenic assay of MPB1 cell lines containing control Renilla (shRen) or cGas (shcGas) shRNAs (n = 3). **(F)** SA-ß-gal staining of MPB1 cell lines containing control Renilla (shRen) or cGas (shcGas) shRNAs after treatment with vehicle or cisplatin for 6 days (n = 3). Scale bar 20 µm. **(G)** Clonogenic crystal violet (CV) assay of MP or MPB1 cells replated in the absence of drugs after 6-day pretreatment as in (F) (n = 3). (**H**) RT-qPCR analysis of *Ccl5*, *Cxcl10* and *Il6* in MPB1 cell lines containing control Renilla (shRen) or cGas (shcGas) shRNAs. Expression ratio of cisplatin-treated relative to untreated is shown (n = 3). (**I-K**) Infiltration of macrophages (**I**) and percentages of M1 (**J**) and M2 (**K**) macrophages in transplanted shRen or shcGas MPB1 ovarian tumors after treatment with 2 cycles of cisplatin (n = 4-5 mice per group).

*p ≤ 0.05, **p ≤ 0.01, ***p ≤ 0.001, ns: not significant; Mean ± SEM; Analyses performed using unpaired t-test (A-C, E-K) or one-way ANOVA (D).

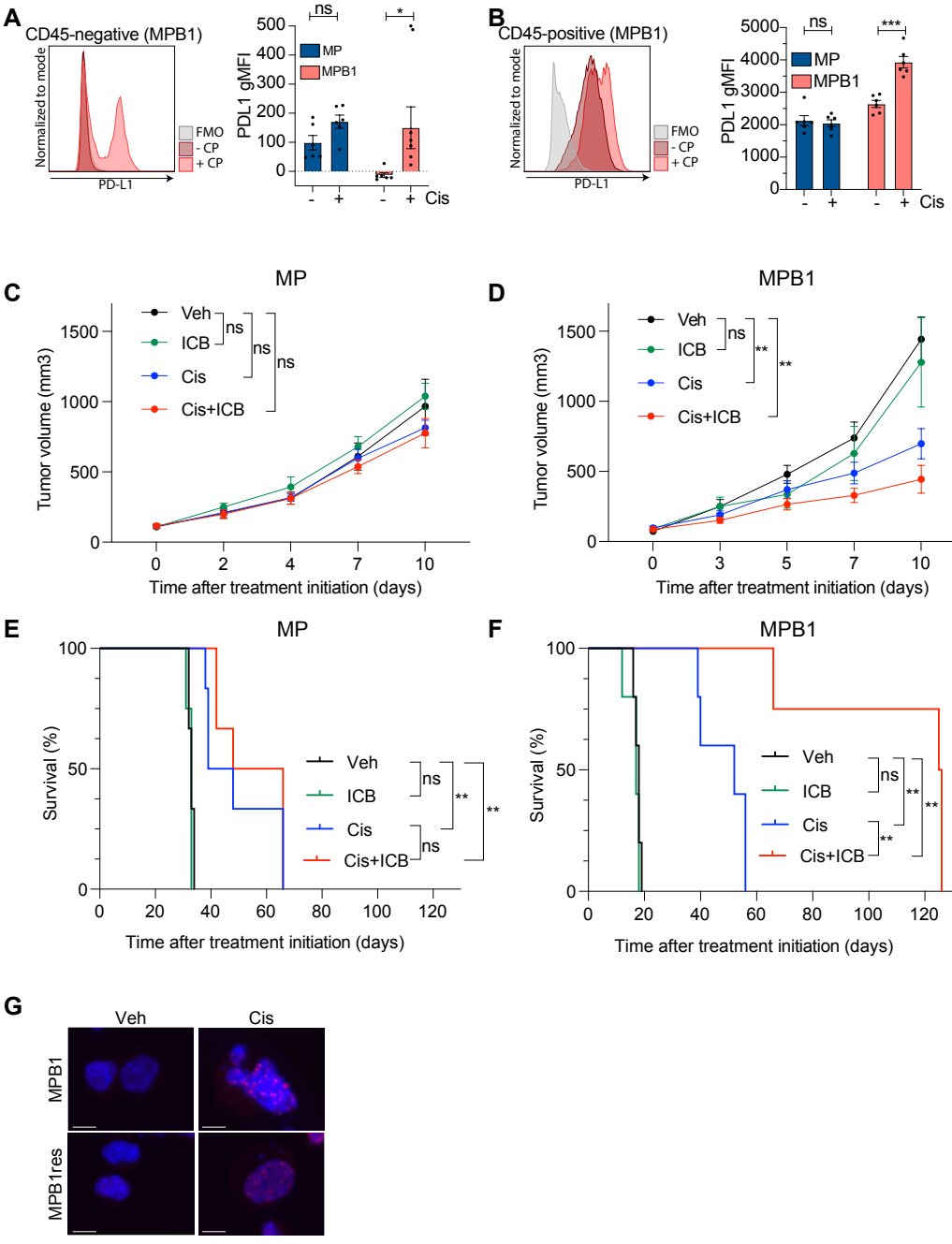
A
CD45-negative (MPB1)
Normalized to mode
PD-L1
FMO
- CP
+ CP
PDL1 gMFI
MP
MPB1
ns
*
Cis
B
CD45-positive (MPB1)
***
C
MP
Tumor volume (mm3)
Veh
ICB
Cis
Cis+ICB
Time after treatment initiation (days)
D
MPB1
**
E
MP
Survival (%)
F
MPB1
G
Veh
Cis
MPB1
MPB1res

Figure S5: Treatment response of HR-proficient and -deficient HGSOC after treatment with chemotherapy and ICB. (A+B) Representative MFI plot (left) and quantification (right) of PD-L1 expression on tumor cells (CD45-negative) **(A)** or immune cells (CD45-positive) **(B)** from subcutaneously transplanted MPB1 ovarian tumors treated with vehicle or cisplatin (n = 5-6 mice per group). **(C+D)** Tumor growth of subcutaneously transplanted MP **(C)** or MPB1 **(D)** tumors treated with vehicle, ICB, cisplatin or cisplatin + ICB (n = 5 mice per group). **(E+F)** Kaplan-Meier survival curve of MP **(E)** or MPB1 **(F)** tumors generated by i.p. injection (n = 4-6 mice per group). Mice were randomized according to luciferase signal before treatment initiation. **(G)** Immunofluorescence staining of 53BP1 foci in MP and MPB1 cell lines treated with vehicle or cisplatin for 72h. Scale bar 10 µm.

*p ≤ 0.05, **p ≤ 0.01, ***p ≤ 0.001, ns: not significant; Mean ± SEM; Analyses performed using unpaired t-test (A-B), one-way ANOVA (C-D) and log-rank test (E-F).

Supplementary Methods

Animal studies

Mice were maintained under specific pathogen-free conditions, and food and water were provided ad libitum. Mice were purchased from Jackson laboratory. CK8-CreER (Van Keymeulen et al. 2011) male mice were crossed with LSL-Cas9-IRES-GFP female mice to produce CK8-CreER;LSL-Cas9-IRES-GFP female mice for generation of EPO-GEMMs. All mouse experiments were approved by the Memorial Sloan-Kettering Cancer Center (MSKCC) Internal Animal Care and Use Committee.

Ultrasound and bioluminescence imaging

High-contrast ultrasound imaging was performed on a Vevo 2100 System with a MS250 13- to 24-MHz scanhead (VisualSonics) to stage and quantify ovarian EPO-GEMM tumor burden. Tumor volume was analyzed using Vevo LAB software.

For visualizing ovarian tumor cells with luciferase, luciferase-blasticidin (Luc-Blast) constructs were cloned into MSCV-based vectors and retroviruses were packaged by co-transfection of Gag-Pol expressing 293 T cells with expression constructs and envelope vectors (VSV-G) using the Lipofectamine method (Thermo Fisher). Following transduction, cells were selected with Blasticidin S (10 μg/ml; Life Technologies) for 5 days. Bioluminescence imaging was used to track luciferase expression in tumor cells expressing the Luc-Blast reporter. Mice were injected i.p. with luciferin (5 mg/mouse; Gold Technologies) and then imaged on a Xenogen IVIS Spectrum imager (PerkinElmer) 10 minutes later for 30 s. Quantification of luciferase signaling was analyzed using Living Image software (Caliper Life Sciences).

Preclinical drug studies

For preclinical treatment studies, EPO-GEMM mice were monitored for tumor development by palpation or ultrasound and randomized into treatment groups. For subcutaneous studies, EPO-GEMM derived cell lines were resuspended in Matrigel (BD Biosciences) and injected in the subcutaneous space. Following inoculation, mice were monitored three times a week. Caliper

measurements began when tumors became visible. Tumor volume was calculated using the following formula: tumor volume = (D x d^2)/2, in which D and d refer to the long and short tumor diameter, respectively. When tumors reached a size of 100-150 mm^3, mice were randomized based on starting tumor volume and enrolled into treatment groups. Tumor size and mouse weights were recorded three times weekly. Experimental endpoints were achieved when tumors reached 2000 mm^3 or became ulcerated. For i.p. studies, 1 to 2.5 million cells of EPO-GEMM derived cell lines carrying a luciferase reporter were resuspended in PBS and injected into the i.p. space in a volume of 200 µl. Tumor volume was monitored using IVIS imaging and mice were randomized based on starting tumor signal.

Mice were treated with vehicle or cisplatin (3 mg/kg body weight) by i.p. injection once a week. Anti-PD-1 antibody (200mg/mouse; RMP1-14, BioXCell) was given 3 times per week i.p. alone or in combination with cisplatin. No obvious toxicities were observed in vehicle- or drug-treated animals as assessed by changes in body weight. Upon sacrifice, ovarian tumor tissue was allocated to either 10% formalin fixation, flow cytometry analysis on fresh tissue or snap frozen for DNA/RNA analysis.

DNA constructs for electroporation

The Sleeping Beauty transposase (SB13) and the pT3 transposon vector were a generous gift of Dr. Xin Chen, UCSF San Francisco. The pX330 vector was a gift from Feng Zhang (Addgene plasmid # 42230). Table S2 provides the sgRNA sequences used in this study.

Clonality analysis of EPO-GEMM tumors

Genomic DNA was isolated from EPO-GEMM tumors using QIAGEN DNeasy Blood and Tissue kit following manufacturer's instructions. The p53 locus was amplified using a 50 µl reaction following standard Q5 High Fidelity Master Mix (NEB) protocol (forward primer: CAGAAGATATCCTGGTAAGG, reverse primer: CTACAGGCTGAAGAGGAACC). Amplicons were confirmed on a 2% agarose gel and PCR purified using QIAGEN QIAquick PCR purification kit. DNA concentration were measured using Nanodrop and samples were normalized to 20 ng/µl

and sequenced using EZ-amplicon sequencing (MiSeq, 2 x 250 bp by GENEWIZ, Inc, South Plainfield, NJ, USA).

CNA inference

1 µg of bulk genomic DNA (gDNA) was extracted from ovarian tumors and tissue using the DNeasy Blood & Tissue Kit (Qiagen) and sonicated using the Covaris instrument. Sonicated DNA was subsequently end-repaired/A-tailed, followed by ligation of TruSeq dual indexed adaptors. Indexed libraries were enriched via PCR and sequenced in multiplex fashion using the Illumina HiSeq2500 instrument to achieve roughly 1 million uniquely mappable reads per sample – a read count sufficient to allow copy number inference to a resolution of approximately 400kb. For data analysis, uniquely mapped reads were counted in genomic bins corrected for mappability. Read counts where subsequently corrected for GC content, normalized, and segmented using Circular Binary Segmentation (CBS). Segmented copy number calls are illustrated as relative gains and losses to the median copy number of the entire genome.

Tumor RNA-sequencing (RNA-seq)

For RNA-seq analysis of the transcriptional profiles of EPO-GEMM ovarian tumors, as well as normal ovaries of WT C57BL/6 mice, total RNA was extracted from bulk tissue using the RNeasy Mini Kit (Qiagen). Purified polyA mRNA was subsequently fragmented, and first and second strand cDNA synthesis performed using standard Illumina mRNA TruSeq library preparation protocols. Double stranded cDNA was subsequently processed for TruSeq dual-index Illumina library generation. For sequencing, pooled multiplexed libraries were run on a HiSeq 2500 machine on RAPID mode. Approximately 10 million 76bp single-end reads were retrieved per replicate condition. Resulting RNA-seq data was analyzed by removing adaptor sequences using Trimmomatic (Bolger, Lohse, and Usadel 2014), aligning sequencing data to GRCm38.91(mm10) with STAR (Dobin et al. 2012), and genome wide transcript counting using featureCounts (Anders, Pyl, and Huber 2015) to generate a TPM matrix of transcript counts. Genes were identified as

differentially expressed using R package DESeq2 with a cutoff of absolute log2(fold change) ≥ 1 and adjusted p-value < 0.05 between experimental conditions (Love, Huber, and Anders 2014).

Clustering and Gene Set Enrichment Analysis (GSEA)

Principal component analysis was performed using the DESeq2 package in R. Gene expressions of RNA-seq data were clustered using hierarchical clustering based on one minus pearson correlation test. For pathway enrichment analysis, the weighted GSEA Preranked mode was used on a set of curated signatures in the molecular signatures database (http://www.broadinstitute.org/gsea/msigdb/index.jsp, MSigDB v7.0). From 22,596 signatures, signatures with 15-500 genes were considered for further analyses. From the results, enriched signatures with an adjusted p-value less than 0.05 were considered as statistically significant. Hallmark and Kegg pathways were used to run GSEA on our murine EPO-GEMM models and human patient data (Pearce et al. 2018), and $-\log_{10}$(FDR) values were plotted in the XY plot.

Immunohistochemistry and immunofluorescence

Tissues were fixed overnight in 10% formalin, embedded in paraffin, and cut into 5 µm sections. Haematoxylin and eosin (H&E), immunohistochemical and immunofluorescence stainings were performed using standard protocols. Sections were de-paraffinized, rehydrated, and boiled in a microwave for 15 minutes in 10 mM citrate buffer (pH 6.0) for antigen retrieval. Antibodies were incubated overnight at 4ºC. Primary antibodies are listed in Table S3. HRP-conjugated secondary antibodies (Vectastain Elite ABC HRP Kits) were applied for 30 minutes and visualized with DAB (Vector Laboratories; SK-4100), or secondary Alexa Fluor 488 or 594 dye-conjugated antibodies (Life Technologies) applied for 1 hour at room temperature. Fluorescence antibody-labeled slides were mounted with Prolong Gold Antifade mountant (Prolong Molecular Probes; P36934) after counterstaining with DAPI.

In vitro cell assays

For knockdown studies, two independent MiRE-based shRNAs targeting *cGas* (shcGas1: CGAAGAAGTTAAAGAAATCAAA, shcGas2: CTCGAAGAAAATTGAATATGAA) were cloned into

MSCV-based vectors as described previously (Chicas et al. 2010). An shRNA targeting *Renilla* was used as a control (Saborowski et al. 2014). Following transduction with shRNA retroviral constructs, cell selection was performed with 4 µg/mL puromycin for 3 days. Knockdown efficiency was evaluated by RT-qPCR.

For cell viability assays, two thousand cells were plated in 100 µl of media per well of a black-walled 96-well plate (Perkin Elmer). The next day, media was changed, and cells were treated with drugs for 72 hours. Following treatment, cell viability was assessed using the CellTiter-Glo Viability Assay (Promega) according to the manufacturer's protocol. IC_{50} calculations were made using Prism 6 Software (GraphPad Software). Drugs for *in vitro* studies were dissolved in DMSO. Growth medium with vehicle or drugs was changed every 3 days.

For drug withdrawal assays, cells were pretreated for 5-7 days with vehicle (DMSO) or cisplatin, and then replated (5 x 10^3 cells per well of 6-well plate) in the absence of drugs for 5 to 7 days. Relative growth was quantified with Crystal Violet staining.

Senescence-associated beta-galactosidase staining

Senescence-associated beta-galactosidase (SA-β-gal) staining was performed as previously described at pH 5.5 for mouse cells and tissue and pH 6 for human cells (Krizhanovsky et al. 2008). Fresh frozen ovarian tumor sections, or adherent cells plated in 6-well plates, were fixed with 0.5% glutaraldehyde in PBS for 15 minutes, washed with PBS supplemented with 1mM $MgCl_2$, and stained for 18-24 hours in PBS containing 1 mM $MgCl_2$, 1 mg/ml X-Gal, and 5 mM each of potassium ferricyanide and potassium ferrocyanide. Tumor tissue sections were counterstained with eosin. For the fluorescent SA-β-gal labelling, frozen sections were incubated in 300 µM chloroquine solution for 30 minutes at 37ºC followed by exposure to the C12RG substrate (ImaGene Red C12RG *lacZ* Gene Expression Kit, Molecular Probes, I2906) for 2 hours at 37°C. The reaction was stopped by addition of 1 µM PETG. Slides were fixed with 4% PFA for 10 minutes at room temperature. 5 high power fields per well/section were counted and averaged to quantify the percentage of SA-β-gal$^+$ cells.

Cytokine array

EPO-GEMM derived ovarian cancer cell lines were plated in 6-well plates and treated for 48h with vehicle or cisplatin at IC50 concentrations. Conditioned media was collected, and the cells were trypsinized and counted using a cellometer (Nexcelom Biosciences). Conditioned media samples were normalized based on cell number by diluting with complete DMEM. 50 µl aliquots of the conditioned media were analyzed using multiplex immunoassays (Mouse Cytokine/Chemokine Array 31-Plex) from Eve Technologies. Biological replicates were averaged to determine cytokine levels.

Micronuclei quantification

Cells were seeded on chamber slides. Following vehicle or cisplatin treatment, the cells were washed and fixed in 4% formaldehyde/PBS for 10 minutes at room temperature. For confocal microscopy, cells were mounted on coverslips using ProLong Gold antifade reagent with DAPI counterstaining (#P36935, Life Technologies). Images were analyzed using ImageJ/Fiji software.

Rad51 assay

Cells were irradiated with a 10 Gy dose of ionizing radiation (IR) and allowed to recover for 4 hr. Cells were fixed with 4% solution of formaldehyde in PBS for 30 min and permeabilized in 0.2% Triton X-100 in PBS^{++} (PBS solution containing 1 mM $CaCl_2$ and 0.5 mM $MgCl_2$) for 20 min. For blocking, cells were incubated for 30 min in staining buffer (1% BSA, 0.15% glycine and 0.1% Triton X-100 in PBS^{++}). Cells were incubated with primary RAD51 antibody (70-001, BioAcademia, 1:5000) in staining buffer for 2h at room temperature followed by incubation of fluorophore-conjugated secondary antibody for 1h at room temperature. Samples were mounted with Prolong Gold Antifade mountant (Prolong Molecular Probes; P36934) after counterstaining with DAPI. RAD51 foci were quantified with ImageJ/Fiji software.

Flow Cytometry

To prepare single cell suspensions for flow cytometry analysis, tumors were minced with a razorblade into small pieces and placed in 5 ml of pre-warmed collagenase buffer (1x HBSS with calcium and magnesium (GIBCO), 2 mg/ml Collagenase D (11088858001; Sigma), 0.1 mg/ml DNase I (DN25; Sigma)). Samples were then transferred to C tubes and processed using program 37C_m_TDK1_1 on a gentleMACSC Octo dissociator with heater (Miltenyi Biotec). Dissociated tissue was filtered through a 70 µm cell strainer and centrifuged at 1500 rpm for 5 minutes. Samples were resuspended in FACS buffer (1x PBS, 2% FBS, 2 mM EDTA) and 3 x 10^6 cells were seeded in a U-bottom 96-well plate. Samples were blocked with anti-CD16/32 (FC block, BD Pharmigen) for 10 minutes and then incubated with antibodies for 30 minutes on ice. In each experiment, a myeloid and a lymphoid panel were set up. The antibodies used for flow cytometry are provided in Table S4 and S5. Gates were set using fluorescence minus one (FMO) controls. Flow cytometry was performed on a LSR Fortessa or LSR II flow cytometer, and data were analyzed using FlowJo (TreeStar).

RT-qPCR

Total RNA was extracted from cell lines treated with vehicle or cisplatin for 48h using the RNeasy Mini Kit (QIAGEN). Complementary DNA (cDNA) was obtained using the TaqMan reverse transcription reagents (Applied Biosystems). Real-time quantitative PCR was performed in duplicate or triplicate using SYBR Green PCR Master Mix (Applied Biosystems) on the ViiA 7 Real-Time PCR System (Invitrogen). Expression was calculated using the ΔΔCt method, *Gapdh* served as an endogenous normalization control. Table S6 indicates the primer sequences used for RT-qPCR.

Figure Preparation

Figures were prepared using BioRender.com for scientific illustrations and Illustrator CC 2020 (Adobe).

Supplementary Table S1: Overview of electroporation plasmid mixes

Mouse Strain	***Plasmid Mix***	***Genotype***
WT C57BL/6	20 µg sg*Trp53*/sg*Pten* Cas9 pX330 vector 20 µg sg*Rb* Cas9 pX330 vector	PPtRb
WT C57BL/6	20 µg sg*Trp53/Pten* Cas9 pX330 vector	PPt
WT C57BL/6	20 µg sg*Trp53* Cas9 pX330 vector	p53_only
WT C57BL/6	1 µg SB13 transposase 5 µg *MYC* transposon vector 20 µg sg*Trp53* Cas9 pX330 vector	MP
WT C57BL/6	1 µg SB13 transposase 5 µg *MYC* transposon vector 20 µg sg*Trp53*/*Brca1* Cas9 pX330 vector	MPB1
CK8-CreER;LSL-Cas9-IRES-GFP	1 µg SB13 5 µg *MYC* transposon vector 20 µg sg*Trp53* vector	CK8-MP

Supplementary Table S2: sgRNA sequences

Gene	***sgRNA sequence***
p53	ACCCTGTCACCGAGACCCC
Pten	GTTTGTGGTCTGCCAGCTAA
Rb	TGCGCGGGGTCGTCCTCCCG
Brca1_1 Brca1_2	TGTTATCCAAGGAACATCGG GCAGCAGGAAATGGCTCACC

Supplementary Table S3: Primary antibodies for IHC and IF

Antigen	*Manufacturer and catalogue number*
MYC	Abcam AB32072
Wilms-Tumor 1	Abcam AB89901
Cytokeratin-7	Abcam AB181598
Granzyme B	Abcam AB4059
Ki67	Abcam AB16667
Cancer antigen 125	Abbiotec 250566
Pax8	Proteintech 10336
CD8	Ebioscience 4SM15
Cleaved Caspase3	Cell Signaling 9664
γH2AX	Millipore JBW301
53BP1	Novus Biologicals NB100-305

Supplementary Table S4: Antibodies used for flow cytometry analysis (myeloid panel)

Antigen	*Fluorophore*	*Company*	*Clone #*	*Catalogue #*
CD45	AF700	Biolegend	30-F11	103128
CD3	BUV737	BD	17A2	612803
Ly6G	BV605	BD	1A8	563005
SIGLECF	PerCp-Cy5.5	BD	E50-2440	565526
LY6C	APC-C7	Biolegend	HK1.4	128026
CD11b	BUV395	BD	M1/70	563553
CD11c	BV785	Biolegend	N418	117335
MHCII	AF488	Biolegend	M5/114.15.2	107616
F4/80	PE-eFluor610	ThermoFisher	BM8	61-4801-82
CD19	BV650	BD	1D3	563235
CD103	PE	Biolegend	2E7	121405
PD-L1	APC	Biolegend	10F.9G2	124312
CD80	BV421	Biolegend	16-10A1	104725
CD206	BV711	Biolegend	C068C2	141727
Viability	eFluor506	ThermoFisher	-	65-0866-18

Supplementary Table S5: Antibodies used for flow cytometry analysis (lymphoid panel)

Antigen	*Fluorophore*	*Company*	*Clone #*	*Catalogue #*
CD45	AF700	Biolegend	30-F11	103128
CD3	AF488	Biolegend	17A2	100210
CD4	BUV395	BD	GK1.5	563790
CD8	PECy7	Biolegend	53-6.7	100722
CD25	BV605	Biolegend	PC61	102035
CD69	Percp-Cy5.5	Biolegend	H1.2F3	104522
CD62L	BV421	BD	MEL-14	562910
CD44	ApC-Cy7	BD	IM7	560568
PD1	PE	Biolegend	29F.1A12	135206
NK1.1	APC	Biolegend	PK136	108710
TIM3	BV711	Biolegend	RMT3-23	119727
LAG3	BV650	Biolegend	C9B7W	125227
KLRG1	BV785	Biolegend	2F1	138429
Viability	eFluor506	ThermoFisher	-	65-0866-18

Supplementary Table S6: Primer sequences used for RT-qPCR

cGas_Fw	GAGGCGCGGAAAGTCGTAA
cGas_Rv	TTGTCCGGTTCCTTCCTGGA
Ccl5_Fw	ATATGGCTCGGACACCACTC
Ccl5_Rv	TCCTTCGAGTGACAAACACG
Cxcl10_Fw	CCCACGTGTTGAGATCATTG
Cxcl10_Rv	GTGTGTGCGTGGCTTCACT
IL6_Fw	ACCAGAGGAAATTTTCAATAGGC
IL6_Rv	TGATGCACTTGCAGAAAACA

Supplementary References

1. A. Jiménez-Sanchez *et al.*, Unraveling tumor–immune heterogeneity in advanced ovarian cancer uncovers immunogenic effect of chemotherapy. *Nature Genetics*, 1–21 (2020).

2. A. Van Keymeulen *et al.*, Distinct stem cells contribute to mammary gland development and maintenance. *Nature*. **479**, 189–193 (2011).

3. A. M. Bolger, M. Lohse, B. Usadel, Trimmomatic: a flexible trimmer for Illumina sequence data. *Bioinformatics*. **30**, 2114–2120 (2014).

4. A. Dobin *et al.*, STAR: ultrafast universal RNA-seq aligner. *Bioinformatics*. **29**, 15–21 (2012).

5. S. Anders, P. T. Pyl, W. Huber, HTSeq--a Python framework to work with high-throughput sequencing data. - PubMed - NCBI. *Bioinformatics*. **31**, 166–169 (2015).

6. M. I. Love, W. Huber, S. Anders, Moderated estimation of fold change and dispersion for RNA-seq data with DESeq2. *Genome Biol.* **15**, 1–21 (2014).

7. O. M. T. Pearce *et al.*, Deconstruction of a Metastatic Tumor Microenvironment Reveals a Common Matrix Response in Human Cancers. *Cancer Discovery*. **8**, 304–319 (2018).

8. A. Chicas *et al.*, Dissecting the Unique Role of the Retinoblastoma Tumor Suppressor during Cellular Senescence. *Cancer Cell*. **17**, 376–387 (2010).

9. M. Saborowski *et al.*, A modular and flexible ESC-based mouse model of pancreatic cancer. *Genes Dev.* **28**, 85–97 (2014).

10. V. Krizhanovsky *et al.*, Senescence of activated stellate cells limits liver fibrosis. *Cell*. **134**, 657–667 (2008).